Title
Cosmology and Astro-particle Physics: What is Dark Matter and What is Dark Energy?

Permalink
https://escholarship.org/uc/item/0vv986jn

Author
Keeley, Ryan E

Publication Date
2018

Peer reviewed|Thesis/dissertation

UNIVERSITY OF CALIFORNIA,
IRVINE

Cosmology and Astro-particle Physics: What is Dark Matter and What is Dark Energy?

DISSERTATION

submitted in partial satisfaction of the requirements
for the degree of

DOCTOR OF PHILOSOPHY

in Physics

by

Ryan Keeley

Dissertation Committee:
Professor Kevork Abazajian, Chair
Professor Manoj Kaplinghat
Professor James Bullock

2018

TABLE OF CONTENTS

LIST OF FIGURES

LIST OF TABLES

ACKNOWLEDGMENTS

CURRICULUM VITAE

Ryan Keeley

EDUCATION

Doctor of Philosophy in Physics   **2018**
University of California, Irvine   *Irvine, California*

Master of Science in Physics   **2017**
University of California, Irvine   *Irvine, California*

Bachelor of Science in Physics   **2012**
California Institute of Technology   *Pasadena, California*

Bachelor of Science in History   **2012**
California Institute of Technology   *Pasadena, California*

RESEARCH EXPERIENCE

Graduate Research Assistant   **2014–2018**
University of California, Irvine   *Irvine, California*

TEACHING EXPERIENCE

Instructor   **2016**
University of California, Irvine   *Irvine, CA*

Teaching Assistant   **2012–2018**
University of California, Irvine   *Irvine, CA*

OUTREACH

COSMOS program   **2016–2017**
University of California, Irvine   *Irvine, CA*

REFEREED JOURNAL PUBLICATIONS

Tying Dark Matter to Baryons with Self-interactions   **2014**
Physical Review Letters

Bright gamma-ray Galactic Center excess and dark dwarfs: Strong tension for dark matter annihilation despite Milky Way halo profile and diffuse emission uncertainties   **2016**
Physical Review D

What the Milky Way's Dwarfs tell us about the Galactic Center extended excess   **2017**
Physical Review D

Model independent inference of the expansion history and implications for the growth of structure   **2017**
Physical Review D

INVITED TALKS AND CONFERENCES

Talk at 5th Korea-Japan Workshop on Dark Energy   August 2018

Talk at Conference on the Intersection of Particle and Nuclear Physics   June 2018

Talk at Texas A&M High Energy seminar   June 2018

Talk at TeV Particle Astrophysics conference   August 2017

Summer Institute for Neutrino Theory at Virginia Tech   July 2017

Talk at American Physical Society April Meeting   January 2017

SOFTWARE

GPHIST   `https://zenodo.org/record/999564`
Cosmological expansion history inference using Gaussian processes

ABSTRACT OF THE DISSERTATION

Cosmology and Astro-particle Physics: What is Dark Matter and What is Dark Energy?

By

Ryan Keeley

Doctor of Philosophy in Physics

University of California, Irvine, 2018

Professor Kevork Abazajian, Chair

We model the expansion history of the Universe as a Gaussian process and find constraints on the dark energy density and its low-redshift evolution using distances inferred from the Luminous Red Galaxy (LRG) and Lyman-alpha (Lyα) datasets of the Baryon Oscillation Spectroscopic Survey, supernova data from the Joint Light-curve Analysis (JLA) sample, Cosmic Microwave Background (CMB) data from the Planck satellite, and local measurement of the Hubble parameter from the Hubble Space Telescope (H0). Our analysis shows that the CMB, LRG, Lyα, and JLA data are consistent with each other and with a ΛCDM cosmology, but the H0 data is inconsistent at moderate significance. Including the presence of dark radiation does not alleviate the H0 tension in our analysis. While some of these results have been noted previously, the strength here lies in that we do not assume a particular cosmological model. We calculate the growth of the gravitational potential in General Relativity corresponding to these general expansion histories and show that they are well-approximated by $\Omega_{\mathrm{m}}^{0.55}$ given the current precision. We assess the prospects for upcoming surveys to measure deviations from ΛCDM using this model-independent approach.

We incorporate Milky Way dark matter halo profile uncertainties, as well as an accounting of diffuse gamma-ray emission uncertainties in dark matter annihilation models for the Galactic Center Extended gamma-ray excess (GCE) detected by the Fermi Gamma Ray

Space Telescope. The range of particle annihilation rate and masses expand when including these unknowns. However, empirical determinations of the Milky Way halo's local density and density profile leave the signal region to be in considerable tension with dark matter annihilation searches from combined dwarf galaxy analyses. The GCE and dwarf tension can be alleviated if: one, the halo is extremely concentrated or strongly contracted; two, the dark matter annihilation signal differentiates between dwarfs and the Galactic Center; or, three, local stellar density measures are found to be significantly lower, like that from recent stellar counts, pushing up the local dark matter density.

The Milky Way's Galactic Center harbors a gamma-ray excess that is a candidate signal of annihilating dark matter. Dwarf galaxies remain predominantly dark in their expected commensurate emission. We quantify the degree of consistency between these two observations through a joint likelihood analysis. In doing so I incorporate Milky Way dark matter halo profile uncertainties, as well as an accounting of diffuse gamma-ray emission uncertainties in dark matter annihilation models for the Galactic Center Extended gamma-ray excess (GCE) detected by the *Fermi Gamma-Ray Space Telescope*. The preferred range of annihilation rates and masses expands when including these unknowns. Even so, using two recent determinations of the Milky Way halo's local density leave the GCE preferred region of single-channel dark matter annihilation models to be in strong tension with annihilation searches in combined dwarf galaxy analyses. A third, higher Milky Way density determination, alleviates this tension. This joint likelihood analysis allows us to quantify this inconsistency. As an example, we test a representative inverse Compton sourced self-interacting dark matter model, which is consistent with both the GCE and dwarfs.

Self-interacting dark matter (SIDM) models have been proposed to solve the small-scale issues with the collisionless cold dark matter (CDM) paradigm. We derive equilibrium solutions in these SIDM models for the dark matter halo density profile including the gravitational potential of both baryons and dark matter. Self-interactions drive dark matter to

be isothermal and this ties the core sizes and shapes of dark matter halos to the spatial distribution of the stars, a radical departure from previous expectations and from CDM predictions. Compared to predictions of SIDM-only simulations, the core sizes are smaller and the core densities are higher, with the largest effects in baryon-dominated galaxies. As an example, we find a core size around 0.3 kpc for dark matter in the Milky Way, more than an order of magnitude smaller than the core size from SIDM-only simulations, which has important implications for indirect searches of SIDM candidates.

Chapter 1

Introduction

95% of the Universe is unknown. This unknown fraction is composed of two classes, dark matter and dark energy. The nature of these unknown components of the Universe has been identified by the Snowmass 2013 Community Summer Study as two of the most important questions for the particle physics community to answer over the next generation [8].

Dark energy's existence was first inferred from observations of supernova [9]. Supernova are a powerful probe of cosmology because they are standard candles; measuring their brightness tells you how far away they are. This is because the luminosity of the supernova is related to its duration. Hence, by measuring the flux of the supernova and how long the explosion lasts, the distance to the supernova can be inferred. Since the redshift of the supernova can also be measured from its spectra, cosmologists can build a distance-redshift relation from a large set of supernova. From this distance-redshift relation, the expansion history of the Universe can be inferred. In fact, not only do these supernova show the Universe is expanding, the expansion of the Universe is actually accelerating [10]. Part of the reason this discovery merits a Nobel prize is that all the known constituents of the Universe could only cause the Universe to decelerate, so this observed late-time acceleration would have to

come from some unknown source, which has come to be referred to as dark energy.

SN can precisely measure the acceleration of the Universe at late times, but since they only measure the ratios of distances, they can only measure the shape of the distance-redshift relation. To pin the distance-redshift to a scale, cosmologists can measure the present day value of the Hubble parameter. The Hubble parameter is the derivative of the log of the scale factor with respect to time. So measuring the Hubble parameter today measures how fast the Universe is presently expanding and hence fixes the distance-redshift relation at the zero redshift end. This is a particularly important quantity to measure, since because the Universe is as flat as we can measure, the present day Hubble parameter determines the total amount of energy density in the Universe and is therefore important in keeping an accurate accounting of the various components of the Universe.

There is an additional class of cosmological observables that can further extend the distance-redshift relation: baryon acoustic oscillations. In the early Universe, the baryons and the photons were tightly coupled in a plasma due to Compton scattering. Primordial density fluctuations of the early Universe plasma generated an attractive gravitational potential well. As dark matter and baryons fell into these potential wells, the pressure of the plasma eventually pushed out the baryons. The competing forces of gravity and pressure created oscillations or sound waves in the early Universe plasma [11]. The distance these sound waves can travel in the age of the Universe is known as the sound horizon. As the Universe expands and cools, the pattern of these sound waves is frozen-in and imprinted on the distribution of galaxies in the Universe. Specifically, the correlation function of galaxies, the probability of another galaxy being some distance away, has a peak at a distance corresponding to the sound horizon at the redshift of the galaxy sample [12, 13, 14, 15]. The relative sizes of the sound horizon in the early Universe and the sound horizon at some later redshift encodes information about how fast the Universe is expanding at that redshift and the angular diameter distance to that redshift, hence adding another point to the distance-

redshift relation.

The earliest point on the distance-redshift relation comes from the cosmic microwave background (CMB). The Universe started as a dense, tightly coupled plasma of (among other things) photons, baryons, and electrons. In the plasma, the photons interacted with the baryons and electrons often since those components were charged. Eventually, the Universe expanded and cooled leaving the baryons and electrons to form atoms. This process is called recombination. Since these atoms were neutral, the cross section for photons to scatter off them was suppressed and so after recombination these photons travelled through the Universe unimpeded until detected by microwave telescopes. These photons compose the CMB, the background radiation field that last interacted when the Universe was hot enough to disassociate hydrogen atoms.

The CMB is incredibly useful for cosmology. In the context of the expansion history of the Universe, by measuring the angular size of the sound horizon and the scale of photon diffusion damping (see Chapter 2.2.1), one can calculate the angular diameter distance to and the Hubble parameter at the redshift of recombination. In Chapter 2, I employ a model independent statistical technique called Gaussian process regression to infer the Universe's expansion history from a diverse set of measurements and calculate the implications for the growth of structure.

Beyond measuring distances, the CMB can be used to detect the existence of dark matter, specifically from the anisotropies in the cosmic microwave background. The statistical properties of the CMB's anisotropies are characterized by an angular power spectrum, which itself can be summarized by the positions and amplitudes of the of the CMB's acoustic peaks. The observed heights and positions of the CMB's acoustic peaks can constrain the total amount of matter in the Universe, the total amount of baryonic matter, and hence the total amount of dark matter [16, 17, 18, 19]. These acoustic peaks form a harmonic series based upon the value of the sound horizon, how far modes or sound waves can travel

from the beginning of the Universe until recombination. Hence, the first peak corresponds to modes that have compressed once before recombination, the second peak corresponds to modes that compressed then expanded exactly once, and so on [16]. Relative to the even numbered peaks, the heights of the odd numbered peaks increase with a greater amount of baryons in the Universe. Furthermore, the total matter density will tend to decrease the amplitude of all the peaks, since the size of the modes' fluctuations in the early Universe is controlled by the gravitational potential. A steeper gravitational potential corresponds to a smaller fluctuation and a greater density of matter leads to a steeper gravitational potential. Hence, measuring the amplitude of the CMB's acoustic peaks can infer the total amount of matter in the Universe, the amount of baryonic matter, and hence the amount of dark matter.

Though the CMB may be the most significant detection of dark matter, the first hints of dark matter's existence were discovered by Fritz Zwicky when he observed the velocity dispersion of the Coma galaxy cluster [20]. Velocity dispersion is a measure of the with of the distribution of a system's velocities, specifically, the square of the velocity dispersion is the average squared difference from the mean velocity. This velocity dispersion can be related to the mass of the galaxy cluster with the virial theorem. The virial theorem relates the average kinetic energy of an ensemble of particles (related to the velocity dispersion) and the average potential energy (related to the total mass of the system). Zwicky observed that the velocity dispersion of the galaxies in the Coma cluster were too large to be explained by the observed mass of the luminous matter. This was explained by the existence of some additional non-luminous mass or dark matter. Vera Rubin saw further evidence for dark matter in the rotation curves of spiral galaxies[21]. If the luminous matter were the only component of the system, then Newtons's law implies the rotation curve should decrease beyond where the luminous matter is observed. However, these rotation curves remain flat for large radii. Again, these observations indicate the presence of dark matter. Further evidence for dark matter is seen in the Bullet cluster, which is a system with two merging

galaxy clusters. The total mass of the Bullet cluster is determined by the gravitational lensing of background galaxies. Gravitational lensing is a novel prediction of general relativity which relates the deflection of light to the mass of the lensing system. As opposed to Newtonian gravity, general relativity dictates that matter warps or curves space. Since light travels along straight lines, which in curved space is generalized to the notion of a geodesic, and since straight lines in curved space are curved, the trajectories that light follows will generically be deflected by the gravity of any mass they encounter. Hence, measuring the deflection of light also infers the mass of the system. Using this technique the total mass distribution of the Bullet cluster was calculated to extend beyond where the luminous matter was observed [22], which again indicates there must be some sort of dark matter. The reason the dark matter and the luminous baryonic matter would have different spatial extents during this sort of merger comes from the difference in how they interact with themselves. The luminous baryonic matter can interact strongly with itself such that it all sticks together during the collision. The approximately collisionless (at these velocity scales at least) dark matter will pass through itself during the collision and hence extend beyond where the luminous matter is seen [23].

There are a large number of ideas for what dark matter could be. Axions, primordial black holes, sterile neutrinos, weakly interacting massive particles (WIMP), scalar fields or superfluid dark matter: the list goes on. A different slicing of the question is to ask what phenomenological properties the dark matter has. i.e. specifying its temperature (cold dark matter (CDM) or warm dark matter (WDM)) or whether it can interact with itself (collisionless dark matter vs self-interacting dark matter (SIDM)). Characterizing these phenomenological properties of dark matter is in some sense the easier task since it just requires information about how dark matter is distributed. Identifying the fundamental nature of dark matter would likely be a harder question since it would probably require a positive signal of dark matter interacting with the Standard Model, which has not yet been definitively observed.

Astrophysical and cosmological environments are uniquely useful to determine the nature of dark matter. There are three classes of experiments that can give insight to how dark matter might interact with Standard Model particles: indirect detection, direct detection, and collider experiments. Indirect detection has the advantage of the fact that dark matter is cosmologically abundant and hence has the potential to have large signals (or in the case of non-detection very constraining limits) but comes at the cost of having complicated backgrounds that could confuse the interpretation of any potential observations. One of the most interesting indirect detection signals is the Galactic center extended (GCE) excess. After accounting for the known astrophysical processes, there remains a significant excess of gamma rays coming from the Galactic center, which has come to be known as the GCE. In Chapters 3 and 4, I investigate whether annihilating WIMPs can explain the GCE.

Further information about dark matter can be gained from analyzing the clustering of matter in the Universe. Measuring the clustering of matter from the largest to the smallest can yield information about how much matter is in the Universe, about how strong gravity acts on the largest scales, and about the detailed microphysics of dark matter [24, 25, 26, 27, 28]. The statistical quantity that encodes this information is called the matter power spectrum. The matter power spectrum is not directly observable but there are a number of tracers that can be used to infer the matter power spectrum, up to some unknown bias factor. The simplest quantity to observe is the clustering of galaxies. Since galaxies live in dark matter halos they should be good tracers of the total matter distribution, however, since the baryonic matter is not distributed in exactly the same way as the dark matter, the statistical parameters of the baryonic matter distribution are biased estimates of the statistical parameters of the total matter distribution [29, 30, 12]. Therefore, any signal from just measuring the clustering of galaxies will be degenerate with the unknown bias.

The Lyman-alpha forest is another observable that can measure the matter power spectrum. High redshift quasars are luminous over a wide range of wavelengths. This light propagates

through an expanding Universe and hence gets redshifted. If this redshifted light encounters hydrogen gas then the fraction of the emitted light that has the same wavelength as the Lyman-alpha transition will be absorbed by the hydrogen gas. As this light further propagates and encounters different hydrogen gas clouds at different redshifts, then different parts of the emitted spectrum will be absorbed. This 'forest' of absorption lines from the Lyman-alpha transition has come to be known as the Lyman-alpha forest. Therefore, observing the absorption spectra of quasars can yield information about the distribution of this hydrogen gas throughout the Universe, and hence serves as another biased tracer of the distribution of the total matter [31, 32].

Another method to measure the distribution of matter in the Universe is to measure the weak gravitational lensing signal. Gravitational lensing represents a useful tool to understand the distribution of matter over a wide range of scales. This is primarily due to the fact the amount of lensing scales with the total amount of matter (rather than just the luminous baryonic matter) and hence is an unbiased tracer of the matter distribution. For cosmology, the most commonly measured lensing signal is the weak lensing of background galaxies by the intervening large-scale structure. The large-scale structure will tend to make these background galaxies look more elliptical and aligned. These effects are collectively referred to as shear-type lensing. This measurement is not without its caveats, however, as the expected signal is small and can be mimicked by intrinsic properties of the background galaxies. Nevertheless, a number of groups have detected this cosmic shear signal and used this measurement to better understand the Universe, specifically how much matter there is and the amplitude of perturbations. [33, 34]

These characterizations of the large scale structure of the Universe have been instrumental in developing the CDM paradigm of hierarchical structure formation, where the smallest scales collapse first and form small dark matter halos [35, 36]. These small dark matter halos accrete onto each other, eventually growing into the currently observed cosmic web of dark matter.

There is potentially more to be learned beyond the successes of the CDM paradigm. For instance, the distribution of matter on smaller scales can yield additional information about the microphysics of dark matter. Indeed, a number of problems for this paradigm have arisen and these problems can point to extensions of the CDM paradigm. These problems are all differences between the predictions of ΛCDM simulations and observations of dwarf galaxies in the Local Group. The dwarf galaxies predicted by these simulations are too dense (the Too Big to Fail Problem) [37], too cuspy (the core-cusp problem or more recently the diversity problem)[38], or too numerous (the Missing Satellites Problem) [39]. Each of these problems could have astrophysical solutions but the implications for dark matter are intriguing. For instance, the Missing Satellite Problem could point to WDM. The temperature of the dark matter characterizes the amount of structure. The amount of structure can be thought of as how different a distribution is from a homogenous one. A distribution with only one large overdensity has little structure and a distribution with an abundance of overdensities from small to large scales has much structure. Dark matter can impede the growth of structure if it can free stream, propagate without interacting. Typically, if dark matter could free stream for some distance the growth of structure would be suppressed for length scales smaller than that free streaming length. The temperature of the dark matter sets this free streaming length; the warmer the dark matter is the further it can free stream. Putting this all together, the warmer the dark matter is, the less structure there is and larger the smallest dark matter halo is. Therefore, WDM is a natural explanation for the missing satellite problem. Further, SIDM can potentially explain both the Too Big to Fail problem and the diversity problem. In Chapter 5, I explore the effects of SIDM on the shapes of dark matter halos and how these effects change with different baryonic potentials.

Chapter 2

Model independent inference of the expansion history and implications for the growth of structure

2.1 Introduction

The ΛCDM model, with a cosmological constant (Λ), cold dark matter (CDM), and baryons, provides an excellent fit to cosmological observations at both low and high redshift [18, 12, 10, 40]. However, as the statistical precision of datasets have improved, the standard ΛCDM model has increasingly pointed towards the existence of dataset discordances, most notably a 3.4σ tension between the direct measurement of the Hubble constant [41] and that inferred from cosmic microwave background (CMB) temperature measurements by Planck [17, 18]. Further moderate discordances include the Planck CMB temperature with the Lyman-α forest of the Baryon Oscillation Spectroscopic Survey (BOSS; [13, 14, 15]), Planck Sunyaev-Zel'dovich cluster counts [42, 43], and weak gravitational lensing measurements by

the Canada-France-Hawaii Telescope Lensing Survey (CFHTLenS; [44, 28]) and the Kilo Degree Survey (KiDS; [40, 26, 34, 27, 25]).

The tensions among datasets could be due to underestimated systematic effects associated with the experiments, or it may point to physics beyond the standard ΛCDM cosmology (e.g. [45, 26, 46]). Examples of physics beyond the standard cosmological model include a time evolving equation of state for the dark energy fluid (e.g. [47, 48]), an infrared modification to General Relativity (GR; e.g. [49, 50]), or a coupling of matter and dark energy (e.g. [51, 52]). An approach independent (as far as possible) of a cosmological model could be very useful given the lack of concrete directions to understand the larger cosmological constant problem (e.g. [53, 54, 55]).

Motivated by these observations, we test the ΛCDM model by inferring the expansion history and growth of structure in a "model-independent" manner using the method of Gaussian processes (GP; e.g. [56]). GP regression is compelling since it is both more flexible and more data driven than parametric approaches [57]. Performing such a regression analysis with GP is additionally useful since it avoids the problem of over fitting which is ubiquitous for polynomial regression.

A model independent approach runs into two issues: what freedom do we allow at the redshift of last scattering and how do we include the data on the growth of structure in a model-independent manner? We adopt a compromise in this work by assuming that at the time of last scattering the Universe can be described by a model based on General Relativity with dark matter, baryons, photons, three active neutrinos, and possibly extra relativistic degrees of freedom. We compute the growth history in a model-independent manner from the expansion history with the assumption of General Relativity and then compare it to observations.

Previous studies have used GP regression to study the expansion history generally, and to

study the dark energy equation of state specifically. An early example of the former is the study by Shafieloo, Kim, and Linder (2012) [58], where the authors generate a GP for $H(z)^{-1}$ (without dividing out a fiducial model) and use the regression on the Union 2.1 dataset of supernovae (SNe). They take the results of their GP regression, derive a posterior for the deceleration parameter $q = -a\ddot{a}/\dot{a}^2$, and find agreement with the ΛCDM cosmology. Our method builds on these investigations and we also include additional datasets and distance measures (D_A).

An example of modeling the dark energy equation of state $w(z)$ using GP is found in Holsclaw et al. [59, 60, 61]. They generate the dark energy density from $w(z)$, and along with fiducial values for the matter density and radiation density, calculate a luminosity distance. They use simulated datasets and the Constitution set of SNe to constrain $w(z)$. They point out, however, that the reconstructed equation of state is sensitive to the assumed fiducial values. The authors also discuss prospects for using the baryon acoustic oscillation (BAO) feature and CMB to reconstruct the equation of state.

A recent analysis parameterized the late-time expansion rate $H(z)$ with cubic splines and discussed the tension between the local measurement of H_0 and its Planck inference [62]. They pointed out that the H_0 tension could be pointing to a smaller sound horizon at the drag epoch (r_{drag}), since they are both derived parameters of the expansion rate. Using the temperature and low-ℓ polarization data, they concluded that including extra radiation at recombination can relieve this tension. However, the inclusion of the high-ℓ polarization data disfavors this interpretation. We will compare to these results in the discussion of the H_0 tension in the forthcoming sections.

In Section 2.2, we outline the different datasets used in our analysis, which span a wide range of redshifts from the present to the epoch of recombination. In Section 2.3, we describe the setup for our GP regression and the inferences on the expansion history that the regression provides, both with present data and forecasted with DESI. In Section 2.4, we use the GP

results to infer the growth history and dark energy density with redshift. We conclude with a summary of our results in Section 2.5.

2.2 Data

We include low-redshift distances from Beutler et al. (2016) [63], who analyzed the clustering of more than a million galaxies in the redshift range $0.2 < z < 0.75$ from the final BOSS data release (DR12) to extract the baryon acoustic oscillation signal. The angular diameter distance, $D_A(z)$, and Hubble parameter, $H(z)$, are measured at the $1 - 3\%$ level in three redshift bins centered at $z = 0.38$, 0.51, and 0.61. We label this dataset 'LRG'.

From Bautista et al. (2017) [15], we obtain high-redshift distances calculated from the BAO feature in the flux correlation function of the Lyα forest. Bautista et al. (2017) use more than 150,000 quasars in the redshift range $2.1 \leq z \leq 3.5$ from DR12 of the BOSS SDSS-III. They measure the Hubble distance and the angular diameter distance with respect to the size of the sound horizon at the drag epoch, r_{drag}, at an effective redshift of $z = 2.33$. This dataset is labeled 'Lyα' in the rest of this paper.

New results by the BOSS collaboration on the Lyα–quasar correlation function at $z = 2.4$ have just been released [64]. The results are consistent with the Planck cosmology [18] at the 2-σ level. The small deviation from Planck ΛCDM is, however, difficult to model because the inferred D_H at $z = 2.4$ is larger, while D_A is smaller. When combined with the auto-correlation data [15], the Planck cosmology shows a moderate 2.3-σ tension [64]. This finding is consistent with the previous BOSS Lyα results [14]. A detailed discussion of this moderate tension in the Lyman-α and Planck datasets in terms of alternate models found no satisfactory solution [65]. In particular, alternative solutions could not simultaneously fit all the BAO data and hence were not preferred over the flat ΛCDM model. If the tension

becomes stronger, it would be interesting to use our model-independent method to search for a possible solution. For the present, we do not include this new cross-correlation dataset, or the older dataset, in our analysis.

For our baseline results, we consider a fiducial value for $r_{\mathrm{drag}} = 147.36$ Mpc for the BAO measurements. Since the relative uncertainty in r_{drag} is significantly smaller than the uncertainty in the measured value of the ratios D_H/r_{drag} and D_A/r_{drag} from the LRG and Lyα datasets, we take the uncertainties in D_H and D_A to arise only from the uncertainty in the ratios for the main analysis. We relax this assumption when discussing an expanded parameter space where the error on r_{drag} becomes comparable to the BAO measurement errors.

We include the direct measurement of the Hubble constant by Riess et al. (2016) [41], who used the Wide Field Camera 3 on the Hubble Space Telescope to observe Cepheid variables in the same host galaxies as recent Type Ia supernovae to anchor its $z = 0$ magnitude-redshift relation. Riess et al. (2016) determined the distances to low-redshift anchors such as the megamaser system NGC 4258 and the Large Magellanic Cloud more robustly, and increased the number of observed local Cepheids in regions such as M31, the Large Magellanic Cloud, and the Milky Way. These improvements led to the estimate $H_0 = 73.24 \pm 1.74 \, \mathrm{km \, s^{-1} \, Mpc^{-1}}$, which we refer to as 'H0'.

For luminosity distances inferred using Type Ia supernovae, we include the binned supernovae from Betoule et al. (2013, 2014) [66, 10]. The 740 SNe of the SDSS-II and SNLS collaborations (joint light-curve analysis sample) are compressed into 31 redshift bins between $0.01 < z < 1.3$. These constraints are effectively on the ratio D_L/D_{H_0}, so we marginalize over the normalization of this distance modulus. We denote this dataset 'SN'.

We consider the CMB temperature and polarization data from the Planck satellite [67, 18] to derive posteriors for the Hubble distance and angular diameter distance to the redshift of last scattering, z_*. The Planck dataset includes TT, EE, TE, and lowP angular power

spectra. We refer to this dataset as 'CMB'. In Section 2.2.1, we discuss the key physics that controls the measured covariance matrix of D_H and D_A at the last scattering surface. Fiducially, we do not include the power spectrum of the CMB lensing potential (ϕ) as part of the CMB dataset to avoid mixing high-z and low-z measurements (as the lensing kernel peaks at low redshift [68, 69]).

Another epoch that lends itself to a model-independent analysis is Big Bang Nucleosynthesis where constraints on the expansion history have been obtained independent of a cosmological model [70]. We do not include it here given the many e-folds of scale factor between last scattering and the epoch when light elements form.

2.2.1 Understanding the CMB constraint

The angular size of the sound horizon is given by the radius of the sound horizon at last scattering, r_s, divided by the angular diameter distance D_A to last scattering: $\theta_s = \frac{r_s}{D_A(z_*)}$. The radius of the sound horizon is $r_s = \int_{z_*}^{\infty} D_H(z)c_s(z)/c \; dz$, which scales with $D_H(z_*)$. Here, c_s/c is the sound speed relative to the speed of light, and D_H is the Hubble distance. We will discuss the impact of new physics on r_s in Section 2.3.2.

With only information about the angular size of the sound horizon $\theta_s \propto D_H(z_*)/D_A(z_*)$, the $D_H(z_*)$ and $D_A(z_*)$ measurements would be fully degenerate. This degeneracy is broken by measuring the wavenumber related to photon diffusion, k_D. Diffusion is a random walk, so the diffusion length ($\propto 1/k_D$) scales as the square root of the number of scatterings multiplied by the mean free path. The number of scatterings is proportional to $D_H(z_*)$, which gives $k_D \propto 1/\sqrt{D_H(z_*)}$. Note that the effect of damping on the heights of the peaks is dictated by the quantity $k_D r_s \propto \sqrt{D_H(z_*)}$, which is independent of low-redshift physics [71].

Given constraints on θ_s and k_D, and knowing how they depend on D_H and D_A, we can

express the joint CMB log-likelihood for $D_H(z_*)$ and $D_A(z_*)$ in the following manner:

$$-2\log\mathcal{L}(D_H, D_A) \propto \left(\frac{k_1 D_H/D_A - \bar{\theta}}{\sigma_\theta}\right)^2 + \left(\frac{k_2/\sqrt{D_H} - \bar{k}_D}{\sigma_k}\right)^2, \quad (2.1)$$

where k_1 and k_2 are constants, the bars represent the measured values, and σ with a subscript is the uncertainty in the measured value corresponding to the subscript. We use this likelihood function to derive the covariance matrix, C, as the inverse of the Fisher matrix, $\mathcal{F}_{ij} = \langle\frac{d^2\log\mathcal{L}}{dx_i dx_j}\rangle$, where $x_{i,j}$ are any generic parameters:

$$C = \begin{bmatrix} 4D_{H,0}^2\left(\frac{\sigma_k}{k_D}\right)^2 & 4D_{A,0}D_{H,0}\left(\frac{\sigma_k}{k_D}\right)^2 \\ 4D_{A,0}D_{H,0}\left(\frac{\sigma_k}{k_D}\right)^2 & D_{A,0}^2\left[4\left(\frac{\sigma_k}{k_D}\right)^2 + \left(\frac{\sigma_\theta}{\theta}\right)^2\right] \end{bmatrix}. \quad (2.2)$$

Using the values from our simplest Markov Chain Monte Carlo case (MCMC; using COSMOMC [72]), 'ΛCDM: TT', where $100\theta_s = 1.04131\pm0.00051$, $k_D = 0.14049\pm0.00053$ Mpc^{-1}, $D_H = 1.927\times10^{-1}$ Mpc, and $D_A = 1.275\times10^1$ Mpc, we calculate $C_{11} = 2.15\times10^{-6}$ Mpc^2, $C_{12} = 1.42\times10^{-4}$ Mpc^2, and $C_{22} = 9.44\times10^{-3}$ Mpc^2.

Compared to the actual covariance matrix for that same COSMOMC run, where $C_{11} = 1.69\times10^{-6}$ Mpc^2, $C_{12} = 5.89\times10^{-5}$ Mpc^2, and $C_{22} = 2.24\times10^{-3}$ Mpc^2, our approximation overestimates the uncertainties of D_H and D_A by about a factor of 1.1 along the D_H direction and by a factor of 2.1 along the D_A direction. This approximation worsens as CMB polarization information is included in the COSMOMC calculation. This is likely because adding more data like 'lowP' or 'TE+EE' brings in more information that constrains D_H and D_A indirectly without impacting k_d and θ_s. This is reflected in the covariance matrices; both the approximate and actual covariance matrices decrease with additional data, but the actual covariances decrease faster.

This exercise shows that other features in the CMB angular power spectrum (not just θ_s and k_D) constrain D_H and D_A. Thus, it is important to examine how new physics at the last scattering surface can bias our inferred expansion history at late times. We discuss this in Section 2.3.2.

2.3   Expansion history

Assuming flatness, we constrain the expansion history $H(z)$ as a function of redshift using the Hubble distance $D_H(z) \equiv c/H(z)$, the angular diameter distance $D_A(z) \equiv D_C(z)/(1+z)$, and the luminosity distance $D_L(z) \equiv D_C(z)(1+z)$, where $D_C(z) = \int_0^z D_H(z')dz'$ is the comoving distance. We factor out a reference history $D_H^0(z)$, and model

$$\gamma(z) = \ln(D_H(z)/D_H^0(z)),\tag{2.3}$$

as a GP with zero mean $\langle\gamma(z)\rangle = 0$ and a covariance function

$$\langle\gamma(z_1)\gamma(z_2)\rangle = h^2 \exp(-(s(z_1) - s(z_2))^2/(2\sigma^2)),\tag{2.4}$$

with hyperparameters h and σ (e.g. [56, 73]). Note that we could expand our analysis in a simple way to non-flat cosmologies by including the curvature as an additional hyperparameter.

We use the Planck+WP best fit to flat ΛCDM from Ade et al. (2013) [17] to calculate the reference history $D_H^0(z)$. Specifically, the fiducial model is constructed with Hubble constant $H_0 = 67.04 \text{ km s}^{-1} \text{ Mpc}^{-1}$, present matter density $\Omega_m = 0.3169$, present dark energy density $\Omega_{DE} = 0.6831$, effective number of neutrinos $N_{eff} = 3.046$, and one neutrino species with
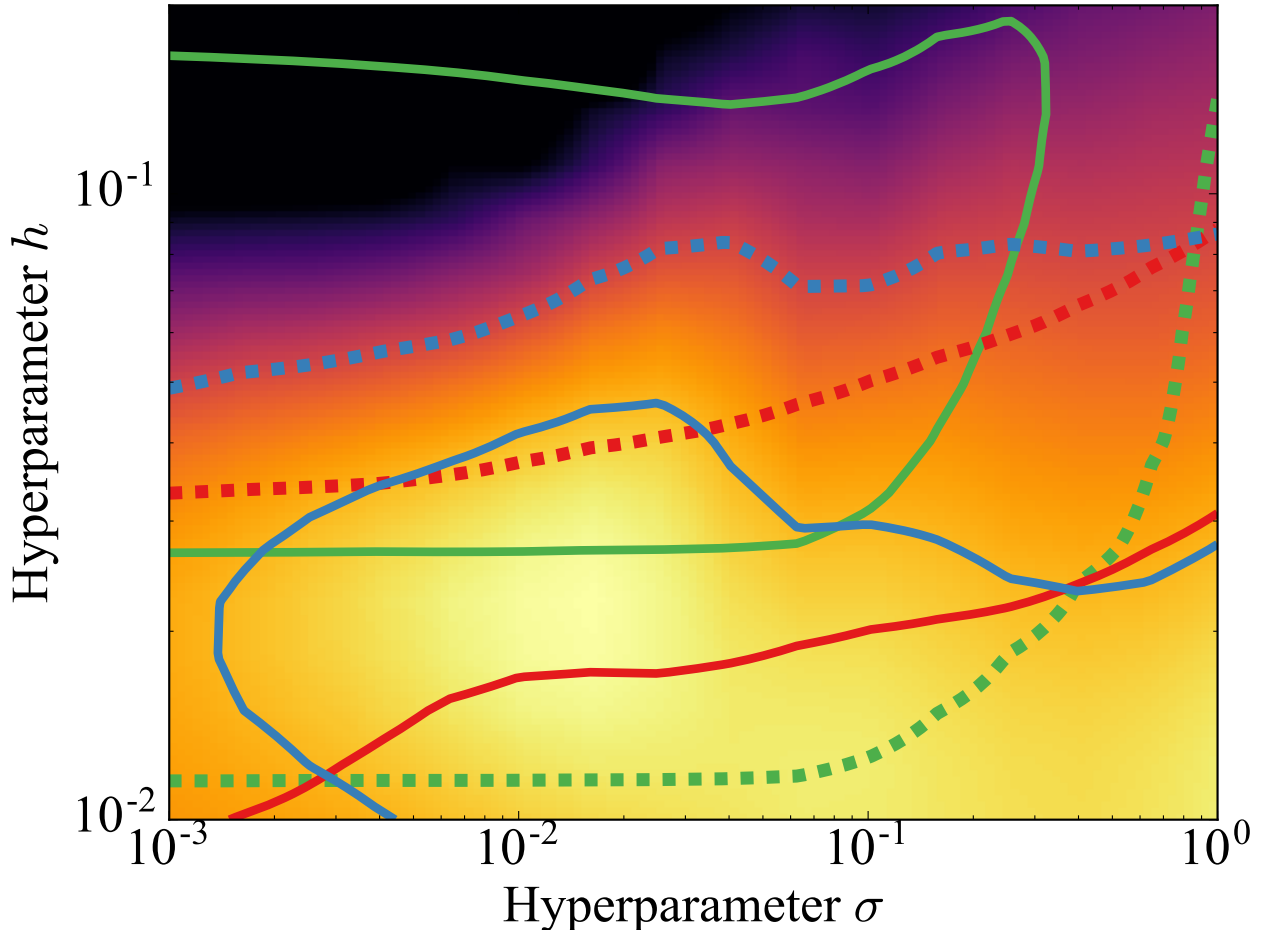
Figure 2.1: Plotted are the 1 and 2-σ contours of the posterior of the hyperparameters $\{h, \sigma\}$ that generate the GP. The solid lines correspond to the 1-σ contours, and dashed lines the 2-σ contours. Green corresponds to the H0-Lyα combination, red the CMB-SN-LRG combination, and blue the full H0-Lyα-CMB-SN-LRG combination. The color map also corresponds to the full combination. It is apparent that the GP regression favors certain values of the hyperparameters. Particularly, the CMB-SN-LRG, which is consistent with the fiducial model, does not meaningfully constrain σ, which describes the correlation length of the fluctuations, and prefers small values of h, which describes the size of the fluctuations.

mass $m_\nu = 0.06$ eV. The evolution variable $s(z)$ is taken to be

$$s(z) = \log(1 + z)/\log(1 + z_{\max}), \tag{2.5}$$

where $z_{\max} = 1090.48$, which matches the redshift of last scattering for the Planck+WP best fit. Note that $s(z)$ goes from 0 to 1 as z changes from 0 to $z_{\max}$. We discretize $D_H(z)$ on a grid in z and linearly interpolate $D_H(z)$ in $s(z)$ to obtain $D_C(z)$ through the following

17
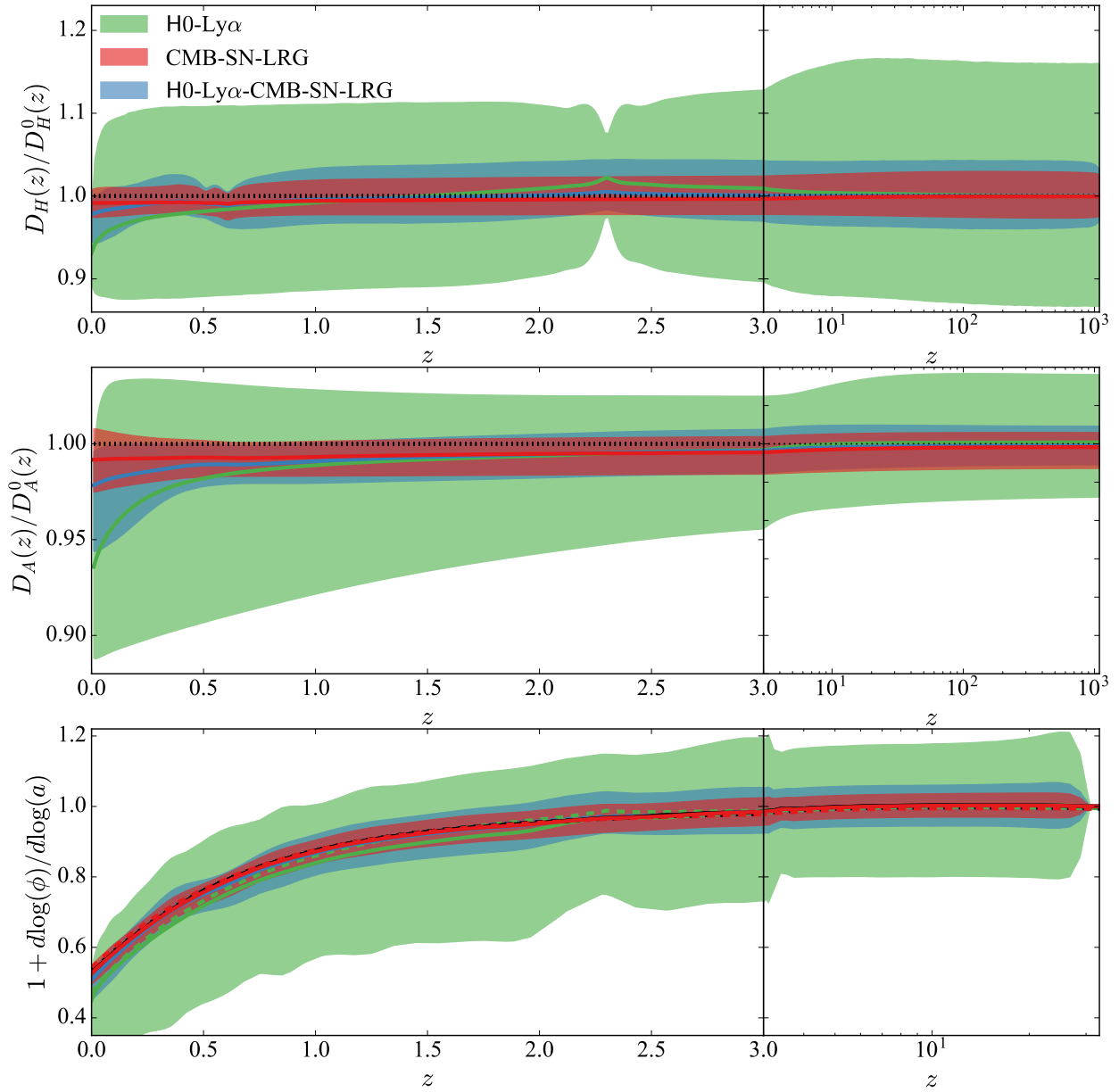
Figure 2.2: Expansion and growth histories determined by the GP regression for different combinations of the H0, Lyα, CMB, SN, and LRG datasets. The top panel shows the Hubble distances and the middle panel shows the angular diameter distances. These distances are plotted relative to those from the fiducial Planck ΛCDM cosmology. The shaded regions are bounded by the 90% confidence level contours generated from the posterior probability for the quantity at that redshift. The solid lines denote the median values, and the dotted lines denote ΛCDM. As in Figure 2.1, we show the combination that includes all of the different datasets, H0-Lyα-CMB-SN-LRG (blue), and the partition of the full dataset into combinations that are consistent with fiducial ΛCDM (CMB-SN-LRG, in red), and combinations that show moderate tension (H0-Lyα, in green). The bottom panel shows the growth rate $f(z) = 1 + d\log(\phi)/d\log(a)$ derived from the expansion history. The dashed lines are $\Omega_{\rm m}^{\gamma}(z)$, where γ is determined by the value that minimizes the squared distance between f and $\Omega_{\rm m}^{\gamma}(z)$ weighted by the size of the uncertainty in $f(z)$. $\gamma = 0.52, 0.53, 0.56$ for the H0-Lyα-CMB-SN-LRG, H0-Lyα, CMB-SN-LRG combinations, respectively.

quadrature,

$$
\begin{aligned}
D_C(z_{i+1}) = &\, D_C(z_i) + D_H(z_i)(z_{i+1} - z_i) \\
&+ \frac{D_H(z_{i+1}) - D_H(z_i)}{s(z_{i+1}) - s(z_i)} \int_{z_i}^{z_{i+1}} \big(s(z) - s(z_i)\big)\, dz \, .
\end{aligned}
\tag{2.6}
$$

We use a fine enough grid in z so that the errors from this quadrature are small.

GP regression is particularly useful since the regression occurs in an infinite-dimensional function space without overfitting. The covariance function of a GP corresponds to a Bayesian regression with an infinite number of basis functions [56]. GP regression works by generating a large sample of functions ($\gamma(z)$) determined by the covariance function. These functions generated by the GP are transformed into Hubble distances and angular diameter distances, as in Eqn. 2.3. Each of these generated expansion histories are given a weight determined by the likelihood of the data. These weighted expansion histories are then histogrammed at various redshifts in the range $0 < z < 1090.48$. Although standard libraries are available for GP, this application required custom code to support flexible constraints in the coupled $D_C(z)$ and $D_H(z)$ evolutions. This code [74] is publicly available at `https://github.com/dkirkby/gphist`.[1]

The results of the GP regression of course depend on the hyperparameters that determine the GP's covariance function. Accordingly, we marginalize over these hyperparameters on a grid with values $0.01 < h < 0.2$ and $0.001 < \sigma < 1.0$. We calculate the posteriors of these hyperparameters (Figure 2.1) and find that they are well constrained when multiple datasets are used.

The effects of the hyperparameters, h and σ can be understood in the following way. When looking at the prior distribution (i.e., inference without a dataset), the errors on the GP result

---

[1]After writing this paper we learned of a software package [75, 76] with similar capabilities to ours.
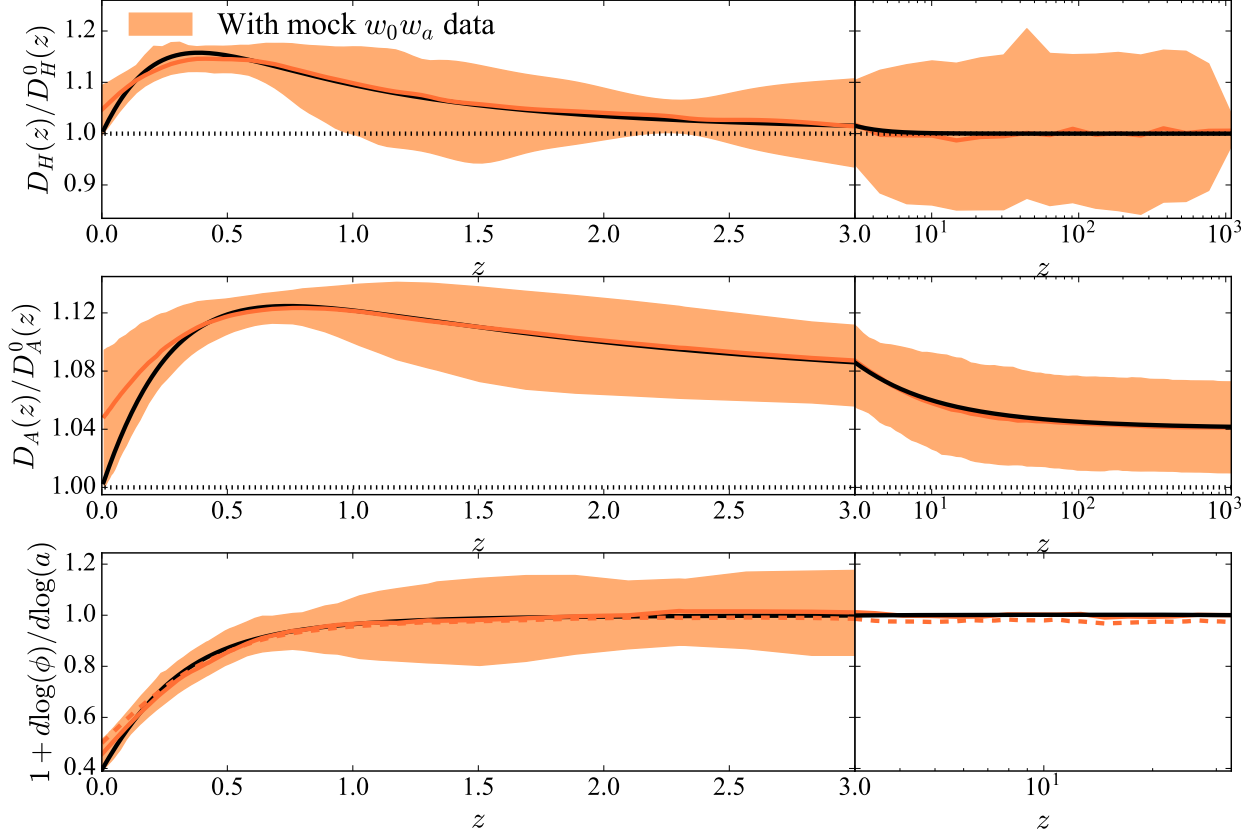
Figure 2.3: Results of the GP regression for mock data generated from a $w_0 w_a$ cosmology and resampled with the covariance matrices of the actual data. The shaded regions represent the posterior probabilities for the expansion and growth histories with redshift, bounded at 90% CL. The results of the GP regression are in orange (solid orange lines denoting the medians), while the solid black lines correspond to the $w_0 w_a$ input cosmology. As in Figure 2.2, the top panel shows the Hubble distance divided by the fiducial distance from a Planck ΛCDM cosmology, the middle panel shows the angular diameter distance, and the bottom panel shows the growth rate. The dashed orange line in the bottom panel is $\Omega_{\rm m}^\gamma(z)$, where $\gamma = 0.65$.

vary proportionally with h because it controls the size of the fluctuations. Should data at some redshift pick out a certain scale for h, then that scale will set the size of the error bars at redshifts unconstrained directly by the data. Typically, if the data are consistent with fiducial values up to some fluctuations, the GP regression will pick out smaller values of h. Exactly how small is determined by the size of the error bars; larger values of h will tend to scatter the expansion history beyond the error bars and smaller values of h will be consistent with the data. Hence, if the data are close to the fiducial values, only an upper limit on

h may be inferred and the error bars on the GP result will be small, as is the case for the CMB-SN-LRG case (see Figure 2.1). The other hyperparameter, σ, controls the correlation length of the GP: if σ is too large, the median of the regression misses a significant portion of the variance; if σ is too small, the median of the regression overfits the data. If the constraints are sufficiently close to the fiducial values, or if the data prefers small values of h, the GP regression will not be able to constrain the values of σ.

In Figure 2.2, we show the median expansion history and 90% confidence level (CL) contours derived from the GP. The bands that overlap with the black dashed line at a given redshift are consistent with the best-fit Planck ΛCDM cosmology at that redshift (at 90% CL). Similarly, bands that overlap with one another at a redshift represent datasets consistent with one another at that redshift. Globally, the mutual consistency between the CMB-Lyα-SN-LRG datasets and the ΛCDM cosmology can further be seen from the fact that the median is relatively featureless and has tight error bars. However, the H_0 measurement is not consistent with the other datasets. Note that the D_A and D_H medians are pulled to lower values and at $z = 0$ there is only a small overlap between the H0-Lyα dataset and the CMB-SN-LRG dataset.

A less obvious indicator of this inconsistency is seen in the relative size of the error bars for the CMB-SN-LRG data combination and the H0-Lyα-CMB-SN-LRG combination. If additional datasets are consistent with previous datasets, one would expect the GP from the union of the datasets to produce smaller error bars at all redshifts. This is not the case with the inclusion of the H0 dataset, implying some tension. Since the H0 dataset is trying to pull D_H below the fiducial value, the GP with the H0 combination favors larger values of the hyperparameter h, which controls the scale of the fluctuations of the GP regression, than without it. This in turn produces larger error bars at all redshifts.

In other words, the exact precision of the GP constraints is sensitive to the concordance between the datasets included in the analysis. Beyond the discrepancies for $z \simeq 0$, the

Cosmology	Data	D_H [Mpc]	D_A [Mpc]	Correlation
ΛCDM	TT	$(1.928 \pm 0.012) \times 10^{-1}$	$(1.275 \pm 0.005) \times 10^{1}$	0.964
	TT+lowP	$(1.920 \pm 0.011) \times 10^{-1}$	$(1.273 \pm 0.004) \times 10^{1}$	0.936
	TT+lowP+lensing	$(1.926 \pm 0.010) \times 10^{-1}$	$(1.276 \pm 0.004) \times 10^{1}$	0.952
	TT+TE+EE+lowP	$(1.919 \pm 0.007) \times 10^{-1}$	$(1.273 \pm 0.003) \times 10^{1}$	0.940
ΛCDM + N_{eff}	TT	$(1.848 \pm 0.047) \times 10^{-1}$	$(1.203 \pm 0.041) \times 10^{1}$	0.988
	TT+lowP	$(1.912 \pm 0.031) \times 10^{-1}$	$(1.266 \pm 0.023) \times 10^{1}$	0.981
	TT+lowP+lensing	$(1.919 \pm 0.029) \times 10^{-1}$	$(1.269 \pm 0.022) \times 10^{1}$	0.983
	TT+TE+EE+lowP	$(1.926 \pm 0.023) \times 10^{-1}$	$(1.278 \pm 0.016) \times 10^{1}$	0.987
ΛCDM	TT	$(1.820 \pm 0.072) \times 10^{-1}$	$(1.118 \pm 0.057) \times 10^{1}$	0.969
$+ \, \mathrm{d}n_{\text{s}}/\mathrm{d}\ln k$	TT+lowP	$(1.923 \pm 0.054) \times 10^{-1}$	$(1.287 \pm 0.039) \times 10^{1}$	0.974
$+ \sum m_\nu + Y_p + N_{\text{eff}}$	TT+lowP+lensing	$(1.913 \pm 0.053) \times 10^{-1}$	$(1.275 \pm 0.037) \times 10^{1}$	0.973
	TT+TE+EE+lowP	$(1.952 \pm 0.036) \times 10^{-1}$	$(1.297 \pm 0.024) \times 10^{1}$	0.990

Table 2.1: Hubble distances and angular diameter distances evaluated at the redshift of last scattering, $z_* = 1090$, along with their uncertainties and correlation coefficient, for each of the considered CMB datasets and cosmologies.

full data combination (H0-Lyα-CMB-SN-LRG) constrains the expansion history (both in D_H and D_A) to be consistent with the Planck ΛCDM cosmology at the 2% level up to the redshift of last scattering. It is worth noting that when the size of the relative errors on D_H are constant in redshift, the size of the relative errors on D_A tends to decrease with redshift. This is because D_A is the integral of D_H, and can be interpreted as the sum of N independent random $D_H(z_i)$ variables. As a result, the error on D_A grows as $\sqrt{N}$, while D_A grows as N, with the relative error decreasing as $1/\sqrt{N}$. This explains why, despite having no CMB constraint, the H0-Lyα dataset constraints on D_A are tightest at high redshifts.

2.3.1 Validation

We now show that our methodology is able to accurately infer non-standard cosmologies from mock data. Concretely, we consider a dark energy model with a time-evolving equation of state parameterized by $w(z) = w_0 + \frac{z}{1+z}w_a$ [77, 78]. We choose $\{w_0, w_a\} = \{-2, 1\}$ and keep the other parameters fixed to their fiducial values. This cosmology is an interesting choice for validation since, for large redshifts, the equation of state is close to the ΛCDM

value of -1, but begins to differ significantly at low redshifts. We use this cosmology to generate mock data and apply a GP regression on this data. The central values for the mock data are taken from the $D_H(z)$ and $D_A(z)$ for our $w_0 w_a$ cosmology, resampled by the covariances from each of the used datasets.

The results of this validation are shown in Fig. 2.3. The median of the GP regression is indeed not precisely the same as the input distances due to the resampling of the data. Any discrepancy between the input cosmology (black line, Fig. 2.3) and the median of the GP (orange line, Fig. 2.3) has only a small significance. The general features, such as the hump in both D_H and D_A at low redshift, of the input cosmology are recovered. In addition to demonstrating the ability of our GP regression to reproduce non-standard cosmologies, this validation shows that our main results are not particularly sensitive to the choice of fiducial model (that we divide out) since the recovered cosmology is substantially different from the fiducial cosmology.

2.3.2 Expanded parameter spaces

We have considered expanded and contracted covariances for the CMB data (to simulate new physics), specifically, by scaling the elements of the covariance matrix by a factor of two. The late-time constraints were insensitive to such changes in the covariance. We also explicitly considered expanded parameter spaces. We generated posteriors for $D_H(z_*)$ and $D_A(z_*)$ using CosmoMC [72] for three different model cases and four different data cases. The three model cases are ΛCDM, a minimal case where only the standard six parameters are varied $(\Omega_b h^2, \Omega_c h^2, \theta_{\mathrm{MC}}, \tau, n_s, \ln(10^{10} A_{\mathrm{s}}))$, a case where N_{eff} is also varied, and an extended case where the running of the scalar spectral index $\mathrm{d}n_{\mathrm{s}}/\mathrm{d}\ln k$, sum of neutrino masses $\sum m_\nu$, and primordial helium abundance Y_p are varied along with N_{eff}. The different CMB data cases include different combinations of the temperature (TT), low-ℓ polarization (lowP),

23

high-ℓ polarization (TE+EE), and lensing data. These results are listed in Table 2.1.

The additional parameters yield constraints on $D_H(z_*)$ and $D_A(z_*)$ with larger uncertainties relative to those from the base case. However, the inferred expansion history showed no significant deviations when using either the expanded or contracted covariance matrices. This is because there is no significant shift in the $D_H(z_*)$ and $D_A(z_*)$ values when the extra parameters are introduced, and changes to the median values are consistent with the expanded errors. This indicates that conclusions about late-time effects such as dark energy domination and the growth of structure are largely independent of the specific CMB constraint.

To isolate the effects of adding N_{eff}, we further examined the 'ΛCDM+N_{eff}' model separately. In particular, we focused on the 'TT' dataset that allows for the largest freedom; for this case the inferred value of $H_0 = 80.5^{+6.7}_{-9.0}$ km s^{-1} Mpc^{-1}. The error on the inferred $D_H(z_*)$ (see Table 2.1) and correspondingly on r_{drag} is also large in this case. This means that we need to propagate the changes in r_{drag} to the BAO distance measurements. To do so, we need a model for how r_{drag} varies with $D_H(z_*)$. To gain an understanding of the covariance between the cosmological variables when N_{eff} is varied, we perform the following exercise. We start with a ΛCDM model with $N_{\text{eff}} = 3.046$, increase N_{eff} and then discuss the changes to the cosmological parameters required to get the TT power spectrum back to the ΛCDM TT spectrum.

Increasing N_{eff} delays matter-radiation equality, i.e., decreases z_{eq} (redshift when matter and relativistic energy densities are equal). In order to obtain a good fit to the CMB data, we keep z_{eq} constant by increasing the physical matter density, $\Omega_{\text{m}}h^2$. In addition, decreasing the baryon fraction by a small amount (keeping $\Omega_{\text{m}}h^2$ fixed) to keep $k_D r_s$ constant, one can maintain the same relative damping of the peaks as the ΛCDM model [71].

To keep the peak positions unchanged, we have to decrease $D_A(z_*)$ commensurate with the
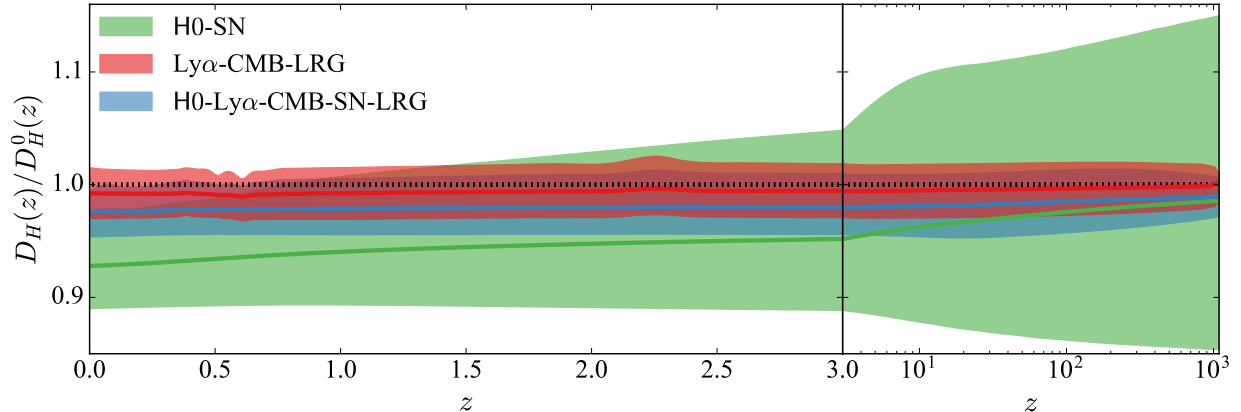
Figure 2.4: The GP results for D_H considering the 'ΛCDM + N_{eff}' case, using only the 'TT' constraint from the CMB. In green, we show the dataset combination that scales as a function of $D_H(0)$ (H0-SN). In red, we show the dataset combination that scales as a function of $D_H(z_*)$ (Lyα-CMB-LRG); see discussion in text. As before, blue corresponds to the full dataset combination (H0-Lyα-CMB-SN-LRG).

decrease in r_s (so that θ_s doesn't change), which can be accomplished by increasing the dark energy density. This necessitates a decrease in Ω_{m} to maintain a flat universe, which in turn requires an increase in H_0 to keep $\Omega_{\text{m}}h^2$ (and hence z_{eq}) unchanged. Using this model we find that the increase in H_0 is about 10%, roughly consistent with what we find from the full MCMC for the TT case. This analysis shows in a simple way why an increase in N_{eff} is correlated with an increase in H_0 or vice-versa [18, 45, 62].

In addition to these changes, we found that an increase in the spectral index of the primordial power spectrum (n_s) leads to a better match. This is also evident in the contours plotted in Fig. 20 of Ref. [18]. With these changes and a small shift in the overall normalization (allowed by the uncertainty in the optical depth measurement), the changes to the spectrum from increasing N_{eff} can be made smaller than cosmic variance at $\ell < 2000$. We have checked this explicitly using the Python version of CAMB [79].

Given this model, we can now predict the change to r_{drag}. At fixed z_{eq}, we have $D_H(z_*) \propto \sqrt{\Omega_{\text{m}}h^2}$ (assuming z_* changes are subdominant, which we verified). In addition, there is a correlated change in the baryon density $\Omega_b h^2$ and hence the sound speed, which implies that r_{drag} will not scale linearly with $D_H(z_*)$. For the model discussed above, we obtain

$r_{\rm drag} \propto D_H(z_*)^{1.3}$. The MCMC results showed a steeper correlation: $r_{\rm drag} \propto D_H(z_*)^{1.5}$. The small discrepancy implies that we are not capturing all the available freedom in this simple model.

Given the above discussion, we generated expansion histories for the TT-only case using the model $r_{\rm drag} = r_{\rm drag,fid}\left(D_H(z_*)/D_H(z_*)_{\rm fid}\right)^{1.5}$. We scaled the BAO distances (both D_A and D_H) by these $r_{\rm drag}$ values. This allows the large uncertainty in the CMB measurement for the TT-only case to impact the BAO measurements directly. The results of the GP regression using this model is shown in Fig. 2.4. We did not find clear evidence that varying $N_{\rm eff}$ alleviates the H_0 tension. Qualitatively, our results are in agreement with the findings of Ref. [45] who discussed tension in cosmological datasets while allowing for the primordial power spectrum to be a knotted spline function.

It is worth noting that the $r_{\rm drag}$ values allowed by the TT data when $N_{\rm eff}$ is free to vary do change the low redshift $D_H(z)$ inferences, but the changes at $z = 0$ are fairly minor. We ascribe this result to the fact that the decrease in D_H is not significant enough (about 1-σ given the expanded error) and that other low redshift measurements are consistent with Planck. We note that the CMB constraints in Table 2.1 are consistent with the findings of Ref. [62]. The key effect of varying $N_{\rm eff}$ is to enlarge the error on $D_H(z_*)$ (and hence $r_{\rm drag}$). Adding polarization or lensing data reduces the error on $D_H(z_*)$ and pushes the median back to its value in ΛCDM.

2.3.3 Forecasts

We can use our methodology to forecast future constraints on the expansion history. As an example, we consider including, in addition to current data (H0-Lyα-CMB-SN-LRG), information from the Dark Energy Spectroscopic Instrument (DESI, [80]). We use the projected uncertainties on D_H and D_A from the DESI Final Design Report [81] and generate the cen-
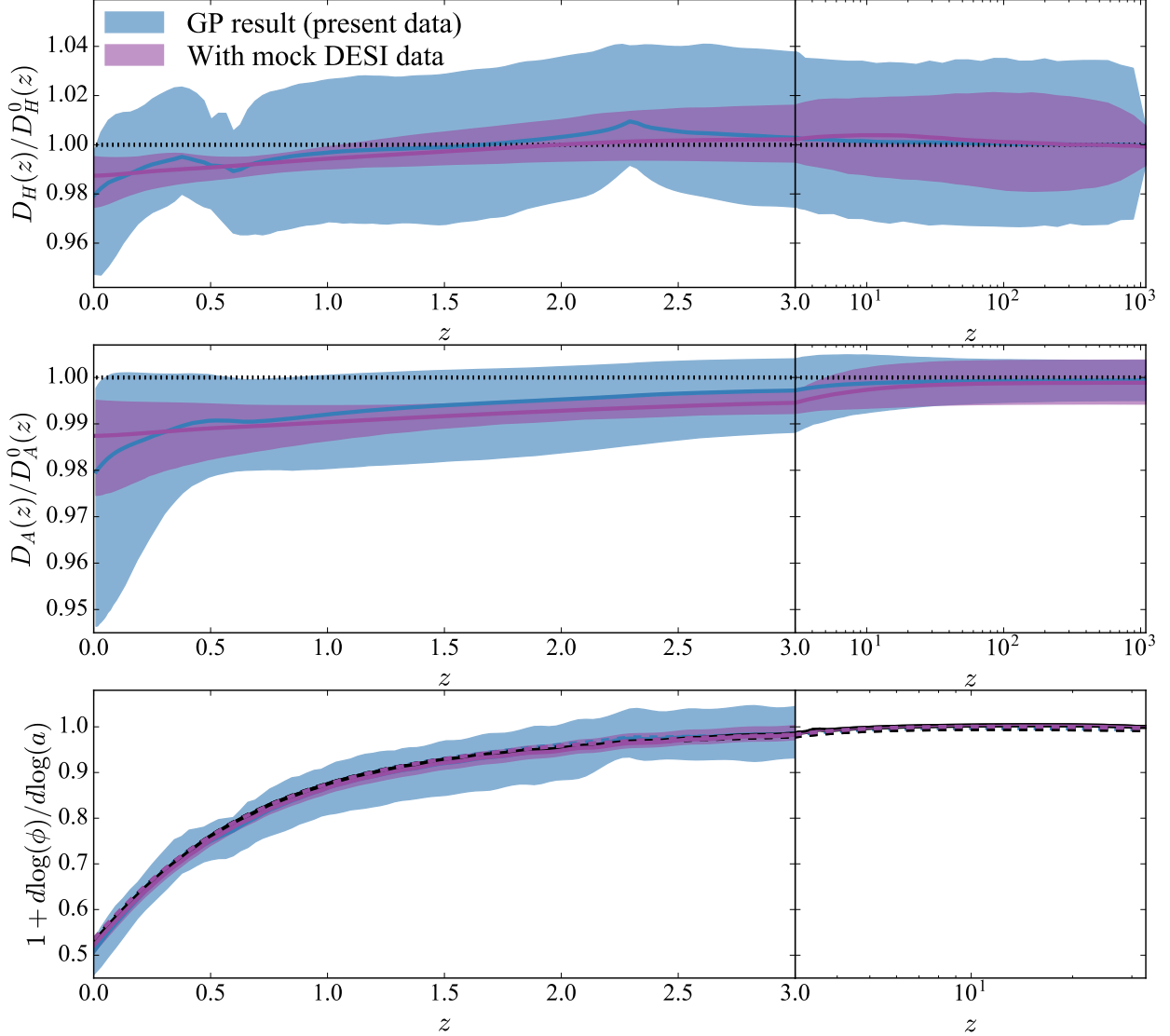
Figure 2.5: The results of the GP regression, now with the inclusion of mock data from the upcoming DESI experiment. The shaded regions correspond to the posterior probability of the expansion history with redshift, bounded at 90% CL. The blue curves and shaded regions represent the results from the H0-Lyα-CMB-SN-LRG dataset. The purple curves and shaded regions further include mock DESI data generated from the median values of the H0-Lyα-CMB-SN-LRG regression. The black curves show the fiducial values for the quantities in each panel. The Hubble distances are in the top panel, angular diameter distances are in the middle panel, and growth rates are in the bottom panel. The dashed lines in the bottom panel show $\Omega_{\rm m}^{\gamma}(z)$ for $\gamma = 0.52, 0.54$ for the GP result and DESI forecast result, respectively. The black dashed line shows the fiducial quantity $\Omega_{\rm m}^{0.55}(z)$.

tral values from the median values of the GP regression with the H0-Lyα-CMB-SN-LRG dataset. Accordingly, DESI spans 24 redshifts bins between $0.65 < z < 3.55$, and has errors on D_H and D_A on the order of $1 - 2\%$ for the lowest redshift bins and as large as 16% for

the highest redshift bin.

When the central values of the new data points are generated from the median result of the GP regression, the combination of the DESI data with the previous datasets yields a precision of $\lesssim 1\%$ across redshift, from the present to the last scattering surface. The tightest constraints in D_H are located around $0.5 < z < 1.0$ while in D_A they are around $1 < z < 4$, as seen in Figure 2.5. In the event DESI follows the trend of current data, it will discern deviations from the fiducial ΛCDM cosmology at above 90% CL for all redshifts $z < 1$ in D_H and all redshifts $z < 4$ in D_A. By contrast, without the DESI data, the only significant evidence for a deviation from ΛCDM occurs as a result of the H0 dataset close to $z = 0$.

It would also be possible to forecast the impact of future CMB or H0 experiments. As discussed earlier, a factor of two reduction in the covariance matrix for the CMB does not particularly affect the low-redshift constraints. Improved uncertainties from a future H0 experiment could lead to interesting new results, and we leave this for future work.

2.4 Late-time growth of the gravitational potential

An avenue for looking for deviations from General Relativity on large scales is the correlated evolution of the late-time growth of the gravitational potential and the expansion history. We can use the space-space perturbed Einstein equations [82] neglecting anisotropic stress and total pressure perturbation to write an equation for the gravitational potential:

$$\phi'' + (4 + H'/H)\phi' + (3 + 2H'/H)\phi = 0 \,. \tag{2.7}$$

If we enter the well-known solution for the ΛCDM model, $\phi \propto (H/a) \int (aH)^{-3} da$, we find that $3(H^2)' + (H^2)'' = 0$, where primes denote derivatives with respect to $\ln(a)$. This is satisfied if the expansion rate is of the ΛCDM form: $H(z)^2 = c_1(1 + z)^3 + c_2$ for constant c_1

28

and c_2.

Eqn. 2.7 can also be derived by starting with the assumption that the energy-momentum tensor is covariantly conserved and writing the perturbation equation for the total energy density at late times neglecting the radiation energy density and any anisotropic stresses. In addition, one needs to assume the hierarchy $k \gg \mathcal{H} \gg kc_{\mathrm{s}}^2$ so as to be able to use the Poisson equation and neglect total pressure perturbations. This way of deriving Eqn. 2.7 may be useful in thinking about modified gravity theories where the Poisson equation is modified or the two gravitational potentials (typically labeled ϕ and ψ [82]) are not equal [83, 84] but the energy-momentum tensor still satisfies the same conservation equations.

2.4.1 Inferring the growth history

We numerically solve Eqn. 2.7 for each generated expansion history in order to calculate the growth of the gravitational potential. We set the initial condition for this equation during the era of matter domination, specifically at $z = 30$, which explains the narrowing of the contours of the growth history at that redshift. Choosing to set the initial condition at this redshift only requires the assumption that new physics is important solely at late times. We store both the gravitational potential (ϕ) and its derivative encapsulated in the growth rate $f = 1 - d\ln(\phi)/d\ln(1 + z)$. As noted previously, the distance constraints determine a weight for each expansion history sampled by the GP. The quantities ϕ and f, calculated for each sampled expansion history, are given this same weight, which allows us to calculate posteriors for ϕ and f.

A comparison of the growth function $D(a) = a\phi(a)$ to its measurement from the Dark Energy Survey (DES), South Pole Telescope (SPT), and Planck is shown in Fig. 2.6. These measurements are obtained by cross-correlating lensing maps of the CMB from Planck and SPT with galaxy maps from DES [1]. The errors on the growth function from galaxy clus-

tering and galaxy-CMB lensing correlations are currently large, and broadly consistent with our inference from the expansion history. There is mild evidence that the measured growth function is systematically lower than the inferred one, and this provides an interesting target for future observations.

We have also investigated the redshift evolution of the growth rate. It is well known that, in GR, $f(z)$ can be accurately modeled by $\Omega_{\mathrm{m}}(z)^\gamma$ with $\gamma \simeq 0.55$ [85, 86], where $\Omega_{\mathrm{m}}(z) \equiv \Omega_{\mathrm{m}}(0)(1 + z)^3(H_0/H(z))^2$ is the matter density assuming the energy-momentum tensor of the matter component is separately conserved.

In our model-independent method, $\Omega_{\mathrm{m}}(0)$ is not defined, so we start with the physical matter density at last scattering. Specifically, for each of the expansion histories generated by the GP, we calculate the value of the Hubble parameter at $z = z_*$, use that to obtain the total energy density at that redshift assuming GR, and then subtract off the energy density in radiation as defined by the fiducial model. We interpret the remaining quantity as the physical matter density at $z = z_*$. This physical matter density is then scaled to the critical density at other redshifts computed from the expansion histories as

$$\Omega_{\mathrm{m}}(z) = \left(\frac{3H^2(z_*)}{8\pi G} - \rho_{\mathrm{r,fid}}(z_*) \right) \left(\frac{1+z}{1+z_*} \right)^3 \frac{8\pi G}{3H^2(z)}. \tag{2.8}$$

The benefit of this method is it maintains the model-independence at late times. The drawback is the need to make specific assumptions to obtain the matter density at last scattering. In particular, we need information about the energy density in relativistic degrees of freedom to determine the matter density. This can be done in a manner that is independent of late-time cosmology since the phase shift of the acoustic peaks [87, 88] and the damping tail [89, 71] in the CMB allow us to infer the energy density in non-interacting relativistic degrees of freedom [90, 91]. These observables in the angular power spectrum are determined by the evolution of the gravitational potential and expansion history at early times. In particular,
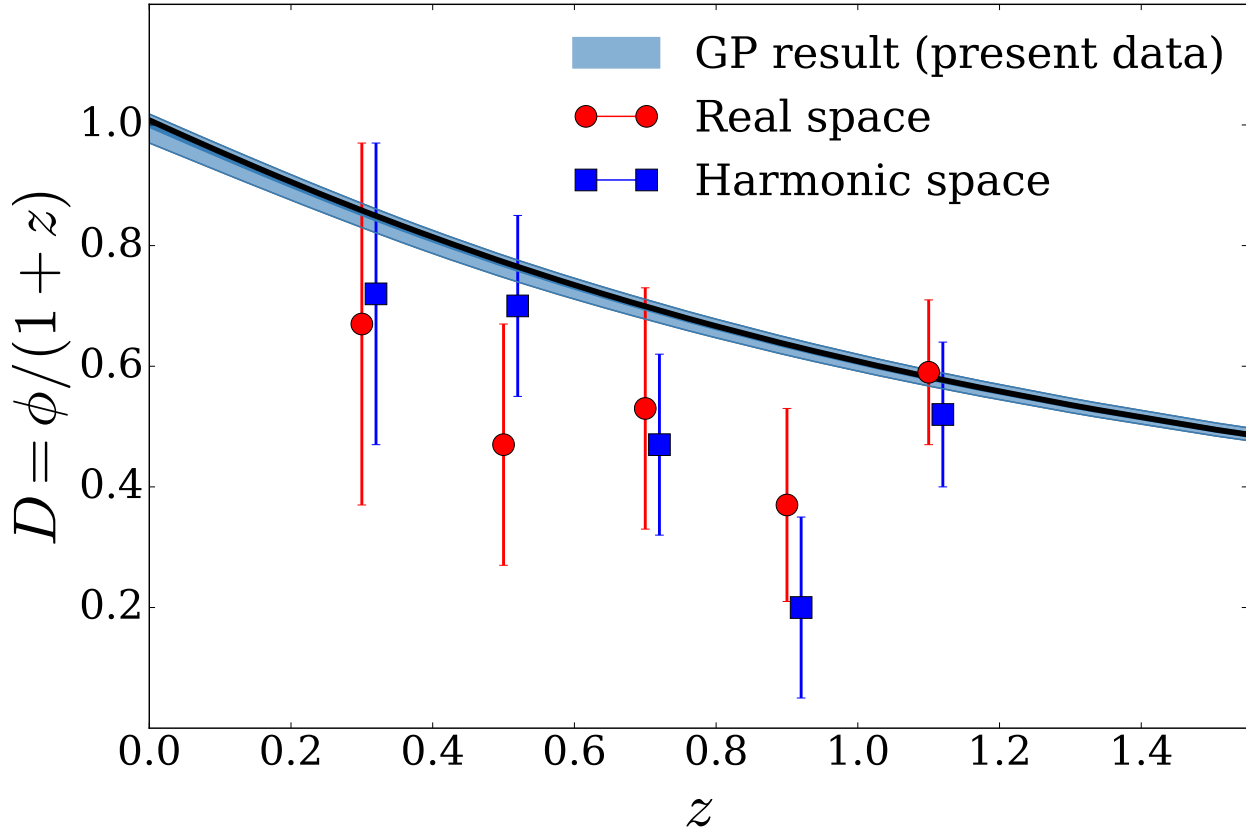
Figure 2.6: The evolution of the gravitational potential multiplied by the scale factor where the median of the GP regression is normalized to unity at the present time and compared to galaxy clustering and galaxy–CMB lensing data from a joint analysis of DES, SPT, and Planck [1] (all shown at 68% CL). The GP result considers the full H0-Lyα-CMB-SN-LRG dataset (light blue). The black line corresponds to the fiducial ΛCDM cosmology. The difference between the red and blue points is that the former are calculated from an estimator of the growth function based off the two-point correlation function (real space), while the latter are calculated from a growth function estimator based off the angular power spectrum (harmonic space). Hence, they represent different techniques to calculate the same quantity.

the damping of the peaks is set by $k_D r_s$, which is manifestly independent of the low-redshift expansion history. The phase shift is proportional to $f_\nu \Delta \ell_{\mathrm{peak}}$, where f_ν is the fraction of energy density in non-interacting relativistic degrees of freedom (including standard model neutrinos) and $\Delta \ell_{\mathrm{peak}}$ is the spacing of peaks for modes that entered the horizon during radiation domination, first measured in the Planck 2013 data [88, 92]. These arguments suggest that we can measure N_{eff} without degeneracy with the late-time expansion of the Universe.

Currently, there is no strong evidence for dark radiation. In computing $\Omega_{\mathrm{m}}(z)$, we use the standard cosmological radiation energy density (CMB photons and three massless active neutrinos). The constraints on $f(z)$ are shown in Figures 2 – 4, and are consistent with the expectation that $f(z) = \Omega_{\mathrm{m}}^{\gamma}(z)$ with $\gamma = 0.55$, with a precision of $3 - 4\%$ across redshift using the full combination of current data (H0-Lyα-CMB-SN-LRG). This is not surprising since the expansion history is consistent with the fiducial history. Future surveys like DESI will have the power to substantially improve the constraints, reducing the uncertainty on the growth history to roughly 1%, and increasing the prospects for detecting deviations from the General Relativistic expectation.

2.4.2 Dark energy equation of state

To obtain a sense of the effective dark energy density, we compute the remaining energy density when the matter and radiation energy densities are subtracted from the critical density. This remaining energy density can be viewed as the dark energy density in a flat cosmology, independent of specific parameterizations for the dark energy equation of state. We define the physical energy densities in matter and radiation in the manner as described above, and compute the effective dark energy density as

$$\rho_{\mathrm{DE}}(z)/\rho_{\mathrm{crit},0} = \left(\frac{3H^2(z)}{8\pi G} - \rho_{\mathrm{m}}(z) - \rho_{\mathrm{r,fid}}(z) \right) \frac{8\pi G}{3H_0^2}. \tag{2.9}$$

This approach implicitly sets the dark energy density to be zero at the redshift of last scattering. Figure 2.7 shows that the inferred dark energy density from current data is consistent with a cosmological constant ($w = -1$) at low redshifts, with a precision of 2%, 6%, and 13% at $z = 0$, 0.5, and 1.0, respectively. As expected, the dark energy constraints successively degrade towards even larger redshifts. The H0 dataset induces some evolution near $z = 0$, but it is small compared to the uncertainties in the inferred dark energy density.
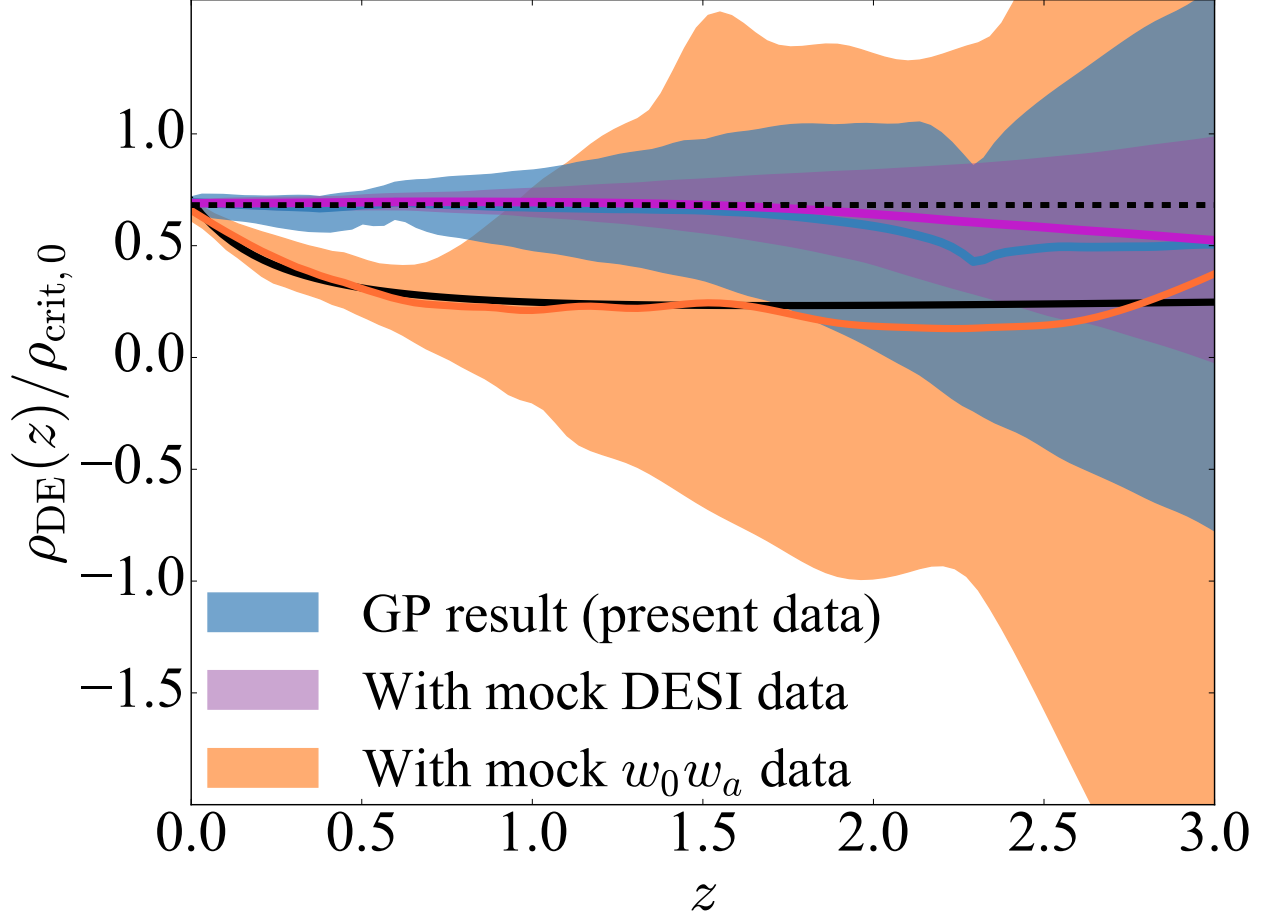
Figure 2.7: The dark energy density scaled to the present critical density as a function of redshift, as inferred from the expansion histories. The shaded regions correspond to the posterior probability of the dark energy density at that redshift, bounded at 90% CL. We consider the full H0-Lyα-CMB-SN-LRG dataset combination in blue, and further include forecasted DESI data in purple. In orange, we consider mock data generated from a $w_0 w_a$ cosmology, illustrating that the analysis can recover the dark energy evolution of non-standard cosmologies. The solid black line corresponds to the input $w_0 w_a$ model, and the dashed black line is for the ΛCDM expectation.

The inclusion of DESI would reduce the errors by a factor of two to three across redshift, allowing for even more stringent tests of the dark energy equation of state.

In Figure 2.7, we moreover consider restricting the analysis to mock data generated from a $w_0 w_a$ cosmology (same model as in Section 2.3.1), and illustrate that the GP regression is able to recover its dark energy evolution. We find that the size of the errors on the reconstructed dark energy density is sensitive to whether the dark energy is the dominant

component of the energy density. When the dark energy density is subdominant to the matter component, the model independent reconstruction has no strong preference for different values of $\rho_{\mathrm{DE}}(z)/\rho_{\mathrm{crit},0}$, and allows for large errors. Hence, the mock $w_0 w_a$ cosmology has larger errors than the GP result from present data (despite having the same covariance) as the dark energy in this $w_0 w_a$ cosmology dominates later in time.

2.5 Conclusions

We have presented a method for analyzing measurements of the expansion history of the Universe that is independent of cosmological models. To achieve this, we inferred the expansion history using GP regression and showed that the Planck CMB temperature, BOSS luminous red galaxies, BOSS Lyman-α, and JLA Type Ia supernova datasets are consistent with one another and with ΛCDM. The tension between the local Riess et al. (2016) and inferred Planck measurements of the Hubble constant that has been pointed out in the context of ΛCDM is also apparent in our model-independent analysis. Our analysis did not find evidence that the presence of dark radiation alleviates this tension, leaving open the possibilities for new late-time physics or systematic effects. Beyond $z \simeq 0$, the full combination of datasets constrain the expansion history with a precision of 2% to the redshift of last scattering, restricting the range of viable non-standard cosmologies.

We derived the growth rate for the fluctuations on sub-horizon scales from the expansion history in a model-independent manner, and showed that it is consistent with the ΛCDM expectation at the $\lesssim 4$% level from the present to the matter dominated era. We have not added independent measurements of the growth rate in this work, but doing so in the future will allow more robust tests of deviations from GR. We further constrained the dark energy density with a precision of 2% at $z = 0$ and roughly 10% by $z = 1$, and found it to be constant across redshift in agreement with the cosmological constant scenario.

We forecasted how the significance of our constraints change with the upcoming DESI experiment. By including DESI in addition to current data, we will be able to improve the constraints on the dark energy density by up to a factor of four, and infer the expansion and growth histories at the percent level from the present to the era of matter domination. This level of precision is encouraging given the model-independent nature of our analysis.

Chapter 3

A Bright Gamma-ray Galactic Center Excess and Dark Dwarfs: Strong Tension for Dark Matter Annihilation Despite Milky Way Halo Profile and Diffuse Emission Uncertainties

3.1   Introduction

The Milky Way's Galactic Center (GC) is a exceedingly crowded region with numerous gamma-ray point sources and several sources of diffuse emission. It is also expected to contain a high density of dark matter, which makes it an promising place to search for signals of dark matter annihilation or decay. Weakly Interacting Massive Particles (WIMPs) are among the leading candidates for dark matter, due to a natural mechanism for their

thermal production at the proper density in the early Universe. Supersymmetric extensions to the standard model of particle physics can easily accommodate a WIMP [93].

In previous work, several known sources of gamma-ray emission toward the GC have been detected and modeled. There are 18 gamma-ray sources within the the the $7° \times 7°$ region about the GC within the Second Fermi Gamma-ray LAT Source Catalog (2FGL). For example, the gamma-ray point source associated with Sgr A* is one of the brightest sources in the region and its emission in this band can be modeled as originating from hadronic cosmic rays transitioning from diffuse to rectilinear propagation [94]. There is an abundance of gamma rays associated with bremsstrahlung emission from $e^{\pm}$, as mapped by the 20 cm radio map of the GC [95]. There is also Inverse Compton (IC) emission that is consistent with coming from the same $e^{\pm}$ source as the bremsstrahlung emission [96]

After considering known sources of gamma-ray emission, there remains an extended excess [97, 98, 99, 100, 101, 3, 102, 5, 4]. This Galactic Center Extended (GCE) excess signal gained significant interest since it may be consistent with a WIMP dark matter annihilation model. Primarily, the spatial profile of the excess is consistent with the expected profile from dark matter halos in galaxy formation simulations. Secondly, the strength of the signal implies an interaction cross section that is consistent with the thermal relic cross section. And thirdly, the spectra of the excess signal is consistent with a WIMP with a mass between 10-50 GeV that decays through quark or lepton channels. This triple consistency of the WIMP paradigm as an explanation of the GCE has gained significant attention.

Of course, there exist other candidates for the GCE gamma-ray emission. For instance, there is a large population of compact objects which can be bright gamma-ray sources. The GC Central Stellar Cluster can harbor a significant population of millisecond pulsars (MSPs). Since MSPs can have a spectra similar to low-particle-mass annihilating WIMPs, their presence can confuse a dark matter interpretation of the GC emission [103, 104]. Significantly, flux PDF methods have found evidence that point sources are more consistent with the GCE

flux map than a smooth halo source [105, 106].

If annihilating dark matter explains the GCE, then there should be annihilation signals in other places that have a high density of dark matter. Two such places are the "inner Galaxy" (within $\sim 20°$ of the GC) and the dwarf satellites of the Milky Way. Previous work has found that the inner galaxy signal is consistent with the mass and cross section supported by the galactic center [5, 4]. We will show the Milky Way dwarf galaxies' lack of a signal [107, 2] significantly constrains the GC parameter space. However, there is a reported excess from the newly discovered Reticulum 2 dwarf galaxy that may be consistent with the GC annihilation signal [108]. We will discuss below what would be required to have the GCE signal be consistent with the dwarf galaxy limits.

Previous analyses have largely used fixed values for the parameters of the Milky Way's dark matter halo when inferring dark matter particle properties that could produce the GCE. There exists significant uncertainty in these parameters, which translates into large errors on the cross section of dark matter annihilation, while background emission modeling uncertainties in the crowded GC region largely generate uncertainties on the dark matter particle mass. In this paper, we perform a Bayesian analysis of the full GCE likelihood in order to more properly quantify the uncertainties on the nature of dark matter that may produce the GCE signal. Gaussian and chi-squared statistics are often used in other work for dark matter fits to the GCE spectra. Such approximations are inaccurate due to the Poisson nature of the photon count signal, and the inaccuracy is increased when convolved with Milky Way halo uncertainties. To assist in particle model fits to the GCE, we also provide the tools necessary to accurately calculate these uncertainties for general dark matter annihilation models with arbitrary spectra.[1]

---

[1]`https://github.com/rekeeley/GCE_errors`
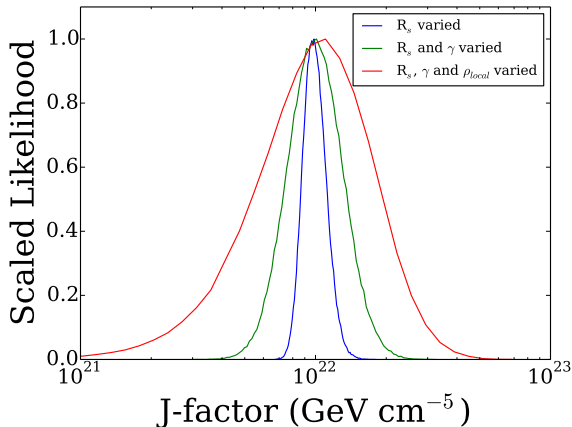
Figure 3.1: Plotted is the scaled likelihood for the galactic center's J-factor for our ROI given relaxation of the constraints on the Milky Way dark matter halo, as described in the text.

3.2   Data and Model Components

The data set that we will refer to as the 'IC' data set is taken from the analysis in Ref. [96]. It is generated with Fermi Tools version `v9r33` to study Fermi LAT observations from August 2008 to June 2014 (approximately 70 months of data). This data is from Pass 7 rather than Pass 7 Reprocessed instrument response functions since the diffuse map associated with the latter have strong caveats for use with new extended sources. This analysis simultaneously fits the amplitude and spectrum of point sources from the 2FGL catalog [109], plus four other point sources in the ROI. It uses $0.2 - 100$ GeV photons in 30 logarthmically-spaced energy bins, with `ULTRACLEAN`-class photon selection. The IC data-set includes the 20 cm radio template as a tracer of gas to account for the bremsstrahlung emission as has been done previously [95, 102, 110]. It also includes IC emission from starlight with a 3.4 μm template from the WISE mission [111]. The IC data set also includes the New Diffuse (ND) map whose intensity is sub-dominant to the bremsstrahlung map and increases with angle away from the GC. The ND template is that described in Ref. [110], and is interpreted as accounting for additional bremsstrahlung emission not captured in the 20 cm map. The IC data set optimized the morphology of the GCE excess and ND templates to their best-fit

profiles. The GCE excess, used templates of density $\rho(r)^2$ projected along the line-of-sight with $\rho(r) \propto r^{-\gamma}(r + r_s)^{-(3-\gamma)}$. The IC data analysis found that $\gamma = 1$ provided the best-fit. In this IC data set, all the 4 extended sources (GCE, ND, IC, Bremsstrahlung) were given generic log-parabola spectral forms with four free parameters each. The analysis detected the WISE 3.4 μm template at very high significance of TS = 197.0[2]. The previously studied sources were also detected at high significance. The GCE was detected with TS = 207.5, bremsstrahlung was detected with TS = 97.2.

We adopt 'noIC' and 'noB' data sets from the analysis in Ref. [110]. These data sets were analyzed in a similar manner to the 'IC' data, except the the 'noIC' data set does not include the inverse Compton background template, and the 'noB' includes neither the inverse Compton template nor the 20 cm radio template. Both these data sets cover the same $7° \times 7°$ ROI as the 'IC' set, but use `SOURCE`-class photons. They use Fermi Tools version `v9r31p1` to study Fermi LAT data from August 2008 to May 2013 (approximately 57 months of data), and they use Pass 7 instrument response functions.

3.3 Analysis

The signal strength of annihilating dark matter in the GC depends on the density profile of the Milky Way's dark matter profile. We the choose dark matter density to have the generalized Navarro-Frenk-White (NFW) profile of the form [112, 113]:

$$\rho(r) = \frac{\rho_\odot}{\left(\frac{r}{R_\odot}\right)^\gamma \left(\frac{1+r/R_s}{1+R_\odot/R_s}\right)^{3-\gamma}}, \tag{3.1}$$

where $R_\odot$ is the Sun's distance from the center of the Milky Way, $\rho_\odot$ is the density of the dark matter halo at $R_\odot$, R_s is the scale radius of the Milky Way's dark matter halo, and γ

---

[2]TS $\equiv 2\Delta \ln \mathcal{L}$, where $\Delta \mathcal{L}$ is the difference of the best fit likelihood with and without the source. For point sources, a value of TS = 25 is detected at a significance of just over 4σ [109].

is a parameter characterizing the slope of the inner part of the profile.

To arrive at substantially more accurate errors on the inferred dark matter particle mass and cross section from the GCE signal, we employ a Bayesian analysis to propagate uncertainties in the dark matter halo to uncertainties in the particle annihilation parameters. Bayesian techniques have a formally straightforward method to include the effect of these nuisance parameters, namely to integrate the likelihood over the subspace of those nuisance parameters:

$$\mathcal{L}(\theta|x) = \int dn \ \mathcal{L}(\theta, n|x). \tag{3.2}$$

This defines our approach for this analysis: calculate the full likelihood then marginalize over the nuisance subspace to get the likelihood as a function of the dark matter mass and cross section. The errors are then contours of $\Delta\mathcal{L}$.

The random observable that is used in our Bayesian analysis is the gamma-ray number counts binned by energy. Such number counts have Poisson statistical errors. Hence, to do the Bayesian analysis, it is appropriate to use a log-likelihood of the form:

$$\log(\mathcal{L}) = \sum_i k_i \log \mu_i - \mu_i, \tag{3.3}$$

up to factors that do not involve the model parameters. Here, k_i is the observed number of events in the i-th energy bin and μ_i is the expected number of events from the model in that energy bin. The expected number count in bin i has two components, one associated with the dark matter annihilation, and one associated with background sources. The dark matter number count is given by the integral of the spectra of the number flux over the energy bin, multiplied by the exposure of the i-th bin:

$$\mu_i = b_i + \epsilon_i \int_{E_i}^{E_{i+1}} \frac{d\Phi}{dE} dE, \tag{3.4}$$

where b is the modeled background counts, ϵ is the exposure, $d\Phi/dE$ is the differential number flux, and the integral is over the energy bin from the observed number counts. The differential flux is given by:

$$\frac{d\Phi}{dE} = J\frac{\langle\sigma v\rangle}{8\pi m_\chi^2}\frac{dN}{dE}.\tag{3.5}$$

Here, $\langle\sigma v\rangle$ is the cross-section, m_χ is the mass of the dark matter particle, dN/dE is the per annihilation spectra, and the J-factor is the integral of the square of the dark matter density along the line of sight

$$J(\theta,\phi) = \int dz\ \rho^2(r(\theta,\phi,z)).\tag{3.6}$$

We use the package `PPPC4DMID` to generate the prompt annihilation spectra dN/dE [114].

The largest uncertainties on dark matter particle parameters arise from Milky Way halo parameters. It is the Milky Way halo parameters, $\rho_\odot, \gamma$, and R_s, that need to be marginalized over. The Milky Way halo parameters are determined either from direct observational constraints, such as that for $\rho_\odot$ and γ, or from that expected for dark matter halos in simulations, for R_s, since no significant observational constraint exists on this scale. The dependence on R_s and its uncertainty, as we shall show, is not significant.

A robust determination of the local dark matter density is derived from modeling the spatial and velocity distributions for a sample of 9000 K-dwarfs from the SDSS by Zhang et al. [115]. The inferred value for the local dark matter density from that work is $\rho_\odot = 0.28\pm0.08$ GeV cm^{-3}, and we employ the exact likelihood from that analysis. This local density is consistent with several other determinations [116]. A very recent determination of the local stellar density by McKee et al. [6] from star counts finds a significantly lower total stellar mass density than the dynamical stellar density profile measures of Refs. [115, 117, 118]. When the lower stellar density is combined with determinations of local total mass densities,

McKee et al. find a higher local dark matter density $\rho_\odot = 0.49 \pm 0.13$ GeV cm^{-3}. The error in McKee et al. of $\sigma(\rho_\odot) = 0.13$ GeV cm^{-3} is determined through the variation in total mass density determinations and is not from a full error analysis. Therefore, both the error and central value on the density from star counts are approximate. McKee et al. [6] also state that the dynamical estimates of the local density like that in Refs [115, 117, 118] are the "cleanest determinations of the local dark matter density," which agrees with our choice of the current most robust determination of the local dark matter density to be coming from Zhang et al. [115].

The constraints on the Milky Way halo scale radius are derived from the concentration, defined as $c \equiv R_{vir}/R_s$. The concentration of a halo describes the scale at which the slope of the profile of the halo changes from γ to 3, and it has some scatter associated with it [119]. We adopt the halo concentration's dependence on the mass of that halo as parameterized by Sanchez-Conde & Prada [120]. The concentration is log-normally distributed with an error of 0.14 dex so the prior likelihood for the scale radius is of the form:

$$\log \mathcal{L} = -\frac{(\log_{10}(R_{vir}/R_s) - \log_{10} c(M_{vir}))^2}{2 \times 0.14^2}. \tag{3.7}$$

The inner profile of the Milky Way halo within the inner $\lesssim 500$ pc relevant for the GCE is not well determined by dynamical data, or numerical results, since the region becomes baryon-density dominated. However, the profile is constrained by the observed GCE itself. on the slope of the inner profile, γ. In the analysis including bremsstrahlung emission, Abazajian et. al. [110] find $\gamma = 1.12 \pm 0.05$. When including the newly discovered IC component, the best fit profile shifted to $\gamma = 1.0$ with comparable errors [96].

To demonstrate the effect of allowing the parameters of the Milky Way's dark matter halo to vary, we plot in Fig. 3.1 the likelihood of the J-factor derived from the relaxing the values of the local density, scale radius, and slope of the inner profile. The width of the likelihood

distribution of the J-factor expands the posterior likelihood of the dark matter particle mass and cross section relative to using fixed values for the halo parameters. As Fig. 3.1 shows, varying the local density accounts for most of the width of the J-factor likelihood, though varying the scale radius and the inner profile slope also widens the likelihood. The J-factor likelihood is approximately a normal distribution as it is dominated by an approximately normal distribution in the $\rho_\odot$ uncertainty, and sub-dominant log-normal R_s and normal γ distributions.

Instead of integrating likelihoods over the nuisance subspace, which is computationally expensive, we maximize the log-likelihood over that subspace. Since the likelihood functions are approximately Gaussian ($\rho_\odot$ and γ) or log-normal (R_s) in the nuisance parameters, this is expected to be a good approximation. We have tested that this approximation is valid by explicitly integrating the likelihoods for single parameter dimensions. We explicitly calculate the probability contained within some $\Delta \log(\mathcal{L})$ by integrating the likelihood to find the 68%, 95%, and 99.7% and 99.99997% confidence regions for our plotted results. We determine the uncertainty regions of the particle mass and cross section parameter space for both b-quark and τ-lepton annihilation channels, as shown in Fig. 3.2. In the next section, we investigate the systematic uncertainty associated with uncertainties in the background-dominated low energy data portion of the GCE, as well as uncertainties introduced by incorporating or excluding different background diffuse emission models, including the bremsstrahlung excess and IC component.

Further, the concentration, which sets the scale radius, will change with varying halo mass. However, over a wide range of halo masses ($5 \times 10^{11} - 10^{14}$ M$_\odot$) the concentration varies only by an amount less than the statistical variation of the concentration: 0.14 dex. Hence, we neglect the additional uncertainty associated with varying the halo mass.
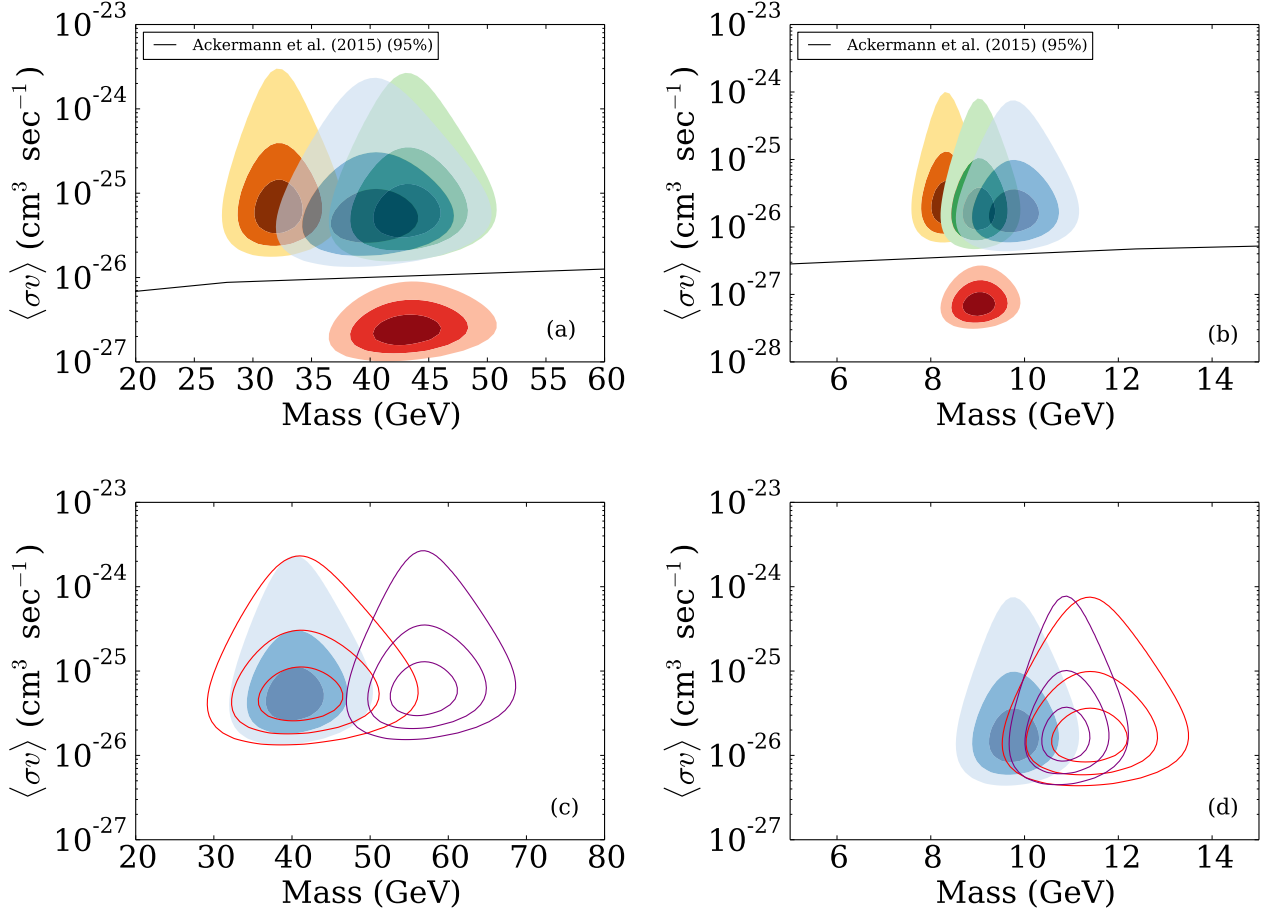
Figure 3.2: In (a) & (b), we plot contours of the Δlog-likelihood that correspond to 68%, 95% and 99.7% confidence regions for the full IC, noIC, and noB data sets, when marginalizing over Milky Way halo uncertainties, which demonstrate the systematic errors involved in the inclusion of diffuse sources in the GC; (a) is for the $b/\bar{b}$-quark channel and (b) is for the $\tau^\pm$ channel. The full IC model is shown in blue, noIC is in orange, and noB is in green. We also show, in red contours, an extreme high-concentration/contraction Milky Way halo model that would escape dwarf galaxy limits, but would be in conflict with local density and Milky Way halo simulations. We also show the 95% limits from dwarf galaxy searches by Ackermann et al. [2]. In the (c) & (d), for the $b/\bar{b}$-quark and $\tau^\pm$ channels respectively, we plot contours of the Δlog-likelihood that correspond to 68%, 95% and 99.7% for different numbers of low-energy bins excluded, demonstrating GCE spectrum determination systematic uncertainties in our method. The red contours are those derived from excluding data below 2.03 GeV, blue from excluding data below 1.24 GeV, and purple with a 0.764 GeV cut. The blue contours are for our optimal GCE spectrum determination, as described in the text.

3.4 Background Diffuse Emission Model Dependence

We test the model dependence associated when including or excluding emission from astrophysical backgrounds, including the detected bremsstrahlung diffuse excess component and IC components producing gamma-ray emission within the GC. Since the morphology of these sources is not known a priori, there is a significant systematic uncertainty introduced by the templates adopted as the model of these diffuse sources. To bracket this model uncertainty, we take extreme cases where the model components are either present or not. Our full model in this work includes all components: the 20 cm bremsstrahlung, IC, and GCE templates, as well as new diffuse and point sources as described in Abazajian et al. [96]. The noIC (denoted 'full' in Abazajian et al. [110]) model includes everything from the full model except the IC component. The noB model neglects the contribution from the 20 cm template, in addition to neglecting the IC component. Including different gamma-ray source templates shifts the best fit values of the mass, bracketing a large part of the model dependence of the GCE emission, as shown in the upper panels of Fig. 3.2. The dependence largely in particle mass in our diffusion uncertainties and not annihilation rate comes from the well-determined nature of the GCE total flux at ≈ 3 GeV even for various diffuse model and GCE spectral cases, as shown in Fig. 4 and Fig. 10 of Ref. [110]. Our adopted full model fit is shown in solid colors, with the contours representing an estimate of background uncertainties.

Additional systematic effects are associated with the low-energy data points. The full low-energy data in the GCE are generally not sensitive to variations in the assumed dark matter spectra since dark matter is sub-dominant to the background components at low energies (< 1 GeV); see, e.g., Fig. 6 of Ref. [110]. Since we are not performing a full template and point source fit in this analysis, we approximate the sub-dominant nature of these low-energy data points by excluding those that are below the flux of other diffuse sources from our fits. In full template fits of Refs. [110, 96], the sub-dominant flux of the GCE portion of the template at low energies does not contribute significantly to the total fit likelihood. Including all of

these points biases the best fit masses since the GCE errors at low energy underestimate the full model error, and shift the best fit dark matter particle mass determinations relative to the full template analysis from the same data in the full template and point source analyses. We investigate the bias effect by varying the the number of low-energy data points included in the analysis. We iteratively exclude points below 0.764 GeV, 1.24 GeV, or 2.03 GeV. Variation of the low-energy data point inclusion shifts the best fit mass by approximately 10 GeV for the b-quark annihilation channel, and by around 2 GeV for the τ-lepton annihilation channel, as shown in the lower panels of Fig. 3.2. Including all the lower energy data shifts to higher particle mass for the fit. Our best estimate of the subset that represents the full template and point source analysis is where the data simultaneously dominates above the background sources at $\gtrsim$ 1 GeV, becomes less sensitive to the number of points included, and provides optimal sensitivity to the particle mass, as shown in Fig. 3.2. The optimal case is shown in solid colors.

Given that the parameter space for the GCE signal is significantly constrained by searches for annihilation in dwarf galaxies, particularly in the Pass 8 analysis of Ref. [2], we explore the type of alteration of the Milky Way halo marginally consistent with dynamical measures and allowing for a significantly larger integrated J-factor toward the center of the galaxy: first, we take the local density to be $\rho_\odot = 0.4$ GeV cm^{-3}, which is 1.5σ away from the constraints from Zhang et al. [115]; and second, we adopt the concentration to be an extreme $c = 50$, which forces the scale radius of the Milky Way to be within the $R_\odot$, boosting the inner galaxy density. Increasing the concentration approximates a new scale possible in the dark matter halo from baryonic effects.

NFW halos are potentially modified by the presence of baryons via adiabatic "contraction" of the halos. Therefore, we also explore this enhancement with the CONTRA tool provided by Ref. [121]. Qualitatively, the contracted profiles give a new effective scale radius close to $R_\odot$, and a significant enhancement of density within $R_\odot$, up to factors of $\sim$1.5. This
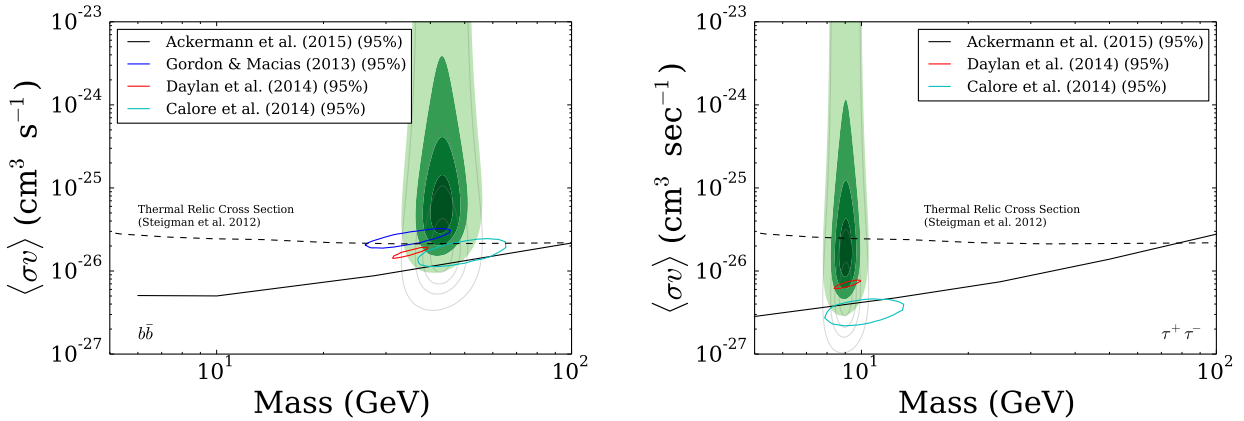
Figure 3.3: Plotted are contours of the Δlog-likelihood that correspond to 68%, 95%, and 99.7% and 99.99997% confidence regions when marginalizing over Milky Way halo uncertainties, in our best estimates for background uncertainties. Counter to the expectation that a symmetric error becomes asymmetric in a logarithmic plot, with larger extent downward, the error regions are asymmetrically oriented upward due to the anti-correlation of the J-factor with the annihilation rate $\langle\sigma v\rangle$. We also show the 95% limits from the dwarf galaxy annihilation search by Ackermann et al. [2], and the signal regions as presented in Refs. [3, 4, 5]. We also show, in light gray, the respective approximate error contours from the inferred approximate dark matter density in the low stellar density star count measures of Ref. [6]. The b-quark annihilation channel is on the left and the τ-lepton annihilation channel is on the right.

boosts the J-factor by $\sim$6, with a commensurate reduction in the necessary $\langle\sigma v\rangle$ by that amount. Therefore, the "extreme" high-concentration NFW case we propose could be close to that plausible in some cases of contracted profiles. Though the NFW parameters in a pure NFW sense are extreme, the overall J-factor result is within the realm of possibility in contracted profiles. A full scan of halo contraction involves an analysis that exceeds the current tools like CONTRA, and is beyond the current scope of the paper. The "high-concentration/contraction" case shown in Fig. 3.2 is plausible when considering particle physics models that directly escape the dwarf galaxy bounds.

3.5 Discussion and Conclusions

As the contours using the full model show, allowing the local density to vary increases the errors greatly along the cross section axis, leaving the mass axis less constrained. This is because the effects of cross section and the J-factor–and by extension the local density, scale radius, and inner profile slope–are exactly inversely degenerate when fitting the data. In particular, the inverse correlation between dark matter density and $\langle \sigma v \rangle$ extends the error region asymmetrically. This is contrast to a symmetric error in log-space, which would extend asymmetrically downward. This illustrates the importance of a full error analysis in quantifying uncertainties.

We also examine the background model dependence and low-energy intensity uncertainty, which shifts the particle mass in a systematic fashion, at the level of up to 10 GeV, depending on the overall level of these systematic uncertainties. We calculate the best fit dark matter particle mass and interaction cross section implied by the GCE that takes into account the uncertainties in the Milky Way's halo parameters and background model uncertainties. When adopting our best estimate models for the Milky Way halo and background diffuse emission models, we found for the b-quark annihilation channel that

$$m_\chi = 43. \left(^{+2.1}_{-1.9} \text{ stat.} \right) (\pm 19. \text{ sys.}) \text{ GeV}, \tag{3.8}$$

$$\langle \sigma v \rangle_{bb} = 7.4 \left(^{+2.7}_{-2.3} \right) \times 10^{-26} \text{ cm}^3 \text{ s}^{-1}. \tag{3.9}$$

For the τ-lepton channel, we found

$$m_\chi = 9.0 \left(^{+0.27}_{-0.23} \text{ stat.} \right) (\pm 2. \text{ sys.}) \text{ GeV}, \tag{3.10}$$

$$\langle \sigma v \rangle_\tau = 2.2 \left(^{+1.2}_{-0.7} \right) \times 10^{-26} \text{ cm}^3 \text{ s}^{-1}. \tag{3.11}$$

The systematic errors are defined largely by the background diffuse emission model uncertainties, which impacts the determined dark matter particle mass much more greatly than its cross section. This parameter space is significantly constrained by dwarf galaxy annihilation searches, as shown in Fig. 3.3. The parameter space agrees largely with other analyses. The region found by Calore et al. [5] is a bit lower due to two factors: they adopt a high value for $\rho_\odot = 0.4$ GeV cm^{-3}, as well as a more peaked central profile for their fit at $\gamma = 1.2$, which are along the lines of Milky Way profile changes that would be required to escape dwarf constraints, as discussed above. The interaction rates for the GCE signal at these particle masses are also in tension with collider searches for many couplings [122].

There are models for generation of the GCE from secondary emission of annihilation products that could alleviate these constraints. One such model produces the GCE as an IC emission from leptonic final states, matching the profile and spectrum but with a significantly reduced annihilation cross section [123, 124, 125]. The IC-induced GCE is generated in the high value of the GC's interstellar radiation field, while the radiation density in dwarf galaxies is much lower, potentially allowing evasion of this tension.

Perhaps the largest systematic or modeling uncertainty is the extrapolation of the Milky Way profile from the local density determination, $\rho_\odot$, at $R_\odot$ to where the GCE is bright at $\lesssim 500$ pc, which determines the profile of the extrapolation γ. For example, a strong adiabatic contraction of the Milky Way's dark matter halo due to baryonic infall could greatly enhance the inner Galaxy dark matter density. To illustrate an extreme, yet potentially physically viable, high-concentration/contraction case that would be necessary to eliminate the constraints from dwarf galaxies, we chose a high local density and small Milky Way halo scale radius, corresponding to a high concentration or contracted profile radius, reducing the particle dark matter annihilation rate necessary for the GCE considerably and avoiding the dwarf galaxy bounds. These choices for a pure NFW halo are inconsistent with dark matter only simulations, but consistent with halo profiles that have a contracted scale radius

50

close to $R_\odot$ [121, 96]. However, recent dynamical plus microlensing data are inconsistent with a strongly contracted halo [126]. In addition, contraction is not seen in high-mass halo systems where it is expected to more greatly contribute [127]. Any contraction of the halo must also preserve both the local density constraints from Zhang et al. [115] and the inner halo profile required by the gamma-ray data, $\gamma = 1.0 - 1.2$. In summary, our high-concentration/contraction case appears disfavored by dynamical constraints, but evades dwarf galaxy limits and is a plausible model for exploration of particle dark matter properties.

A recent study aiming to determine the local stellar density from star counts, McKee et al. [6], has found lower stellar densities than previous analyses, such as Zhang et al. [115], Bovy & Tremaine [117], and Bovy & Rix [118], that determine the modeled stellar density profile simultaneosly as the dark matter profile, using the position and velocity data of stars above the plane. If these lower stellar densities are borne out to be accurate, with the total density remaining invariant, then the dark matter density would be commensurately determined to be higher. The error analysis on the local dark matter density in McKee et al. [6] uses the variation in total mass density determinations to set the value of $\sigma(\rho_\odot)$ and is not the result of a robust error analysis. Therefore, both the error and central value on the density from star counts are approximate. In Fig. 3.3 we also show alternate GCE contours, in gray, from the higher value of the approximate local dark matter density inferred by McKee et al. [6]. McKee et al. state that high-above the Galactic plane estimates of the local density like that in Refs [115, 117, 118] are "the cleanest determination of the local density of dark matter," which agrees with our choice of the current most robust determination of the local dark matter density to be that from Zhang et al. [115]. However, if there is a systematic uncertainty that shifts local stellar densities lower, our framework allows for a reassessment of the GCE and dwarf agreement or tension regarding a dark matter interpretation.

In summary, we performed a Bayesian analysis of the GCE emission that more accurately accounts for uncertainties in the Milky Way halo parameters and approximates diffuse back-

ground emission model uncertainties. The presence of the GCE is relatively robust to variations in the background models, though the best fit values of the dark matter particle mass depends significantly on these background models. Our analysis is certainly not an exhaustive search of all Milky Way halo and diffuse model uncertainties, but demonstrates the fact that uncertainties in the halo parameters increase the uncertainty in dark matter particle parameters. Significantly, however, we find that canonical Milky Way halo properties leave the GCE parameter space significantly in conflict with dwarf galaxy uncertainties. In order to make a quantitative statement as to the level of exclusion of the GCE by the combined dwarf analyses, a joint likelihood analysis of the combined dwarf and GCE constraints would need to be performed.

Though the triple consistency of the dark matter interpretation of the GCE with morphology, signal strength, and spectra remains intriguing, the strong tension with dwarf galaxy annihilation searches illustrated here, and extreme change to the Milky Way halo properties would be needed to alleviate these constraints, may indicate that astrophysical interpretations of the GCE are more plausible, or more novel dark matter annihilation mechanisms are required to produce the GCE while avoiding constraints from dwarf galaxies. Further multiwavelength analysis is required to model background sources of gamma-rays, which constrains the associated systematics and allows insight into the true nature of the gamma-ray excess in the Galactic Center.

Chapter 4

What the Milky Way's Dwarfs tell us about the Galactic Center extended excess

4.1 Introduction

The Large Area Telescope aboard the *Fermi Gamma-Ray Space Telescope*, *Fermi*-LAT, has observed a bright excess of gamma rays towards the Galactic Center whose presence is robust to systematic uncertainties in the standard background templates [97, 128, 98, 99, 101, 129, 3, 102, 110, 4, 5, 96, 124, 130, 131]. This excess has generated a great deal of interest since dark matter (DM) annihilation models can explain three compelling coincidences in the signal. First, the excess' spatial morphology matches the predictions of a generalized Navarro-Frenk-White (NFW) profile, which is a generic prediction of cold DM models [132, 112]. Second, the total flux of the signal is well fit by the annihilation cross-section required by a thermal production scenario to generate the observed cosmological relic abundance.

Third, the spectrum roughly matches the expectations of a tens of GeV weakly interacting massive particle (WIMP) annihilating to standard model particles. Should the GCE turn out to be explained by such an annihilating WIMP DM particle, it could be the first non-gravitational evidence of DM and the first strong clue of the particle nature of DM.

The prompt annihilation of WIMPs is not the only class of DM models that can explain the GCE, however. For example, a class of self-interacting DM (SIDM) models can explain the GCE via up-scattering of starlight that would not be seen in dwarf galaxies [123, 133, 134, 135, 136]. Specifically, this class of SIDM particles could annihilate into electrons (as well as the other standard model leptons) and these electrons could up-scatter the Galactic Center's interstellar radiation field (ISRF) via the inverse Compton (IC) process.

There are also reasonable astrophysical interpretations of the GCE. Most notably is that the GCE can arise from a population of unresolved millisecond pulsars (MSP) [104, 101, 137, 138, 102, 139, 140, 141, 142, 143, 144, 145]. Specifically, observations of MSPs in globular clusters show they have a spectrum consistent with the spectrum of the GCE. Further, low mass X-ray binaries (likely progenitors of MSPs) in M31 have been observed to follow a power law radial spatial distribution, similar to the expectations of an NFW halo [101, 141]. Other astrophysical explanations might include more dynamic events such as cosmic-ray injection into the Galactic Center (GC) [146, 147, 148, 149]. Furthermore, the presence of the *Fermi* Bubbles tell us that such dynamic events have occurred in the past, so whatever mechanism produced the *Fermi* Bubbles, could also have produced the GCE [150, 151, 152].

There have arisen a number of independent avenues that each has the potential to challenge a DM interpretation of the GCE. One such avenue is to look for a gamma-ray excess from other DM halos. Such halos include those of galaxy clusters, the limits from which have recently been extended to be in slight tension with the GCE [153, 154], and the Milky Way's satellite dwarf galaxies, the most recent *Fermi* limits appearing in Ref. [155]. Unfortunately, *Fermi*-LAT observations of both of these sources, and particularly the dwarfs, have not seen

a significant complementary gamma-ray excess.[1] In particular, this difference between the GCE and the dwarfs has the potential to rule out certain classes of DM interpretations of the GCE. Specifically, any minimal model based around a two-body annihilation process (any process where the flux is proportional to the square of the DM density) would exhibit this same tension.

One paper which explores any tension between the GCE and a lack of a gamma ray signal from the dwarfs is Calore et al (2014)[124]. They do not find any indication of tension, though they use relaxed constraints on Galactic parameters relative to our analysis, particularly the local DM density, which would explain the difference in our results. Also, they use different statistical techniques to test the consistency of this DM annihilation scenario.

Other avenues to test whether the GCE is better explained by annihilating DM or astrophysics is to more precisely check whether the morphology of the excess truly follows a smooth NFW profile [158, 159]. Tension in the morphology of the GCE has arisen from the detection of an 'X-shape' residual in the *Fermi* data which correlates infrared emission as seen by the WISE telescope [160]. Should this 'X-shape' template account for the entirety of the GCE, it would challenge any DM interpretation since DM annihilation would not produce such a shape. Measurements of the GCE being consistent with wavelets [105] or non-Poissonian fluctuations have also been reported [161, 106, 162, 163], which would indicate an point source rather than DM origin, though systematic uncertainties in such analyses remain [164]. Specifically, small scale gas clouds are left out of the model used by `GALPROP`, software used to generate the gamma-ray templates associated with cosmic rays propagating through the Milky Way, which could confuse any detection of point sources near the GC [164]. Though each of these lines of evidence against a DM interpretation of the GCE have their own systematic uncertainties, many of these systematics are independent of each other. Arguably, these different lines of evidence add up to strongly indicate that the

---

[1]Note, however, there has been a low-significance detection of a gamma-ray excess from Reticulum II and Triangulum II, see e.g. [108, 156], although see also [157].

GCE is astrophysical in origin.

Our focus in the present paper is to consider one aspect of this general line of reasoning: the consistency between the GCE and the dwarfs, and to do so with a more detailed treatment of the systematics coming from both sides. The discussion is structured as follows. In section 4.2 we discuss the background models we investigate to understand some of the dominant sources of systematic uncertainties in the problem. In section 4.3, we discuss DM annihilation models of the GCE. In section 4.4, we discuss alternative models to promptly annihilating DM, including astrophysical interpretations and SIDM models. We conclude in section 4.5.

4.2   Background Models and Data

There remains significant uncertainty regarding the various processes that contribute to the gamma-ray signal coming from the GC. Any interpretation of the GCE will necessarily be affected by these uncertainties. To capture these effects, we investigate four different cases of the astrophysical background contributions to the GCE.

For all of our cases (denoted cases A, B, C, and D), we use data collected by *Fermi*-LAT. For cases A, B, and C, that data corresponds to observations over a 103 month period from August 2008 to March 2017. We use all `SOURCE`-class photons from the Pass 8 instrument response functions. We apply a maximum zenith angle cut of 90° to avoid contamination. In cases A, B, and C, we focus our analysis on the innermost $7° \times 7°$ region of interest (ROI) about the Galactic Center. We then bin these photons into spatial bins of size $0.05° \times 0.05°$ for each energy bin. The photon events range from 200 MeV to 50 GeV and are binned in 16 logarithmically spaced energy bins.

For Case D we instead choose a dataset similar to that considered in the Inner Galaxy analyses of [4, 162]. Here we use the best quartile, as graded by the *Fermi* point spread
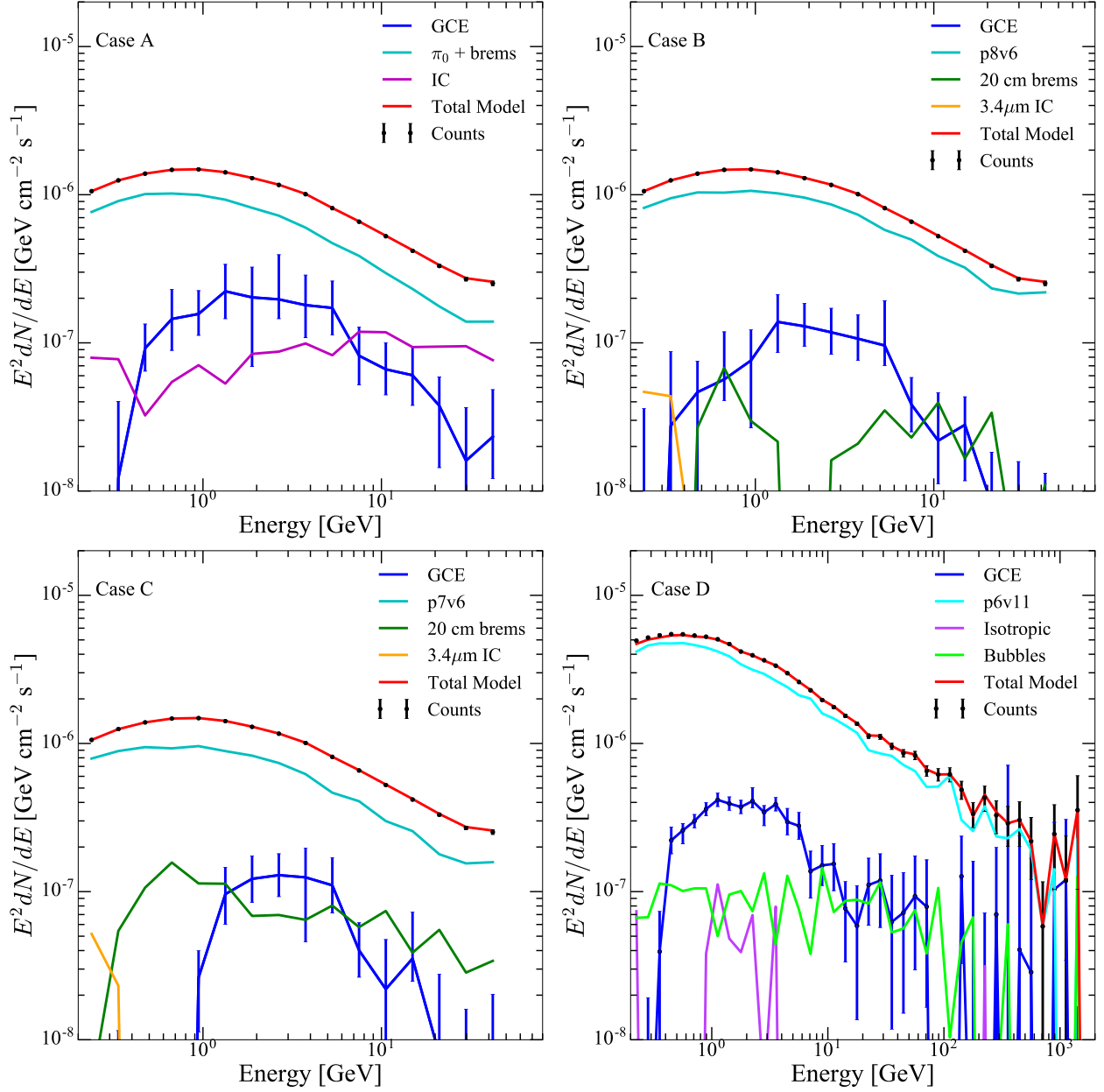
Figure 4.1: Here we plot the energy flux spectrum (intensity) $E^2 dN/dE$ for the various templates included in the likelihood fits for our A, B, C, and D background cases. These show the total emission from the ROI, $7° \times 7°$ for cases A-C and $30° \times 30°$ for case D. The error bars on the counts is the Poisson error. The various 3FGL sources were also varied in the fits but are not included for the sake of simplicity.

function, of `ULTRACLEANVETO`-class Pass 8 photons, gathered between August 4, 2008 and June 3, 2016 with recommended quality cuts. This case can be contrasted with the above in that it generally corresponds to less data, but with less cosmic-ray contamination and

improved angular reconstruction per event. To mimic an earlier Inner Galaxy analyses, we use a larger ROI of $30° \times 30°$, masking latitudes less than $1°$. No masks were applied to the data in cases A-C. We also mask the top 300 brightest and most variables sources in the 3FGL catalog [165] at 95% containment. The photons are binned into 40 equally spaced logarithmic bins between 200 MeV and 2 TeV, and spatially using an `nside`=128 `HEALPix` grid [166].

With this processed data, we perform a maximum likelihood analysis to determine the best fit background model and GCE model. For each component of our model, we generate a template which encodes the spatial distribution of the photons for that component. The quantity that we are trying to determine is then the linear combination of these spatial templates that best fit the observed number of counts. The templates fall into three groups: point sources, extended emission, and diffuse emission. The point sources we use are taken from *Fermi*'s 3FGL point source catalog [165] and they are typically well characterized or independent of the GCE result. The extended emission components include a GCE template, as well as background components coming from cosmic rays interacting with gas in the interstellar medium (ISM) or photons in the ISRF. Specifically, these would include any IC radiation from high energy electron cosmic rays up-scattering the ISRF, neutral pion (π_0) decay generated from hadronic cosmic rays interacting with the ISM, and bremsstrahlung radiation arising from high energy electrons interacting with the ISM. The spatial distribution of these components are more *a priori* uncertain than point sources and are partially degenerate with the GCE, especially in the lowest energy bins, where the point-spread function is the largest. Therefore, it is these uncertainties and degeneracies that make a careful and broad investigation of the diffuse backgrounds crucial to analyzing the GCE and are the main difference between our different cases.

Since the uncertainty in the spectral shape of the GCE signal is dominated by systematic uncertainties in the background templates, rather than Poisson fluctuations of the total

counts, it is necessary to explore multiple possible background models. To this end, we use four different sets of templates for these extended background models:

- **Case A:** We use the templates for the π_0, bremsstrahlung, and IC emission for 'model F' from Horiuchi et al. (2016) [164], which in turn used diffusion model parameters from Calore et al. (2014) [5] to generate their background models. Their 'model F' corresponds to the diffuse background model that was found to best fit the data in their ROI. Unlike the *Fermi* collaboration Pass 8 and Pass 7 diffuse backgrounds, the IC component of the diffuse background is fit independently of the π_0+bremsstrahlung components. We used the templates for 'model F' from these papers. In this work, we denote this 'case A.'

- **Case B**: For this case, we use the Pass 8 Galactic interstellar emission model from the *Fermi* tools, which models the distribution of gamma rays coming from π_0 decay, bremsstrahlung, and IC. All three components are combined in a single diffuse template with fixed relative normalizations in each energy bin. Furthermore, we used a template which traces the 20 cm radio emission first discovered by Yusef-Zadeh et al. (2013) [95]. We also include a template for an additional IC component that was derived from 3.4μm maps from the WISE telescope, discovered by Abazajian et al. (2014) [96].

- **Case C:** This case uses the same templates for the bremsstrahlung and IC components but uses `p7v6` model for Pass 7.

- **Case D:** This case uses the `p6v11` template and floats an isotropic template as well as a template for the *Fermi* bubbles.

For all these cases, we allow the flux associated with each template in a given bin to be independent of the flux in other bins, rather than assume a specific component has a specific spectral shape. This allows us to be agnostic about the shape of the spectrum for each of

these sources, but potentially comes at the cost of over-fitting the data. The results of these maximum likelihood fits for cases A-D are shown in Fig. 4.1.

To calculate posteriors for the dwarfs, we use the flux likelihood limits from Albert et al. (2016) [155]. Specifically, we use the flux likelihood manifolds for the nineteen kinetically confirmed dwarf galaxies that have measured J-factors. The J-factor for Reticulum II is calculated in Simon et al. (2015) [167] and the rest are calculated in Geringer-Sameth e t al. (2014) [168]. To calculate these flux likelihood limits, Albert et al. use six years of LAT data with 24 equally-spaced logarithmic bins between 500 MeV and 500 GeV. They binned the photons in a $10° \times 10°$ region about the target dwarf galaxies with a pixel size of $0.1°$ in order to model any overlap from the points spread function of the point sources in the 3FGL catalog, from the Galactic diffuse emission, and from the isotropic model. Each target dwarf galaxy was modeled as a point-like source and used a maximum likelihood analysis with these templates to generate the flux likelihood limits.

4.3 Annihilating Dark Matter Models

4.3.1 Flux Spectra

The differential flux in some ROI for the class of two-body DM annihilation is given by the following:

$$\frac{d\Phi}{dE} = \frac{1}{4\pi} \frac{J}{m_\chi^2} \frac{\langle \sigma v \rangle}{2} \frac{dN}{dE} . \tag{4.1}$$

Here, J is the J-factor, the integral of the density-squared over the ROI and through the line of sight. m_χ is the mass of the DM particle and $\langle \sigma v \rangle$ is the thermally averaged cross section of the annihilation. $\frac{dN}{dE}$ is the per-annihilation spectrum, which we calculated using

`PPPC4DMID` [114]. For our dark matter models, we use flat priors on the DM mass and scale invariant priors on the cross section. The prior on the J-factor is discussed in the next section.

4.3.2   J-factors

The J-factor is the square of the DM density integrated through the line of sight and integrated over the ROI.

$$J = \int_{\mathrm{ROI}} d\Omega \int dz \, \rho^2(r(z, \Omega)) \,. \tag{4.2}$$

As in Abazajian & Keeley 2015 [169], we determine the prior on the J-factor for the GC by parameterizing the Milky Way's DM halo as a generalized NFW profile with a local DM density ($\rho_\odot$), a scale radius (R_s), and an inner profile slope (γ)

$$\rho(r) = \frac{\rho_\odot}{\left(\frac{r}{R_\odot}\right)^\gamma \left(\frac{1+r/R_s}{1+R_\odot/R_s}\right)^{3-\gamma}} \,. \tag{4.3}$$

Each of these parameters has a probability distribution, so in principle, we could say the prior on the J-factor is the product of the probability distributions of each of these parameters and then perform the change of variables to write this probability distribution as a function of the J-factor. This is analytically cumbersome, so we use numerical Monte Carlo methods to calculate this distribution. Specifically, we draw values for the local density, scale radius, and inner slope to compute a set of J-factors and then use kernel density estimation to define the prior for the GCE J-factor.

For the local density, we use the value determined by Zhang et al. (2012) [115]: $\rho_\odot = 0.28 \pm 0.08 \ \mathrm{GeV} \ \mathrm{cm}^{-3}$. This robust determination of the local DM density is derived from modeling

the spatial and velocity distributions for a sample of 9000 K-Dwarf stars from the Sloan Digital Sky Survey (SDSS). The velocity distribution of these stars directly measures the local gravitational potential and, when combined with stellar density constraints, provides a measure of the local DM density.

Some analyses of Galactic dynamics, including local stellar measures [6] as well as rotational dynamic measures [170, 171] give a wider range of local density constraints. These would alter the GCE-dwarf tension measures, and were studied in Abazajian & Keeley (2015) [169]. We chose to use the Zhang et al. (2012)[115] value since it represents a determination of the local density that is independent of any model-based projection that would occur using rotation curve measures.

The prior on the scale radius is calculated from the concentration, which is the ratio of the virial radius to the scale radius. The uncertainty in the concentration is calculated from simulations of galaxy formation. Sanchez-Conde and Prada (2013) [120] parameterized the uncertainty in the concentration of a DM halo as a function of that halo's mass. Thus we can write the prior on the scale radius as:

$$\log \mathcal{L} = -\frac{(\log_{10}(R_{\mathrm{vir}}/R_s) - \log_{10} c(M_{\mathrm{vir}}))^2}{2 \times 0.14^2} \, . \tag{4.4}$$

The prior on the inner slope we use for the Monte Carlo calculation of the J-factor is taken to be the posterior determined by the spatial information contained in the GCE data. We constrain the inner slope by running the likelihood analysis with the same background models but with different NFW spatial templates that have different values for the inner slope. The likelihood analysis calculates the ΔLog-likelihood value for each of these different cases, which allows us to fit a χ^2 distribution to these ΔLog-likelihood values. This determines the best fit value of γ and its error. Unsurprisingly, this derived prior on the inner slope depends on the background model used. For case A we calculate, $\gamma = 1.14 \pm 0.04$; for case

B, $\gamma = 1.24 \pm 0.04$; for case C, $\gamma = 1.10 \pm 0.04$; and for case D, we calculate $\gamma = 1.2 \pm 0.06$. The results of this Monte Carlo calculation of the priors on the J-factor for the different background cases is shown in Fig. 4.2.

We include the uncertainties in dwarf galaxy J-factors by employing the priors on these J-factors from Albert et al. (2016) [155]. These are all reported as log-normal distributions. These J-factors come with some caveats, however. Specifically, assumptions about how spherically symmetric the dwarf galaxy is, which in turn can influence the inferred cuspiness of the density profile, can lead to systematic uncertainties greater than the statistical uncertainties [172, 173, 174].
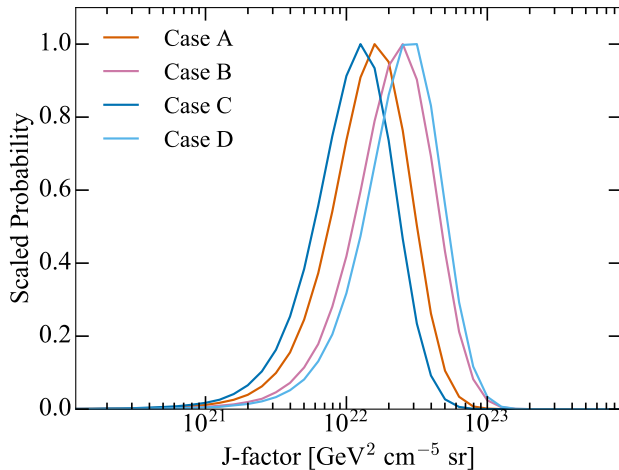
Figure 4.2: The prior on the J-factor integrated over the ROI derived through a Monte Carlo convolution of the priors on the local density, scale radius, and inner slope. Since each of the different background cases have different best fit values for γ, and since case D corresponds to a larger ROI, the derived uncertainties on the J-factors are different.

4.3.3 Evidence Ratios

To quantify the tension between the GCE and the dwarfs, we calculate a Bayesian evidence ratio. This evidence ratio can be used in answering the question: by what factor do the odds of some model being true change with the inclusion of a new data set. It is the product of the Bayesian evidences of two data sets, D_1 and D_2, when considered separately divided by

the evidence of the two data sets when considered jointly [175]:

$$\text{ER} = \frac{p(D_1)p(D_2)}{p(D_1, D_2)}$$

$$= \frac{\int d\theta_1 p(D_1|\theta_1)p(\theta_1) \int d\theta_2 p(D_2|\theta_2)p(\theta_2)}{\int p(D_1, D_2|\theta)p(\theta)} . \quad (4.5)$$

This can be interpreted as a Bayes factor where the two models being compared are the same except for the fact that the model corresponding to the numerator has an additional, independent copy of the parameter space and the two parameter spaces describe the two data sets separately.

This statistic can indicate three different outcomes for the model. First, if the data set D_2 contains no information, then this evidence ratio is unity. If D_2 is entirely consistent with D_1 then the evidence ratio should be less than unity. This is expected since increasing the complexity of a model should come at a cost of subjective belief. If D_2 is in tension with D_1 then this evidence ratio will be greater than unity. How strongly this evidence ratio prefers consistency or tension can be interpreted by any standard Bayes factor scale. In this work, we choose to interpret our evidence ratios by the Jeffreys' scale.

Using this setup, we then calculate evidence ratios between the combined dwarf galaxies and the GC. The results are stated in Table 4.1.

One particularly useful feature of evidence ratios in this context is that, compared to Bayes factors, they are relatively insensitive to systematic uncertainties in the background models. These systematic uncertainties can alter the total flux of the signal, but they more drastically change in which energy bin this flux is distributed. This is seen most clearly in the lowest energy bins, where the inclusion of diffuse templates from 20 cm maps of bremsstrahlung emission and 3.4 μm maps of IC emission, for cases B and C, remove all the photons from the NFW template for these bins. Such changes to the lowest energy bins changes the overall

curvature of the GCE spectrum, which, in turn, significantly changes the best fit mass but not the best fit cross section [169]. When the best fit mass of the GCE changes, the amount of overlap between the GCE posterior with the combined dwarfs posterior (and hence the evidence ratio) changes relatively little. This lack of change in overlap comes from the fact that the contours of the dwarf posterior are almost parallel to contours of constant cross section, since the lack of a dwarf signal contains no significant amount of information about the spectrum. It is because the evidence ratio is most sensitive to the cross section and not particularly sensitive to the dark matter mass that the evidence ratios are more robust to systematic uncertainties in the background templates. This is born out in Table 4.1 where the DM evidence ratios for the different cases vary by only two orders of magnitude. On the other hand, because the Bayes factors are sensitive to both the normalization and the shape of the spectrum it can vary by 30 orders of magnitude, as seen in Table 4.2.

Beyond systematic uncertainties due to the inclusion of additional templates for bremsstrahlung and inverse Compton processes, uncertainties in the diffuse model for the `GALPROP` generated π_0, IC, and bremsstrahlung templates, can alter the total flux of the GCE signal and will affect the best fit cross section for the GCE and hence affect the tension with the dwarfs. This is seen by the fact the evidence ratio for our different cases significantly change. This change is caused by the fact that the differences in these diffuse emission templates, for cases B and D, shift the overall flux of the GCE signal to smaller values, relative to case A. In these background model cases, the presence of the GCE is less significant and reduces the significance of the tension with the dwarfs.

The information encoded by the evidence ratio can be qualitatively seen in Fig. 4.3, which plots the posterior of our $b\bar{b}$ and $\tau^+\tau^-$ DM annihilation models for each of our different GCE background cases and for the dwarf data. The amount of overlap in the GCE posteriors and the dwarf posterior indicates the amount of tension between the data sets.

For our DM annihilation models, we calculate evidence ratios between 15 and 2200 for the

$b\bar{b}$ channel and between 27 and 4300 for the $\tau^+\tau^-$ channel. Using the Jeffreys Scale, this indicates a strong (>10) to decisive (>100) tension in two-body DM interpretations of the GCE and dwarf data.

Importantly, this strong to decisive tension exists in models beyond just the specific DM particle annihilating to $b\bar{b}$ or $\tau^+\tau^-$. Any model of prompt two-body decay, described by a J-factor, would exhibit this same tension. Hence, models that contain only novel versions of spectrum dN/dE, or branching ratios, will not alleviate this strong tension.
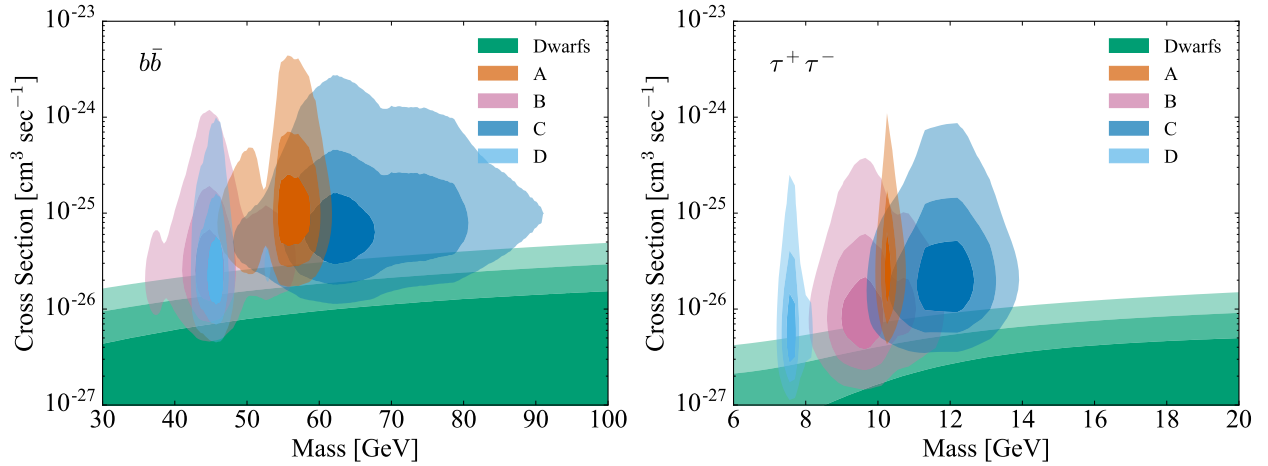
Figure 4.3: Here we show the 1, 2, and 3σ contours of the posteriors for the annihilation cross section and DM mass. Our calculated limits on the dwarf signal is in green, case A is in orange, case B is in blue, and case C is in pink. The results for $b\bar{b}$ on the left and $\tau^+\tau^-$ on the right. The amount of overlap qualitatively demonstrates the information contained in the evidence ratio and shows how consistent two-body DM annihilation models are at explaining both the GCE and the lack of a dwarf signal.

4.3.4   Caveats

The GCE-dwarf tension we quantified in the previous section certainly depends on the prior information adopted for the J-factors of the GC region and the dwarf galaxies. Naturally, if there was a significant change in the inferred DM content of either the GC region or dwarf galaxies, then the nature of tension would correspondingly change. However, our choices for the J-factor of the GC region and dwarf galaxies are those determined by the most robust

Table 4.1: Evidence ratios for our five models using the diffuse templates for our various background cases.

Model	Case A	Case B	Case C	Case D
DM: $b\bar{b}$	3600	21	220	15
DM: $\tau^+\tau^-$	2300	25	230	29
Log-Parabola	0.69	0.58	0.71	0.54
Exponential Cutoff	0.73	0.59	0.78	0.54
SIDM	1.1	1.2	1.2	1.1

analyses available.

The parameter that the J-factor is most sensitive to is the local density of DM. As stated in a previous section, we use a value of 0.28±0.08 GeV/cm³ taken from Zhang et al. (2012) [115]. Other groups including Pato et al. (2015) [176] and McKee et al. (2015) [6] tend to find higher values for the local density. To fully resolve the tension between the GCE and the dwarfs, the GCE J-factor needs to increase between 1 and 1.5 orders of magnitude, which translates into a local density of 3 to 6 times greater. As we show, none of these determinations of the local density relieve the GCE-dwarf evidence ratio to be unity.

Another parameter with a systematic uncertainty is the scale radius of the DM profile. Small deviations around our fiducial value would not change the J-factor by a great deal since the inner profile is unchanged due to the scale radius being beyond the local radius. However, should the scale radius become smaller than the local radius, the inner density profile would increase as r^{-3} between the local radius and the scale radius, resulting in a larger J-factor. A profile with such a small scale radius could only occur in halos with a concentration parameter far outside of what CDM simulations predict for halos with the mass of the Milky Way.

The inner slope γ is more robust to systematic uncertainties, in that it is determined directly from the spatial information of the gamma-ray data. In particular, to fully resolve the GCE-

dwarf tension, a value of around $\gamma = 1.7$ would be required. However, all of the diffuse models that we tested preferred values for the inner slope were found to be significantly below that, between and $\gamma = 1.1$ and 1.3. Despite systematic uncertainties in the parameterization of the Milky Way's DM profile, no single alteration can fully relieve the tension between the GCE and dwarf data.

4.4   Models

We have shown that there is tension with the standard WIMP scenario between the derived cross sections from the GC and the dwarfs, with some important caveats. This tension can potentially point to alternate models being better explanations for the GCE, including astrophysical interpretations to more complicated DM models. To quantitatively answer this question, we calculate a Bayes factor:

$$K_{12} = \frac{p(M_1|D)p(M_2)}{p(M_2|D)P(M_1)} = \frac{p(D|M_1)}{p(D|M_2)}. \qquad (4.6)$$

We consider the following models: two astrophysical interpretations, one with a log-parabola spectrum and another with an exponential cutoff spectrum, and a SIDM model where the GCE gamma rays are generated by DM decaying to high-energy electrons up-scattering starlight. The Bayes factors for our models are given in Table II.

4.4.1   Astrophysical Interpretations

Should the GCE have an astrophysical interpretation, the gamma-ray spectrum can be parameterized as a log-parabola or a power law with an exponential cutoff. We investigate both parameterization as explanations of the GCE.

The spectrum for our log-parabola model is given by:

$$\frac{dN}{dE} = N_0 \left(\frac{E}{E_s} \right)^{-\alpha - \beta \log(E/E_s)} , \tag{4.7}$$

where N_0 is an arbitrary normalization, E_s is a scale energy, α is the slope of the power-law part of the spectrum, and β parameterizes the turnover of the spectrum.

The spectrum for our power law with an exponential cutoff model is given by:

$$\frac{dN}{dE} = N_0 \left(\frac{E}{E_s} \right)^{\gamma} e^{-E/E_c} , \tag{4.8}$$

where N_0 is the normalization of the spectrum, E_s is a scale energy, γ is the slope of the power-law part of the spectrum, and E_c parameterizes how fast the spectrum cuts off.

Our astrophysical models do not have a specific physical interpretation so it is not straightforward to investigate to what extent the GCE and the lack of signal from the dwarf galaxies are compatible given these models. Presumably, if the GCE and any potential dwarf signal were to be explained by the same category of astrophysical object, then they should have the same spectral parameters. Therefore, it makes sense for our model to have only one set of spectral parameters that describes both the GCE and the dwarfs. The normalizations of the spectrum, however, would not necessarily be the same. One option is to allow the normalization of the spectrum of the GCE and the spectrum of each of the dwarfs to be independent. Following this parameterization, we calculate an evidence ratio between the GCE and the dwarfs of about 1, which would indicate the two data sets contain no new information relative to each other. This is expected, since if we put in the fact that the signals are independent, we should get out that they have no mutual information. Instead of saying these normalizations are entirely independent of each other, we use a zeroth order ansatz to parameterize the normalization as the product of the stellar mass of the system and the gamma-ray rate per stellar mass. The stellar mass would, of course, be independent between

regions, but the gamma-ray rate per stellar mass should be the same between regions. To this end, we find N_0 in the above equations such that the integral of dN/dE over our energy range (200 MeV to 50 GeV) is one. This allows us to attach physical interpretations to our normalization for $d\Phi/dE$.

Specifically, it makes sense, should the initial mass function of some galaxy be independent of the stellar mass of that galaxy, that the gamma-ray production rate scales linearly with the stellar mass of the galaxy. Hence, the gamma-ray rate per stellar mass should be consistent across all regions.

Ultimately, this leads to the following parameterization of the differential number flux:

$$\frac{d\Phi}{dE} = \frac{\dot{N}}{4\pi R^2} \frac{M_*}{M_0} \frac{dN}{dE}, \tag{4.9}$$

where M_* is the stellar mass of the object, R is the distance to the object, and $\dot{N}/M_0$ is the gamma-ray rate per stellar mass, which should be the same between different objects.

For both spectra of astrophysical models, we marginalized over the spectral parameters with flat priors, and marginalized over the over the gamma-ray rate per stellar mass with a scale invariant prior. We use the stellar mass of the dwarfs, the distance to them, as well as the uncertainties in those parameters from McConnachie (2012) [177]. Interestingly, both of our astrophysical models pick out values for the gamma-ray rate per stellar mass around $10^{31\pm1}$ s^{-1} $M_\odot^{-1}$, which is consistent with known millisecond pulsars. In the end, the evidence ratios for each of our two spectral choices for astrophysical models, for all of our background cases, are less than unity. Importantly, this less than unity evidence ratio indicates that the combined dwarf and GCE data have a weak indication of a mutual astrophysical excess described by a single set of parameters.

The Bayes factors we compute also point towards a preference for these astrophysical models.

As seen in Table 4.2, the log-parabola spectrum is preferred over any DM model in each of the cases, and the exponential cutoff spectrum is preferred in three out of four of the cases. The preference in the Bayes factor can be thought of as coming from two distinct sources. One is the GCE data on their own prefer that model and the other is that the model can better explain the differences in the flux from the GC and the dwarfs. Astrophysical interpretations, with evidence ratios less than unity, can do better on the latter count, but interestingly, depending on the data case, can also do better on the former count. In all cases, the log-parabola spectrum can explain the GCE data better than dark matter models, but in cases B and C, the exponential cutoff can do so also. This preference in some cases for the log-parabola spectrum is predominantly coming from the lowest energy bins. The maximum likelihood fit prefers giving no appreciable amount of photons to the lowest energy bins, a fact that is difficult for DM models to explain, but is more easily accommodated by the log-parabola spectra. This preference of the lowest energy bins for the log-parabola spectra can be seen in Figure 4.4, where we plot the best fit models, along with the data. It is worth noting that these lowest energy bins have the largest systematics associated with them due to the large size of the size of the point spread function at those energies [5]. Unlike the evidence ratios, the Bayes factors are particularly sensitive to these systematics, particularly because no model is a strikingly good fit, just less bad than the others. Indeed, when ignoring the first few data points for each data case, the Bayes factors tend to show less extreme results, giving more consistent fits to the GCE. With these truncated data sets, the values of the Bayes factors come from the models' abilities to explain the difference in flux coming from the GC and the dwarfs.

On an additional note, the preference for $b\bar{b}$ can also be seen in Fig. 4.4. Since the $\tau^+\tau^-$ model requires a light (compared to the $b\bar{b}$ model) dark matter mass to explain the peak of the GCE spectra at around 1-2 GeV, and since these annihilating dark matter models cutoff in energy at around their mass, the $\tau^+\tau^-$ model fail to account for the GCE spectra that gradually fall off with large energies, such as in cases A, B, and D.

4.4.2 A Representative SIDM Model

In certain classes of SIDM models for the GCE, the gamma-ray excess is generated by the DM particles annihilating to electron-positron pairs through a light mediator [123]. The electrons then up scatter the starlight in the Galactic Center via an IC process. This would naturally explain the difference in the observed gamma-ray flux between the GC and the dwarfs since the stellar density of the dwarfs, and therefore the interstellar light, is many orders of magnitude smaller than the stellar mass of the GC.

Should the GCE be explained DM annihilating to electrons that interact with the ambient starlight, the process should be governed by the following IC equation:

$$\frac{dn_\gamma}{dEdt} = \sigma_T c n_e n_{\text{ISRF}} \frac{dN_\gamma}{dE} \,, \tag{4.10}$$

where n_γ is the number density of gamma rays, σ_T is the Thomson cross section, n_e is the number density of electrons produced by annihilating DM, n_{ISRF} is the number density of low energy photons in the interstellar radiation field, and $\frac{dN_\gamma}{dE}$ is the probability distribution function of producing a gamma ray of energy E via this IC process. Naturally, this probability distribution function depends on the probability distribution functions of the energies of the electrons produced via DM annihilation and the energy distribution of the starlight:

$$\frac{dN_\gamma}{dE} = \int dE_e dE_{\text{ISRF}} p(E_\gamma | E_e, E_{\text{ISRF}}) p(E_e) p(E_{\text{ISRF}}) \,. \tag{4.11}$$

In principle, other energy-loss mechanisms, such as synchrotron emission, can alter the energy distribution of electrons in this IC process. We checked this model against the spectrum `PPPC4DMID` calculates and found the shape of the spectra were largely consistent.

Since the electrons are produced via a two-body interaction, the number density of electrons should scale as the square of the number density of DM particles: $n_e \propto n_\chi^2$. To convert the

time derivative of the differential number density of photons to some number flux, we need to evaluate the following integral:

$$\frac{d\Phi_\gamma}{dE} = \int dV' \frac{1}{4\pi(\vec{R} - \vec{R}')^2} \frac{dn_\gamma}{dEdt}(\vec{R}') \,. \tag{4.12}$$

Choosing the origin of the coordinate system to be at $R = 0$ leads to the standard expression for the J-factor, should the process be entirely a two-body process and the time derivative of n_γ scale solely as the square of the DM particles. Putting this all together, we get:

$$\frac{d\Phi_\gamma}{dE} \propto \int d\Omega dz \frac{1}{4\pi} n_{\mathrm{ISRF}} n_\chi^2 \frac{dN}{dE} \,. \tag{4.13}$$

Instead of using this equation as written, we make the following assumptions and simplifications. First, n_{ISRF} is approximately constant where the density of DM is largest, so we can pull the factor of n_{ISRF} outside the integral. Second, it should be true that the number density of photons from stars scales with the stellar mass of those stars we replace n_{ISRF} with the stellar mass of the gamma-ray source, M_*:

$$\frac{d\Phi_\gamma}{dE} \propto \frac{J}{m_\chi^2} \frac{M_*}{M_{*,\mathrm{GC}}} \,. \tag{4.14}$$

Taking this spectrum leads to a model that has far greater consistency between the GCE and dwarfs; the evidence ratios for this model are all around unity for each of the data cases. This highlights the possibility to alleviate the tension when going beyond simple two-body final state scenarios.

The best fit DM mass for this representative SIDM model is 15 ± 1 GeV for cases A and D, 15 ± 3 GeV for case B, and 21 ± 2 GeV for case C.

Table 4.2: Bayes factors for the considered models, relative to the $b\bar{b}$ model, for each of the different background cases. Values larger than one indicate the data prefer that model over $b\bar{b}$.

Model	Case A	Case B	Case C	Case D
DM: $\tau^+\tau^-$	4×10^{-24}	1×10^{-5}	7×10^4	1×10^{-22}
Log-Parabola	3×10^{12}	4×10^5	2×10^{12}	5×10^9
Exponential Cutoff	2×10^1	2×10^4	4×10^{10}	0.1
SIDM	5×10^{-20}	8×10^{-19}	6×10^{-2}	0.1

To construct a more realistic and self-consistent SIDM model, we would need to account for two effects. The first is Sommerfeld enhancement in the dwarfs. This Sommerfeld enhancement causes an increase in the effective annihilation cross section due to the smaller velocity dispersion in the dwarfs, relative to the GC [123]. This would tend to push down the limits on the DM annihilation cross section coming from the dwarfs. However, unless this enhancement factor were many orders of magnitude above unity, the evidence ratio would still be around unity. The second effect would have the opposite impact on the dwarfs' cross section limits. Since SIDM models generically predict cored density profiles for the dwarfs [178], the inferred central density of the dwarves would be smaller than implied by assuming an NFW profile, as is currently done. This, in turn, would decrease the J-factors of the dwarfs and push up the limits on the DM annihilation cross section.

4.5 Conclusions

We have analyzed the GCE in a wide variety of background models by performing a template based likelihood analysis of the GC using four different models for the diffuse background templates. To answer the question of whether an annihilating DM interpretation can be consistent with the lack of dwarf signals, we calculated evidence ratios for each model of the
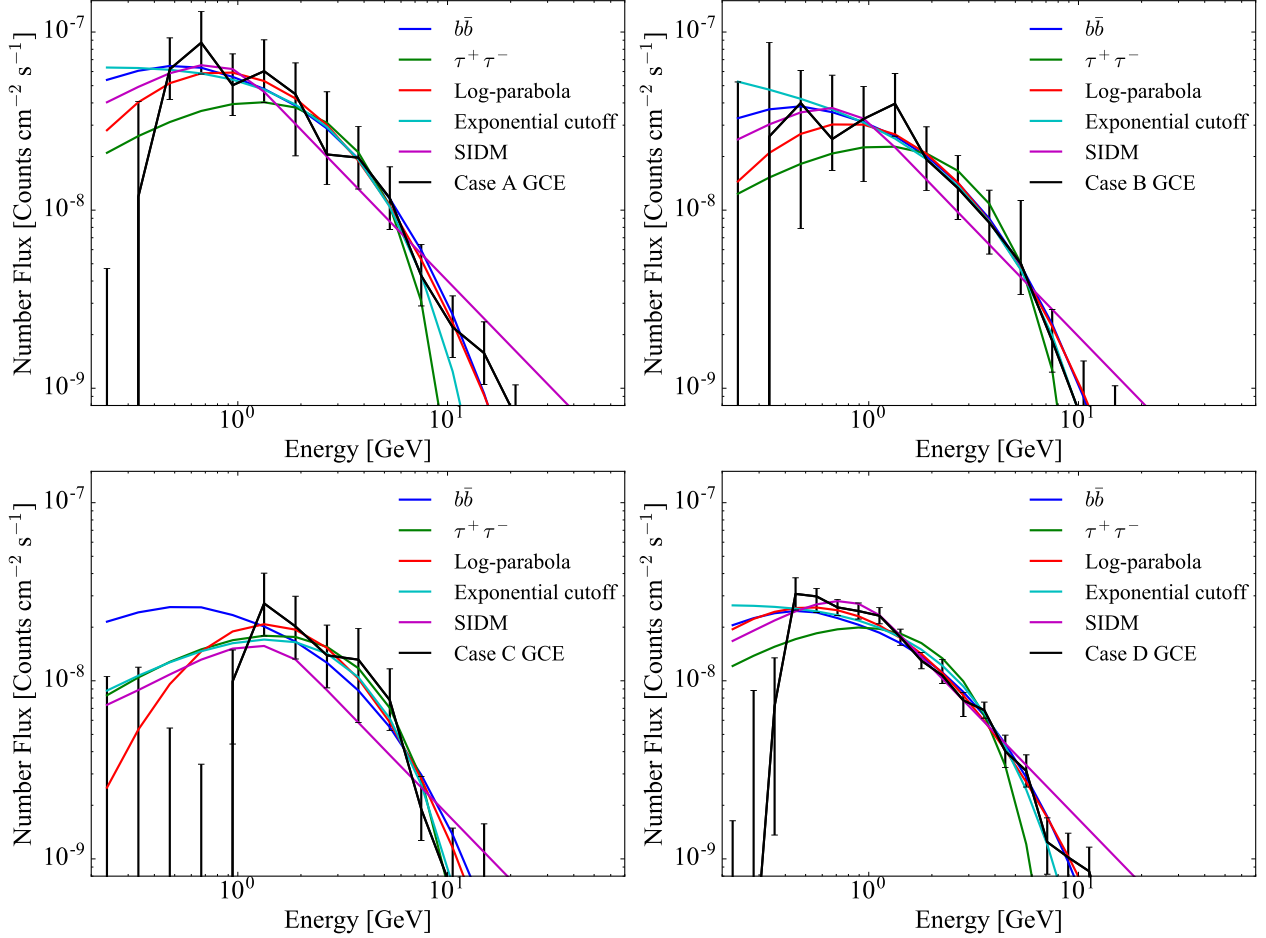
Figure 4.4: Here we plot the number flux for the GCE template along with the best fit spectra for the different models considered. The error bars correspond to the 1-σ region of each bin's number flux likelihood profiles.

GCE and for each case of diffuse background models. These evidence ratios are sensitive to the choice of background model but they all display strong to decisive tension between the GCE and the dwarfs for annihilating DM models. Specifically, cases A and C show decisive tension, with evidence ratios greater than 100 for both annihilation channels, and cases B and D show strong tension with evidence ratios greater than 10 for both channels. This difference can, at least in part, be attributed to the fact the likelihood fit for these cases seem to prefer both giving less flux to the DM GCE component, and also prefer an NFW template with a higher value for the inner slope γ. Since the tension is seen to various degrees using a variety of models for the the diffuse emission, it is robust to say that prompt

two-body annihilating DM interpretations of the GCE are in strong doubt.

Astrophysical and SIDM interpretations of the GCE fare better with evidence ratios around unity. Ultimately, allowing the gamma ray signal to scale with the stellar mass, as for astrophysical models, or with the product of the J-factor and stellar mass, as with SIDM models, relieves any tension between the GCE signal and lack of a dwarf signal.

We also calculated Bayes factors for our different DM GCE interpretation models. This Bayes factor can be thought of as coming from two different sources: the ability of the model to explain the GCE and the ability of the model to explain the difference in GCE and dwarf fluxes. These Bayes factors decisively prefer the log-parabola spectrum model over the DM annihilation models in all of our background cases, and prefer the exponential cutoff model in three of the four background cases. This preference for either astrophysical spectrum model predominantly comes from the lowest energy bins where the likelihood analysis prefers to attribute no amount of flux to an NFW template. However, these are also the energy bins that have the largest systematic uncertainties associated with them. Standard two-body DM annihilation models cannot explain these low energy gamma-ray data, while more general log-parabola and exponential cutoff models are able to do so. With the long integration time now available from the *Fermi*-LAT observations of the GCE, the data allows us to make very precise determinations of the GCE's spectral parameters, given a particular background model. However, the accuracy of these background models are still uncertain. In other words, the systematic uncertainties in the background model cases dominate over the Poisson statistical uncertainties. In fact, there exist two sets of tests. One is whether DM or astrophysical spectral models' can explain the joint GCE and dwarf data. The second is the intrinsic ability of the GCE spectral choices to explain the GC observations. Importantly, the biggest change in the models' Bayes factors comes from the spectral models' different ability to properly fit the GCE. In almost all cases, log-parabola spectra is decisively better in their evidence ratios at fitting the GCE data (cf. Table 4.2).

Therefore, given the GCE data alone, the log-parabola astrophysical interpretation of the GCE is favored.

Furthermore, the combined GCE-dwarf data strongly to decisively disfavor single channel DM annihilation interpretations of the GCE. Secondary-emission from DM models like that from SIDM could alleviate the inconsistent emission between the GCE and dwarf galaxies. Further detailed analysis of the diffuse emission towards the GC will help determine the true nature of the GCE and its relation to any emission from the dwarf galaxies.

Chapter 5

Tying Dark Matter to Baryons with Self-interactions

5.1 Introduction

The CDM paradigm has been extremely successful in explaining the large-scale structure of the Universe. However, there is no established CDM-based solution to explain the central dark matter densities in galaxies. Observed dwarf galaxies and low surface brightness galaxies prefer 0.5-5 kpc cores of constant dark matter density [179, 180, 181, 182], in contrast to the $1/r$ (where r is distance from the center of the galaxy) cusps seen in CDM-only simulations [112]. There is also evidence for deviations from the $1/r$ behavior within the brightest (central) cluster galaxies [183]. Additionally, the most massive subhalos predicted by CDM-only simulations are too dense to host observed dwarf satellite galaxies in the Milky Way [37]. It is possible that in-situ supernova feedback [184], environmental effects [185, 186] or an early episode of star formation [187, 188, 189] may play a role in resolving these issues. Here, we focus on the possibility that the above small-scale issues may be resolved

by significant self-interactions among dark matter particles [190].

Recent N-body simulations have shown that strong dark matter self-interactions can lower the central dark matter density and lead to core formation matching observations on small-scales [7, 191, 192, 193]. On larger scales (beyond the core), SIDM behaves as the same as CDM. In particular, ΛSIDM retains all the cosmological successes of ΛCDM. However, the particle physics of SIDM models is strikingly different. For example, the existence of a ~1-100 MeV light force carrier is necessary to generate the required self-scattering cross section [194]. When the mediator couples to standard model particles, it may generate signals that can be probed by direct and indirect dark matter detection experiments [195]. To quantify indirect detection signals, it is crucial to understand the SIDM halo profile in the Milky Way and its satellites.

Elastic interactions between dark matter particles allow for energy exchange and hence transport of heat. By the time each particle has had a few interactions over the lifetime of the galaxy, an isothermal core forms [7]. Our main point in this *Letter* is that the presence of baryons can have a dramatic influence on the predictions for the SIDM halo profile when baryons dominate the potential well. In particular, we show that the core properties are tied to the stellar gravitational potential leading to a smaller and denser core. A straightforward conclusion from this finding is that the constraints on the self-interaction cross section will be loosened.

To contrast our results with the expectations from SIDM-only simulations, we consider the example of the Milky Way. In the case of the dark matter dominated halos, the temperature (velocity dispersion) increases with radius in the inner region, $r \lesssim r_s$ (where the density profile is less steep than $1/r^2$). Hence interactions that lead to energy exchange between dark matter particles tend to make the inner region hotter, producing a constant-density isothermal core. The core radius is set by the transfer cross section over dark matter particle mass σ_T/m_χ. The larger this quantity, the bigger the core with the caveat that the isothermal
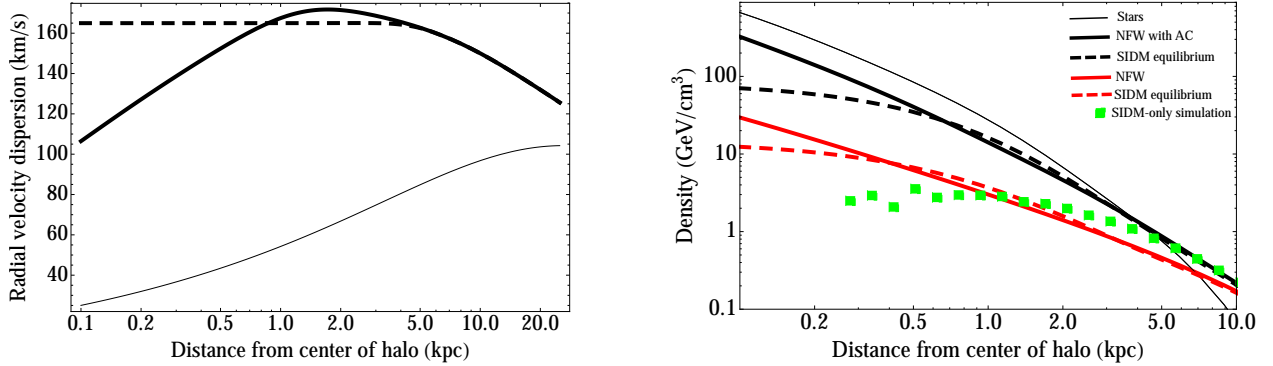
Figure 5.1: *Left:* the radial velocity dispersion for dark matter (thin solid: contracted NFW; solid: contracted NFW in stellar potential; dashed: SIDM in stellar potential). *Right:* the dashed curves show SIDM equilibrium solutions assuming the density profile matches on to a NFW profile (solid red) and an adiabatically contracted NFW profile (solid black) at 10 kpc, and an isotropic velocity dispersion tensor. The green squares show the SIDM density profile for a $10^{12} M_\odot$ halo from dark-matter-only simulations [7]. Note that the points below 1 kpc are not fully resolved in this simulation.

region is at $r \lesssim r_s$, which is true for interesting values of σ_T/m_χ [7]. The prediction for the Milky Way core radius (where the density is half the central density) is $\mathcal{O}(10\text{kpc})$ for $\sigma_T/m_\chi \sim 1$ cm^2/g [7, 193].

If baryons dominate the potential well, as in the case of the Milky Way, they will dictate the temperature (velocity dispersion) profile of dark matter. As we will see, the dark matter temperature peaks around 1 kpc in the Milky-Way case leading to a small (sub-kpc) core size. Seen from the point of view of an equilibrium solution, the dark matter spatial density profile has to track the gravitational potential of the baryons. *Hence, we arrive at the surprising conclusion that in the limit of significant self-interactions, the radius of the dark matter core is intimately tied to the gravitational potential of the baryons.* The corresponding central density will naturally be larger than the predictions of the SIDM-only simulations.

5.2 Solutions to the Jeans Equation

Once an isothermal core forms, further scattering will not lead to significant changes in the density profile of the core. We neglect the possibility of core collapse here, which hasn't been seen in recent simulations with $\sigma_T/m_\chi \lesssim 1$ cm^2/g [7, 192]. We further assume that the stellar profile is set on time scales shorter than the time required for dark matter to attain equilibrium through self-scattering. In this limit, we can neglect the scattering term and rewrite the Jeans equation [196] (using Poisson's equation) with constant velocity dispersion σ_0 and dark matter density $\rho(\vec{r}) = \rho_0 \exp(h(\vec{r}))$ as:

$$\nabla_x^2 h(\vec{x}) + (4\pi G_N r_0^2/\sigma_0^2)\left(\rho_B(\vec{x}) + \rho_0 \exp(h(\vec{x}))\right) = 0\,, \tag{5.1}$$

where ρ_0 is a density scale that we take to be the central dark matter density, $\vec{x} = \vec{r}/r_0$ with r_0 as a length scale, and ρ_B is the baryonic density profile. To illustrate our main point, let's first consider the case in which baryons completely dominate the potential well. In this limit, we can neglect the $\exp(h)$ term and the solution to Equation 5.1 is simply:

$$\rho(\vec{x}) = \rho_0 \exp\left((\Phi_B(0) - \Phi_B(\vec{x}))/\sigma_0^2\right)\,, \tag{5.2}$$

where $\Phi_B(\vec{x})$ is the baryonic potential generated by the density distribution $\rho_B(\vec{x})$. We define the core radius as the position where the density falls by a factor of 2 or $h(\vec{r}_c) = \ln 2$. Thus, $\vec{r}_c$ is given by the solution to $\left(\Phi_B(0) - \Phi_B(\vec{r}_c)\right) = \sigma_0^2 \ln 2$. It is clear that the core radius in this limit depends on the baryonic potential rather than the self-interactions as long as the interaction strength is large enough. The density profiles in generic solutions to Equation 5.2 are also not spherically symmetric. Both these features are in marked contrast

to the predictions of SIDM when dark matter dominates [7, 193].

To estimate the SIDM core size in the Milky Way, we specialize to the spherically symmetric solution. We include contributions from the stellar bulge, the thin disk and the thick disk of the Milky Way from the best-fit model advocated in Ref. [197] and then calculate the mass enclosed within spherical shells to get a "spherical Milky Way" model. This profile turns out to be fit by a Hernquist density profile $\rho_B(r) = \rho_{B0} r_0^4 / [r(r + r_0)^3]$, where we have set r_0 to be the Hernquist scale radius. The assumed Hernquist profile for the baryon distribution in the Milky Way can be specified by either $\Phi_B(0) = -2\pi G \rho_{B0} r_0^2 = -GM_B/r_0$ or the circular velocity $V_B^2(r_0) = -\Phi_B(0)/4$, where G is Newton's constant and M_B is total mass in baryons. With $\sqrt{-\Phi_B(0)} = 365$ km/s and $r_0 = 2.7$ kpc, we found a good fit. Thus, the core radius is $r_c \approx \sigma_0^2 \ln 2 / (2\pi G \rho_{B0} r_0) = r_0 \sigma_0^2 \ln 2 / 4 V_B^2(r_0) = r_0^2 \sigma_0^2 \ln 2 / GM_B$. Numerically, we have

$$r_c \approx 0.3 \text{ kpc} \left(\frac{r_0}{2.7 \text{ kpc}} \right) \left(\frac{\sigma_0}{150 \text{ km/s}} \right)^2 \left(\frac{183 \text{ km/s}}{V_B(r_0)} \right)^2, \tag{5.3}$$

where we take a typical value $\sigma_0 \sim 150$ km/s (as we will discuss later). Thus, the expected core size in the Milky Way halo is much smaller than ~ 10 kpc as predicted by the SIDM-only simulations.

In this spherically symmetric limit, the analytical solution for $h(x)$ can be generalized to include the case when the dark matter component is important. Assuming the above Hernquist profile for baryons, we obtain

$$\frac{1}{y^2} \frac{d}{dy} \left[y^2 \frac{d}{dy} h(y) \right] + \frac{2a_1}{y} + \frac{a_0}{(1-y)^4} \exp \left[h(y) \right] = 0, \tag{5.4}$$

where we define $a_0 \equiv 4\pi G \rho_0 r_0^2 / \sigma_0^2$ and $a_1 \equiv -\Phi_B(0)/\sigma_0^2$, and h should be interpreted as a function of a new variable $y \equiv r/(r + r_0) = x/(1 + x)$. The boundary conditions to solve

this equation are $h(0) = 0$ and $h'(0) = -a_1$, where the second term enforces a core in the center. This may be derived by noting that as $y \to 0$, the solution to $h(y)$ has to be given by $(y^2 h'(y))' + 2a_1 y = 0$.

Within the core region, the density profile varies slowly. This suggests that the equation can be solved through a series of approximations. The first is obtained by setting the third term in Equation 5.4 equal to a_0 (i.e., setting $y = 0$), and we get $h \approx -a_1 y - a_0 y^2/6$. The core radius derived from this approximate solution is given by,

$$ r_c \approx r_0 \frac{\sqrt{1 + (2/3)\ln(2)a_0/a_1^2} - 1}{1 + a_0/(3a_1) - \sqrt{1 + (2/3)\ln(2)a_0/a_1^2}} . \tag{5.5} $$

This approximation is good to about 10% for the interesting ranges of a_0 and a_1. We note that if the stellar density profile differs from Hernquist and $\rho_B(r) \propto 1/r^\alpha$ for small r, then $h_0(y) = -2a_1 y^{2-\alpha}/(2 - \alpha)(3 - \alpha) - a_0 y^2/6$. In particular, there is no cored profile when $\rho_B(r)$ diverges towards the center as $1/r^2$.

Several limits of these equations are particularly illuminating. In the limit that a_0 is $\mathcal{O}(1)$ and a_1 is large, we obtain $r_c \approx r_0 \ln(2)/[a_1 - \ln(2)]$, *i.e.*, the core is set just by the baryonic potential, which agrees with the result we derived before. In the opposite limit when the baryons are not dynamically important, we have a self-gravitating isothermal sphere and $r_c \approx r_0 \sqrt{6\ln(2)/a_0}$ or $r_c^2 \approx 3\ln(2)\sigma_0^2/(2\pi G\rho_0)$. Thus, as the baryonic contribution gets larger, the core radius becomes smaller.

To further illuminate this result, we need estimates for the central density ρ_0 to fix a_0. In Ref. [7], a model was presented for the SIDM density profile of field halos based on the radius r_1 where the average dark matter particle has had one interaction and the density profile in the absence of self-interactions, *i.e.*, the CDM halo density profile. For the Milky Way halo, the predicted CDM halo density profile has the NFW form and we assume this profile with the appropriate concentration for a virial mass of 10^{12} M$_\odot$ [198]. The NFW profiles have

a density at the solar position $r = 8.5$ kpc of 0.2 GeV/cm^3, which is in the range of the measured value [115]. If we use a velocity dispersion of 150 km/s (appropriate for the Milky Way) the average number of scatterings per particle per 10 Gyr within the solar radius is unity for $\sigma_T/m_\chi \sim 1$ barn/GeV $= 0.56$ cm^2/g. (Basically, 0.2 GeV/cm^3 $\times$ 150 km/s $\times$ 1 barn/GeV $\times$ 10 Gyr $\simeq 1$.) Hence we expect to see deviations due to self-interactions at radii smaller than $\sim$10 kpc for $\sigma_T/m_\chi \sim 1$ barn/GeV. This cross section is consistent with all observations and is in the range required to solve the small-scale anomalies [7, 191].

Values for ρ_0 about 10 times the local density would be expected in SIDM simulations that do not include baryons. If this were true even when including a stellar component, then we would have a_0 of order unity. Specifically,

$$a_0 \approx 1 \left(\frac{\rho_0}{2.2 \text{ GeV/cm}^3} \right) \left(\frac{r_0}{2.7 \text{ kpc}} \right)^2 \left(\frac{150 \text{ km/s}}{\sigma_0} \right)^2. \tag{5.6}$$

For the Milky Way, we will find values of $a_0 = \mathcal{O}(10)$ because the equilibrium solution including the stellar potential demands larger values of the central density ρ_0. In order to choose from the family of solutions parameterized by a_0 and a_1, we impose two conditions - that the mass within r_1 and the total energy within r_1 are the same as the halo would have had in the absence of self-interactions. These conditions are based on the model presented in Ref. [7].

The two resulting SIDM profiles (shown in Figure 5.1) show a spread of almost an order of magnitude in the the central (core) density and show that the SIDM profile depends on the details of the disk and bulge formation and associated feedback. However, the core radius is determined to be close to 0.3 kpc in both cases. We caution that this estimate depends sensitively on the assumed inner density profile of the baryons. For example, if the baryons are more centrally concentrated within 0.3 kpc, the core radius would be smaller.

For the adiabatically contracted NFW profile [199], the velocity dispersion profile is plotted in the right panel of Figure 5.1. This profile is a solution to the Jeans equation assuming that the velocity dispersion tensor is isotropic. The value of the central density ρ_0 is 80 GeV/cm^3 and the central radial dispersion σ_0 is 165 km/s, both of which lead to an enclosed mass and energy within $r_1 = 15$ kpc (for $\sigma_T/m_\chi = 1$ barn/GeV) equal to that of an adiabatically contracted NFW. We note that even with this high central density the mean free path is larger than the core radii.

In order to solve for the SIDM profile beyond the core region, we join the constant dispersion region smoothly to the dispersion profile in the absence of self-interactions as shown by the dashed curve in the right panel of Figure 5.1. The density profile (dashed curves in the left panel of Figure 5.1) is the solution to the isotropic Jeans equation assuming this velocity dispersion profile. We note that the solution in the core (for this more complete solution) is the same as Equation 5.1. As an aside, we find that a numerical approximation to the full range $r < r_1$ can be obtained by considering a solution of the form $h(y, p) = -a_1 y - p a_0 y^2/6$ and then fixing p so that the mass enclosed within r_1 is the same as in the case without self-interactions.

For the NFW profile without adiabatic contraction (for example, due to significant feedback from star formation) the dispersion profile is very similar (since it is controlled in the inner regions by baryons) but the density profile is very different. We again use the isotropic Jeans equation to find the SIDM solution. Note that the assumption of an isotropic velocity dispersion tensor plays a central role in both cases. Physically, this is reasonable because scatterings lead to energy exchange that should erase the anisotropy in the velocity dispersion (which is small even in the absence of self-interactions). For this second case without initial adibatic contraction, the solution that matches the mass and energy profile in the absence of scatterings at r_1 has $\sigma_0 = 165$ km/s and $\rho_0 = 14$ GeV/cm^3.

We emphasize that the velocity dispersion profile is crucial to the effect we are pointing
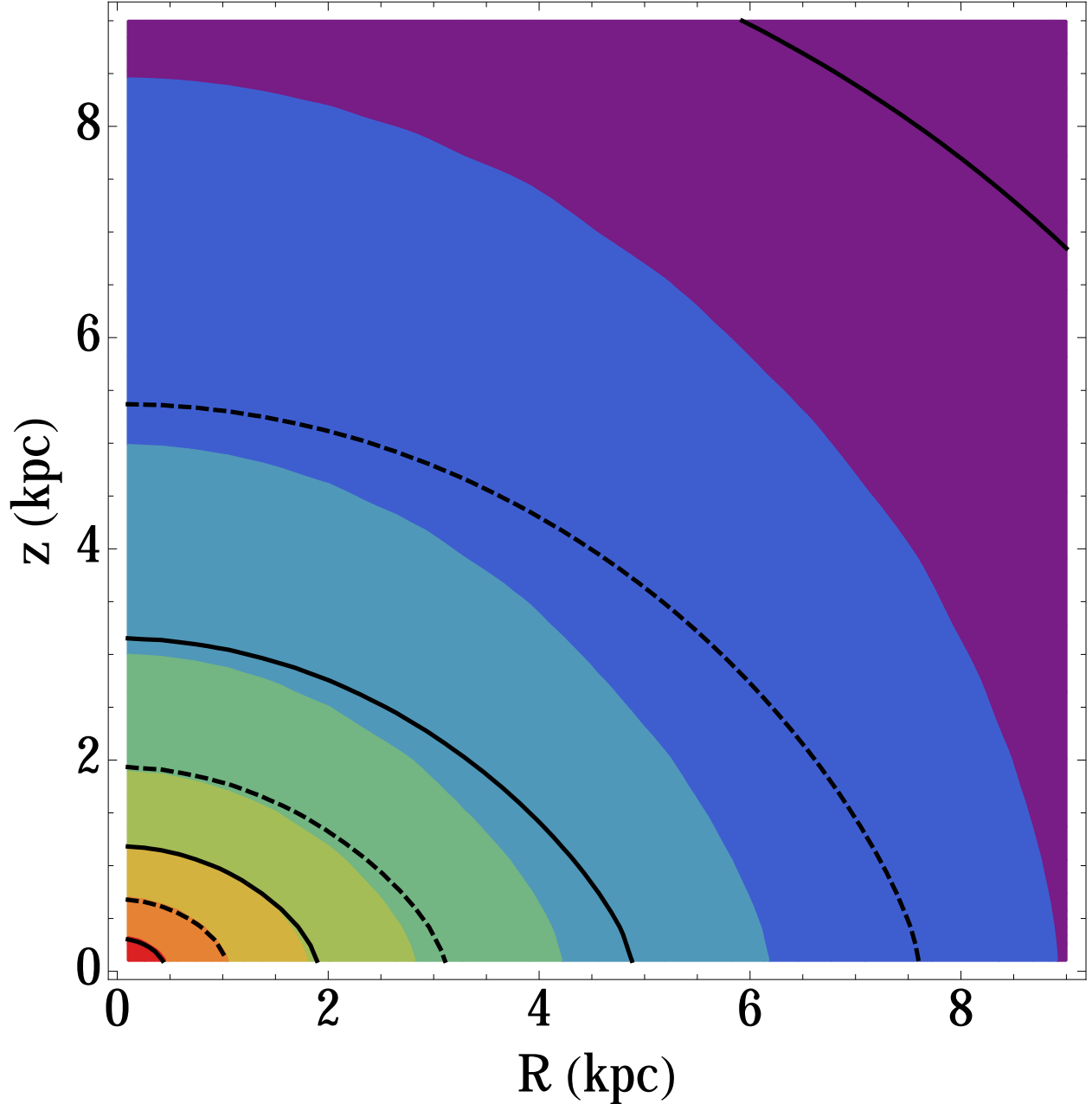
Figure 5.2: Constant density contours for dark matter in cylindrical coordinates (R, z) showing deviations from spherical symmetry outside the core (~ 0.3 kpc). The density at the outermost contour is 0.5 GeV/cm^3 and increases by factors 2. The color shaded contours are from the full numerical analysis, while the black curves are for the approximate solution given in Equation 5.2.

out. A core should form in the region that gets hotter (higher kinetic energy particles have larger apocenters on average) and hence the cross-over between the two dispersion profiles in Figure 5.1 provides an estimate of the core radius of the SIDM density profile.

5.3 Shapes of halos

The shape of the halo is not expected to be spherical and deviations from spherical symmetry will depend on the stellar potential well. This has been noted previously in the context of a non-spherical isothermal solution for a halo with an embedded thin disk [200]. To investigate this quantitatively, we incorporate a more realistic model for the baryon distribution in the Milky Way in our analysis. In the baryon-dominated central region, we expect the simple solution given in Equation 5.2 is valid. However, for the region away from the center, dark matter becomes important and a full numerical approach to the Jeans equation is necessary. Here, we numerically solve Equation 5.1 via a relaxation algorithm by rewriting Equation 5.1 in the following manner,

$$\nabla^2 h + a_0(\rho_B/\rho_0 + e^h) = \partial h/\partial t \,, \tag{5.7}$$

and demanding that $\partial h/\partial t \to 0$ for large t (where t plays the role of "time" for the relaxation method). We assume axisymmetry and then approximate the above equation using finite differencing on a logarithmically spaced grid. This finite difference equation is then relaxed to an equilibrium solution in two stages (coarse and then finer spatial grid), starting with a spherical NFW density profile and the boundary conditions imposed at 10 kpc (in R, z) in the form of the same profile.

The SIDM constant density contours in R, z for the resulting solution are plotted in Figure 5.2, which clearly shows deviations from spherical symmetry when baryons dominate the potential well. We see that the approximate solution in Equation 5.2 and the full numerical calculation give the same result in the inner region. Thus, it confirms the expectation that the SIDM distribution traces baryons when they dominate the potential well. The contours become spherical further away due to the boundary condition. Further investigations of how the shape depends on the iso-potential contours and changes away from the baryon-

dominated regions (without the assumption of spherically symmetric boundary conditions) may reveal a way to use this effect to test SIDM models in galaxies and clusters.

5.4   Discussion

A natural application of the effect described above is the SIDM density profile in the centers of clusters of galaxies. Assuming a Hernquist profile and the stellar mass and effective radii in Ref. [127], we find that the core sizes are $\mathcal{O}(10 \text{ kpc})$ using Equation 5.5. This is encouraging and deserves further work, especially since we predict a correlation between the SIDM core size and the effective stellar radius for which there seems to be some support [183].

Constraints on the self-interaction strength from the observed densities and shapes in clusters of galaxies [191] and the Bullet Cluster [201] should be reevaluated in light of the above results.

While this effect is relevant for most galaxies, it would be particularly interesting to apply the model presented here to spiral galaxies and dwarf galaxies, which show distinct correlations in their halo core properties [202].

5.5   Conclusions

We have shown that baryons and dark matter are tied together dynamically due to self-interactions in the dark matter. The presence of baryons changes the predicted SIDM density profile by decreasing the core radius and increasing the core density, with dramatic effects in baryon-dominated galaxies. For the Milky Way halo, SIDM follows the stellar distribution and forms a core around 0.3 kpc, in contrast to the ~ 10 kpc core predicted in SIDM-only simulations for $\sigma_T/m_\chi \sim 1$ barn/GeV. If SIDM is a thermal relic, the signal strength

from SIDM annihilation or decay in the Galactic Center is not suppressed as would have been deduced from SIDM-only simulations. Our results imply that in SIDM models the distributions of dark matter and baryons in galaxies are strongly correlated.

Bibliography

[1] T. Giannantonio et al. CMB lensing tomography with the DES Science Verification galaxies. *Mon. Not. Roy. Astron. Soc.*, 456(3):3213–3244, 2016.

[2] M. Ackermann et al. Searching for Dark Matter Annihilation from Milky Way Dwarf Spheroidal Galaxies with Six Years of Fermi-LAT Data. 2015.

[3] Chris Gordon and Oscar Macias. Dark Matter and Pulsar Model Constraints from Galactic Center Fermi-LAT Gamma Ray Observations. *Phys.Rev.*, D88:083521, 2013.

[4] Tansu Daylan, Douglas P. Finkbeiner, Dan Hooper, Tim Linden, Stephen K. N. Portillo, Nicholas L. Rodd, and Tracy R. Slatyer. The characterization of the gamma-ray signal from the central Milky Way: A case for annihilating dark matter. *Phys. Dark Univ.*, 12:1–23, 2016.

[5] Francesca Calore, Ilias Cholis, and Christoph Weniger. Background Model Systematics for the Fermi GeV Excess. *JCAP*, 1503:038, 2015.

[6] Christopher F. McKee, Antonio Parravano, and David J. Hollenbach. Stars, Gas, and Dark Matter in the Solar Neighborhood. *Astrophys. J.*, 814(1):13, 2015.

[7] Miguel Rocha, Annika H.G. Peter, James S. Bullock, Manoj Kaplinghat, Shea Garrison-Kimmel, et al. Cosmological Simulations with Self-Interacting Dark Matter I: Constant Density Cores and Substructure. *Mon.Not.Roy.Astron.Soc.*, 430:81–104, 2013.

[8] J. L. Feng et al. Planning the Future of U.S. Particle Physics (Snowmass 2013): Chapter 4: Cosmic Frontier. In *Proceedings, 2013 Community Summer Study on the Future of U.S. Particle Physics: Snowmass on the Mississippi (CSS2013): Minneapolis, MN, USA, July 29-August 6, 2013*, 2014.

[9] Adam G. Riess et al. Observational evidence from supernovae for an accelerating universe and a cosmological constant. *Astron. J.*, 116:1009–1038, 1998.

[10] M. Betoule et al. Improved cosmological constraints from a joint analysis of the SDSS-II and SNLS supernova samples. *Astron. Astrophys.*, 568:A22, 2014.

[11] P. J. E. Peebles and J. T. Yu. Primeval Adiabatic Perturbation in an Expanding Universe. *Astrophys. J.*, 162:815, December 1970.

[12] Shadab Alam et al. The clustering of galaxies in the completed SDSS-III Baryon Oscillation Spectroscopic Survey: cosmological analysis of the DR12 galaxy sample. *Mon. Not. Roy. Astron. Soc.*, 470(3):2617–2652, 2017.

[13] Andreu Font-Ribera et al. Quasar-Lyman α Forest Cross-Correlation from BOSS DR11 : Baryon Acoustic Oscillations. *JCAP*, 1405:027, 2014.

[14] Timothe Delubac et al. Baryon acoustic oscillations in the Ly forest of BOSS DR11 quasars. *Astron. Astrophys.*, 574:A59, 2015.

[15] Julian E. Bautista et al. Measurement of BAO correlations at $z = 2.3$ with SDSS DR12 lya-Forests. *Astron. Astrophys.*, 603:A12, 2017.

[16] Wayne Hu, Naoshi Sugiyama, and Joseph Silk. The Physics of microwave background anisotropies. *Nature*, 386:37–43, 1997.

[17] P. A. R. Ade et al. Planck 2013 results. XVI. Cosmological parameters. *Astron. Astrophys.*, 571:A16, 2014.

[18] P. A. R. Ade et al. Planck 2015 results. XIII. Cosmological parameters. *Astron. Astrophys.*, 594:A13, 2016.

[19] G. Hinshaw, D. Larson, E. Komatsu, D. N. Spergel, C. L. Bennett, J. Dunkley, M. R. Nolta, M. Halpern, R. S. Hill, N. Odegard, L. Page, K. M. Smith, J. L. Weiland, B. Gold, N. Jarosik, A. Kogut, M. Limon, S. S. Meyer, G. S. Tucker, E. Wollack, and E. L. Wright. Nine-year Wilkinson Microwave Anisotropy Probe (WMAP) Observations: Cosmological Parameter Results. *Astrophys. J. Supp.*, 208:19, October 2013.

[20] F. Zwicky. Die Rotverschiebung von extragalaktischen Nebeln. *Helv. Phys. Acta*, 6:110–127, 1933. [Gen. Rel. Grav.41,207(2009)].

[21] V. C. Rubin, W. K. Ford, Jr., and N. Thonnard. Extended rotation curves of high-luminosity spiral galaxies. IV - Systematic dynamical properties, SA through SC. *Astrophys. J. Lett.*, 225:L107–L111, November 1978.

[22] Douglas Clowe, Anthony Gonzalez, and Maxim Markevitch. Weak lensing mass reconstruction of the interacting cluster 1E0657-558: Direct evidence for the existence of dark matter. *Astrophys. J.*, 604:596–603, 2004.

[23] Maxim Markevitch, A. H. Gonzalez, D. Clowe, A. Vikhlinin, L. David, W. Forman, C. Jones, S. Murray, and W. Tucker. Direct constraints on the dark matter self-interaction cross-section from the merging galaxy cluster 1E0657-56. *Astrophys. J.*, 606:819–824, 2004.

[24] T. M. C. Abbott et al. Dark Energy Survey Year 1 Results: Cosmological Constraints from Galaxy Clustering and Weak Lensing. 2017.

[25] Edo van Uitert et al. KiDS+GAMA: Cosmology constraints from a joint analysis of cosmic shear, galaxy-galaxy lensing and angular clustering. 2017.

[26] Shahab Joudaki et al. KiDS-450: Testing extensions to the standard cosmological model. *Mon. Not. Roy. Astron. Soc.*, 471:1259, 2017.

[27] Shahab Joudaki et al. KiDS-450 + 2dFLenS: Cosmological parameter constraints from weak gravitational lensing tomography and overlapping redshift-space galaxy clustering. 2017.

[28] Shahab Joudaki et al. CFHTLenS revisited: assessing concordance with Planck including astrophysical systematics. *Mon. Not. Roy. Astron. Soc.*, 465(2):2033–2052, 2017.

[29] J. Elvin-Poole et al. Dark Energy Survey Year 1 Results: Galaxy clustering for combined probes. 2017.

[30] J. Prat et al. Dark Energy Survey Year 1 Results: Galaxy-Galaxy Lensing. 2017.

[31] David H. Weinberg, Romeel Dave, Neal Katz, and Juna A. Kollmeier. The Lyman - alpha forest as a cosmological tool. *AIP Conf. Proc.*, 666:157–169, 2003. [,21(2005)].

[32] David H. Weinberg et al. Cosmology with the lyman-alpha forest. 1998.

[33] M. A. Troxel et al. Dark Energy Survey Year 1 Results: Cosmological Constraints from Cosmic Shear. 2017.

[34] F. Köhlinger et al. KiDS-450: The tomographic weak lensing power spectrum and constraints on cosmological parameters. 2017.

[35] S. D. M. White and M. J. Rees. Core condensation in heavy halos - A two-stage theory for galaxy formation and clustering. *Mon. Not. Roy. Astron. Soc.*, 183:341–358, May 1978.

[36] W. H. Press and P. Schechter. Formation of Galaxies and Clusters of Galaxies by Self-Similar Gravitational Condensation. *Astrophys. J.*, 187:425–438, February 1974.

[37] Michael Boylan-Kolchin, James S. Bullock, and Manoj Kaplinghat. The Milky Way's bright satellites as an apparent failure of LCDM. *Mon.Not.Roy.Astron.Soc.*, 422:1203–1218, 2012.

[38] Ayuki Kamada, Manoj Kaplinghat, Andrew B. Pace, and Hai-Bo Yu. How the Self-Interacting Dark Matter Model Explains the Diverse Galactic Rotation Curves. *Phys. Rev. Lett.*, 119(11):111102, 2017.

[39] J. S. Bullock. Notes on the Missing Satellites Problem. *ArXiv e-prints*, September 2010.

[40] H. Hildebrandt et al. KiDS-450: Cosmological parameter constraints from tomographic weak gravitational lensing. *Mon. Not. Roy. Astron. Soc.*, 465:1454, 2017.

[41] Adam G. Riess et al. A 2.4% Determination of the Local Value of the Hubble Constant. *Astrophys. J.*, 826(1):56, 2016.

[42] P. A. R. Ade et al. Planck 2013 results. XX. Cosmology from SunyaevZeldovich cluster counts. *Astron. Astrophys.*, 571:A20, 2014.

[43] P. A. R. Ade et al. Planck 2015 results. XXIV. Cosmology from Sunyaev-Zeldovich cluster counts. *Astron. Astrophys.*, 594:A24, 2016.

[44] Catherine Heymans et al. CFHTLenS tomographic weak lensing cosmological parameter constraints: Mitigating the impact of intrinsic galaxy alignments. *Mon. Not. Roy. Astron. Soc.*, 432:2433, 2013.

[45] Nicolas Canac, Grigor Aslanyan, Kevork N. Abazajian, Richard Easther, and Layne C. Price. Testing for New Physics: Neutrinos and the Primordial Power Spectrum. *JCAP*, 1609(09):022, 2016.

[46] G. E. Addison, D. J. Watts, C. L. Bennett, M. Halpern, G. Hinshaw, and J. L. Weiland. Elucidating ΛCDM: Impact of Baryon Acoustic Oscillation Measurements on the Hubble Constant Discrepancy. *ArXiv e-prints*, July 2017.

[47] R. R. Caldwell, R. Dave, and P. J. Steinhardt. Cosmological Imprint of an Energy Component with General Equation of State. *Physical Review Letters*, 80:1582–1585, February 1998.

[48] Gong-Bo Zhao et al. Dynamical dark energy in light of the latest observations. *Nat. Astron.*, 1:627–632, 2017.

[49] G. R. Dvali, Gregory Gabadadze, and Massimo Porrati. 4-D gravity on a brane in 5-D Minkowski space. *Phys. Lett.*, B485:208–214, 2000.

[50] Sean M. Carroll, Vikram Duvvuri, Mark Trodden, and Michael S. Turner. Is cosmic speed - up due to new gravitational physics? *Phys. Rev.*, D70:043528, 2004.

[51] K. Freese, F. C. Adams, J. A. Frieman, and E. Mottola. Cosmology with decaying vacuum energy. *Nuclear Physics B*, 287:797–814, 1987.

[52] Luca Amendola. Coupled quintessence. *Phys. Rev.*, D62:043511, 2000.

[53] S. Weinberg. The cosmological constant problem. *Reviews of Modern Physics*, 61:1–23, January 1989.

[54] S. M. Carroll, W. H. Press, and E. L. Turner. The cosmological constant. *Annu. Rev. Astron. Astrophys.*, 30:499–542, 1992.

[55] Joshua Frieman, Michael Turner, and Dragan Huterer. Dark Energy and the Accelerating Universe. *Ann. Rev. Astron. Astrophys.*, 46:385–432, 2008.

[56] C. E. Rasmussen and C. K. I. Williams. *Gaussian Processes for Machine Learning.* the MIT Press, 2006.

[57] Zeljko Ivezic, Andrew J. Connolly, Jacob T. Vanderplas, and Alexander Gray. *Statistics, Data Mining, and Machine Learning in Astronomy*. Princeton University Press, 2014.

[58] A. Shafieloo, A. G. Kim, and E. V. Linder. Gaussian process cosmography. *Phys. Rev. D*, 85(12):123530, June 2012.

[59] T. Holsclaw, U. Alam, B. Sansó, H. Lee, K. Heitmann, S. Habib, and D. Higdon. Nonparametric reconstruction of the dark energy equation of state. *Phys. Rev. D*, 82(10):103502, November 2010.

[60] T. Holsclaw, U. Alam, B. Sansó, H. Lee, K. Heitmann, S. Habib, and D. Higdon. Nonparametric Dark Energy Reconstruction from Supernova Data. *Physical Review Letters*, 105(24):241302, December 2010.

[61] T. Holsclaw, U. Alam, B. Sansó, H. Lee, K. Heitmann, S. Habib, and D. Higdon. Nonparametric reconstruction of the dark energy equation of state from diverse data sets. *Phys. Rev. D*, 84(8):083501, October 2011.

[62] Jose Luis Bernal, Licia Verde, and Adam G. Riess. The trouble with H_0. *JCAP*, 1610(10):019, 2016.

[63] Florian Beutler et al. The clustering of galaxies in the completed SDSS-III Baryon Oscillation Spectroscopic Survey: Baryon Acoustic Oscillations in Fourier-space. *Submitted to: Mon. Not. Roy. Astron. Soc.*, 2016.

[64] Hlion du Mas des Bourboux et al. Baryon acoustic oscillations from the complete SDSS-III Lyα-quasar cross-correlation function at $z = 2.4$. 2017.

[65] Éric Aubourg et al. Cosmological implications of baryon acoustic oscillation measurements. *Phys. Rev.*, D92(12):123516, 2015.

[66] M. Betoule et al. Improved Photometric Calibration of the SNLS and the SDSS Supernova Surveys. *Astron. Astrophys.*, 552:A124, 2013.

[67] R. Adam et al. Planck 2015 results. I. Overview of products and scientific results. *Astron. Astrophys.*, 594:A1, 2016.

[68] S. Joudaki and M. Kaplinghat. Dark energy and neutrino masses from future measurements of the expansion history and growth of structure. *Phys. Rev. D*, 86(2):023526, July 2012.

[69] P. A. R. Ade et al. Planck 2015 results. XIII. Cosmological parameters. *Astron. Astrophys.*, 594:A13, 2016.

[70] Sean M. Carroll and Manoj Kaplinghat. Testing the Friedmann equation: The Expansion of the universe during big bang nucleosynthesis. *Phys. Rev.*, D65:063507, 2002.

[71] Zhen Hou, Ryan Keisler, Lloyd Knox, Marius Millea, and Christian Reichardt. How Massless Neutrinos Affect the Cosmic Microwave Background Damping Tail. *Phys. Rev.*, D87:083008, 2013.

[72] A. Lewis and S. Bridle. Cosmological parameters from CMB and other data: A Monte Carlo approach. *Phys. Rev. D*, 66(10):103511, November 2002.

[73] Marina Seikel and Chris Clarkson. Optimising Gaussian processes for reconstructing dark energy dynamics from supernovae. 2013.

[74] David Kirkby and Ryan Keeley. Cosmological expansion history inference using gaussian processes. 2017.

[75] M. Seikel, C. Clarkson, and M. Smith. GaPP: Gaussian Processes in Python. Astrophysics Source Code Library, March 2013.

[76] Marina Seikel, Chris Clarkson, and Mathew Smith. Reconstruction of dark energy and expansion dynamics using Gaussian processes. *JCAP*, 1206:036, 2012.

[77] M. Chevallier and D. Polarski. Accelerating Universes with Scaling Dark Matter. *International Journal of Modern Physics D*, 10:213–223, 2001.

[78] Eric V. Linder. Exploring the expansion history of the universe. *Phys. Rev. Lett.*, 90:091301, 2003.

[79] Antony Lewis, Anthony Challinor, and Anthony Lasenby. Efficient computation of cmb anisotropies in closed frw models. *Astrophys. J.*, 538:473–476, 2000.

[80] Amir Aghamousa et al. The DESI Experiment Part I: Science,Targeting, and Survey Design. 2016.

[81] DESI Final Design Report Part I: science, targeting, and survey design. `http://desi.lbl.gov/tdr/`. Accessed: 2017-07-01.

[82] C.-P. Ma and E. Bertschinger. Cosmological Perturbation Theory in the Synchronous and Conformal Newtonian Gauges. *Astrophys. J.*, 455:7, December 1995.

[83] Edmund Bertschinger. On the Growth of Perturbations as a Test of Dark Energy. *Astrophys. J.*, 648:797–806, 2006.

[84] Scott F. Daniel, Robert R. Caldwell, Asantha Cooray, and Alessandro Melchiorri. Large Scale Structure as a Probe of Gravitational Slip. *Phys. Rev.*, D77:103513, 2008.

[85] E. V. Linder. Cosmic growth history and expansion history. *Phys. Rev. D*, 72(4):043529, August 2005.

[86] Guillermo Ballesteros and Antonio Riotto. Parameterizing the Effect of Dark Energy Perturbations on the Growth of Structures. *Phys. Lett.*, B668:171–176, 2008.

[87] Sergei Bashinsky and Uros Seljak. Neutrino perturbations in CMB anisotropy and matter clustering. *Phys. Rev.*, D69:083002, 2004.

[88] Daniel Baumann, Daniel Green, Joel Meyers, and Benjamin Wallisch. Phases of New Physics in the CMB. *JCAP*, 1601:007, 2016.

[89] Wayne Hu and Martin J. White. The Damping tail of CMB anisotropies. *Astrophys. J.*, 479:568, 1997.

[90] K. T. Story et al. A Measurement of the Cosmic Microwave Background Damping Tail from the 2500-square-degree SPT-SZ survey. *Astrophys. J.*, 779:86, 2013.

[91] Thibaut Louis et al. The Atacama Cosmology Telescope: Two-Season ACTPol Spectra and Parameters. *JCAP*, 1706(06):031, 2017.

[92] Brent Follin, Lloyd Knox, Marius Millea, and Zhen Pan. First Detection of the Acoustic Oscillation Phase Shift Expected from the Cosmic Neutrino Background. *Phys. Rev. Lett.*, 115(9):091301, 2015.

[93] Jonathan L. Feng. Dark Matter Candidates from Particle Physics and Methods of Detection. *Ann.Rev.Astron.Astrophys.*, 48:495, 2010.

[94] M. Chernyakova, D. Malyshev, F.A. Aharonian, R.M. Crocker, and D.I. Jones. The high-energy, Arcminute-scale galactic center gamma-ray source. *Astrophys.J.*, 726:60, 2011.

[95] F. Yusef-Zadeh, J.W. Hewitt, M. Wardle, V. Tatischeff, D.A. Roberts, et al. Interacting Cosmic Rays with Molecular Clouds: A Bremsstrahlung Origin of Diffuse High Energy Emission from the Inner 2deg by 1deg of the Galactic Center. *Astrophys.J.*, 762:33, 2013.

[96] Kevork N. Abazajian, Nicolas Canac, Shunsaku Horiuchi, Manoj Kaplinghat, and Anna Kwa. Discovery of a New Galactic Center Excess Consistent with Upscattered Starlight. *JCAP*, 1507(07):013, 2015.

[97] Lisa Goodenough and Dan Hooper. Possible Evidence For Dark Matter Annihilation In The Inner Milky Way From The Fermi Gamma Ray Space Telescope. 2009.

[98] Dan Hooper and Lisa Goodenough. Dark Matter Annihilation in The Galactic Center As Seen by the Fermi Gamma Ray Space Telescope. *Phys.Lett.*, B697:412–428, 2011.

[99] Dan Hooper and Tim Linden. On The Origin Of The Gamma Rays From The Galactic Center. *Phys.Rev.*, D84:123005, 2011.

[100] Alexey Boyarsky, Denys Malyshev, and Oleg Ruchayskiy. A comment on the emission from the Galactic Center as seen by the Fermi telescope. *Phys.Lett.*, B705:165–169, 2011.

[101] Kevork N. Abazajian and Manoj Kaplinghat. Detection of a Gamma-Ray Source in the Galactic Center Consistent with Extended Emission from Dark Matter Annihilation and Concentrated Astrophysical Emission. *Phys.Rev.*, D86:083511, 2012.

[102] Oscar Macias and Chris Gordon. Contribution of cosmic rays interacting with molecular clouds to the Galactic Center gamma-ray excess. *Phys. Rev.*, D89(6):063515, 2014.

[103] Edward A. Baltz, James E. Taylor, and Lawrence L. Wai. Can Astrophysical Gamma Ray Sources Mimic Dark Matter Annihilation in Galactic Satellites? *Astrophys. J.*, 659:L125–L128, 2007.

[104] Kevork N. Abazajian. The Consistency of Fermi-LAT Observations of the Galactic Center with a Millisecond Pulsar Population in the Central Stellar Cluster. *JCAP*, 1103:010, 2011.

[105] Richard Bartels, Suraj Krishnamurthy, and Christoph Weniger. Strong support for the millisecond pulsar origin of the Galactic center GeV excess. *Phys. Rev. Lett.*, 116(5):051102, 2016.

[106] Samuel K. Lee, Mariangela Lisanti, Benjamin R. Safdi, Tracy R. Slatyer, and Wei Xue. Evidence for Unresolved γ-Ray Point Sources in the Inner Galaxy. *Phys. Rev. Lett.*, 116(5):051103, 2016.

[107] Alex Geringer-Sameth, Savvas M. Koushiappas, and Matthew G. Walker. Comprehensive search for dark matter annihilation in dwarf galaxies. *Phys. Rev.*, D91(8):083535, 2015.

[108] Alex Geringer-Sameth, Matthew G. Walker, Savvas M. Koushiappas, Sergey E. Koposov, Vasily Belokurov, Gabriel Torrealba, and N. Wyn Evans. Indication of Gamma-ray Emission from the Newly Discovered Dwarf Galaxy Reticulum II. *Phys. Rev. Lett.*, 115(8):081101, 2015.

[109] P. L. Nolan, A. A. Abdo, M. Ackermann, M. Ajello, A. Allafort, E. Antolini, W. B. Atwood, M. Axelsson, L. Baldini, J. Ballet, and et al. Fermi Large Area Telescope Second Source Catalog. *Astrophys.J.Suppl.*, 199:31, 2012.

[110] Kevork N. Abazajian, Nicolas Canac, Shunsaku Horiuchi, and Manoj Kaplinghat. Astrophysical and Dark Matter Interpretations of Extended Gamma-Ray Emission from the Galactic Center. *Phys.Rev.*, D90:023526, 2014.

[111] E. L. Wright et al. The Wide-field Infrared Survey Explorer (WISE): Mission Description and Initial On-orbit Performance. *Astron. J.*, 140:1868–1881, December 2010.

[112] Julio F. Navarro, Carlos S. Frenk, and Simon D. M. White. A Universal density profile from hierarchical clustering. *Astrophys. J.*, 490:493–508, 1997.

[113] Anatoly Klypin, HongSheng Zhao, and Rachel S. Somerville. LCDM-based models for the Milky Way and M31 I: Dynamical Models. *Astrophys. J.*, 573:597–613, 2002.

[114] Marco Cirelli, Gennaro Corcella, Andi Hektor, Gert Hutsi, Mario Kadastik, et al. PPPC 4 DM ID: A Poor Particle Physicist Cookbook for Dark Matter Indirect Detection. *JCAP*, 1103:051, 2011.

[115] Lan Zhang, Hans-Walter Rix, Glenn van de Ven, Jo Bovy, Chao Liu, and Gang Zhao. The Gravitational Potential Near the Sun From SEGUE K-dwarf Kinematics. *Astrophys. J.*, 772:108, 2013.

[116] J. I. Read. The Local Dark Matter Density. *J. Phys.*, G41:063101, 2014.

[117] Jo Bovy and Scott Tremaine. On the local dark matter density. *Astrophys.J.*, 756:89, 2012.

[118] Jo Bovy and Hans-Walter Rix. A Direct Dynamical Measurement of the Milky Way's Disk Surface Density Profile, Disk Scale Length, and Dark Matter Profile at 4 kpc $\stackrel{<}{\sim}$ R $\stackrel{<}{\sim}$ 9 kpc. *Astrophys. J.*, 779:115, 2013.

[119] James S. Bullock, Tsafrir S. Kolatt, Yair Sigad, Rachel S. Somerville, Andrey V. Kravtsov, Anatoly A. Klypin, Joel R. Primack, and Avishai Dekel. Profiles of dark haloes. Evolution, scatter, and environment. *Mon. Not. Roy. Astron. Soc.*, 321:559–575, 2001.

[120] Miguel A. Snchez-Conde and Francisco Prada. The flattening of the concentrationmass relation towards low halo masses and its implications for the annihilation signal boost. *Mon. Not. Roy. Astron. Soc.*, 442(3):2271–2277, 2014.

[121] Oleg Y. Gnedin, Daniel Ceverino, Nickolay Y. Gnedin, Anatoly A. Klypin, Andrey V. Kravtsov, et al. Halo Contraction Effect in Hydrodynamic Simulations of Galaxy Formation. 2011.

[122] Georges Aad et al. Search for dark matter candidates and large extra dimensions in events with a jet and missing transverse momentum with the ATLAS detector. *JHEP*, 04:075, 2013.

[123] Manoj Kaplinghat, Tim Linden, and Hai-Bo Yu. Galactic Center Excess in γ Rays from Annihilation of Self-Interacting Dark Matter. *Phys. Rev. Lett.*, 114(21):211303, 2015.

[124] Francesca Calore, Ilias Cholis, Christopher McCabe, and Christoph Weniger. A Tale of Tails: Dark Matter Interpretations of the Fermi GeV Excess in Light of Background Model Systematics. *Phys. Rev.*, D91(6):063003, 2015.

[125] Jia Liu, Neal Weiner, and Wei Xue. Signals of a Light Dark Force in the Galactic Center. *JHEP*, 08:050, 2015.

[126] James Binney and Tilmann Piffl. The distribution function of the Galaxy's dark halo. 2015. Mon. Not. Roy. Astron. Soc.accepted.

[127] Andrew B. Newman, Tommaso Treu, Richard S. Ellis, David J. Sand, Carlo Nipoti, Johan Richard, and Eric Jullo. The Density Profiles of Massive, Relaxed Galaxy Clusters: I. The Total Density Over 3 Decades in Radius. *Astrophys. J.*, 765:24, 2013.

[128] Vincenzo Vitale and Aldo Morselli. Indirect Search for Dark Matter from the center of the Milky Way with the Fermi-Large Area Telescope. In *Fermi gamma-ray space telescope. Proceedings, 2nd Fermi Symposium, Washington, USA, November 2-5, 2009*, 2009.

[129] D. Hooper and T. R. Slatyer. Two emission mechanisms in the Fermi Bubbles: A possible signal of annihilating dark matter. *Physics of the Dark Universe*, 2:118–138, September 2013.

[130] M. Ajello et al. Fermi-LAT Observations of High-Energy γ-Ray Emission Toward the Galactic Center. *Astrophys. J.*, 819(1):44, 2016.

[131] Christopher Karwin, Simona Murgia, Tim M. P. Tait, Troy A. Porter, and Philip Tanedo. Dark Matter Interpretation of the Fermi-LAT Observation Toward the Galactic Center. *Phys. Rev.*, D95(10):103005, 2017.

[132] Julio F. Navarro, Carlos S. Frenk, and Simon D. M. White. The Structure of cold dark matter halos. *Astrophys. J.*, 462:563–575, 1996.

[133] Ming-Yang Cui, Cun Zhang, and Hong-Shi Zong. Morphology of $\gamma-$ray emission induced by $e^{\pm}$ from annihilating self-interacting dark matter. *Phys. Rev.*, D93(12):123516, 2016.

[134] Thomas Lacroix, Oscar Macias, Chris Gordon, Paolo Panci, Cline Boehm, and Joseph Silk. Spatial morphology of the secondary emission in the Galactic Center gamma-ray excess. *Phys. Rev.*, D93(10):103004, 2016.

[135] Thomas Lacroix, Celine Boehm, and Joseph Silk. Fitting the Fermi-LAT GeV excess: On the importance of including the propagation of electrons from dark matter. *Phys. Rev.*, D90(4):043508, 2014.

[136] Iftah Galon, Anna Kwa, and Philip Tanedo. Lepton-Flavor Violating Mediators. *JHEP*, 03:064, 2017.

[137] Harrison Ploeg, Chris Gordon, Roland Crocker, and Oscar Macias. Consistency Between the Luminosity Function of Resolved Millisecond Pulsars and the Galactic Center Excess. *JCAP*, 1708(08):015, 2017.

[138] M. Ajello et al. Characterizing the population of pulsars in the Galactic bulge with the *Fermi* Large Area Telescope. *Submitted to: Astrophys. J.*, 2017.

[139] N. Mirabal. Dark matter vs. Pulsars: Catching the impostor. *Mon. Not. Roy. Astron. Soc.*, 436:2461, 2013.

[140] Jovana Petrovi, Pasquale D. Serpico, and Gabrijela Zaharijas. Millisecond pulsars and the Galactic Center gamma-ray excess: the importance of luminosity function and secondary emission. *JCAP*, 1502(02):023, 2015.

[141] Qiang Yuan and Bing Zhang. Millisecond pulsar interpretation of the Galactic center gamma-ray excess. *JHEAp*, 3-4:1–8, 2014.

[142] Qiang Yuan and Kunihito Ioka. Testing the millisecond pulsar scenario of the Galactic center gamma-ray excess with very high energy gamma-rays. *Astrophys. J.*, 802(2):124, 2015.

[143] Timothy D. Brandt and Bence Kocsis. Disrupted Globular Clusters Can Explain the Galactic Center Gamma Ray Excess. *Astrophys. J.*, 812(1):15, 2015.

[144] Ryan M. O'Leary, Matthew D. Kistler, Matthew Kerr, and Jason Dexter. Young Pulsars and the Galactic Center GeV Gamma-ray Excess. 2015.

[145] Ryan M. O'Leary, Matthew D. Kistler, Matthew Kerr, and Jason Dexter. Young and Millisecond Pulsar GeV Gamma-ray Fluxes from the Galactic Center and Beyond. 2016.

[146] Eric Carlson and Stefano Profumo. Cosmic Ray Protons in the Inner Galaxy and the Galactic Center Gamma-Ray Excess. *Phys.Rev.*, D90:023015, 2014.

[147] Daniele Gaggero, Marco Taoso, Alfredo Urbano, Mauro Valli, and Piero Ullio. Towards a realistic astrophysical interpretation of the gamma-ray Galactic center excess. *JCAP*, 1512(12):056, 2015.

[148] Ilias Cholis, Carmelo Evoli, Francesca Calore, Tim Linden, Christoph Weniger, and Dan Hooper. The Galactic Center GeV Excess from a Series of Leptonic Cosmic-Ray Outbursts. *JCAP*, 1512(12):005, 2015.

[149] Eric Carlson, Tim Linden, and Stefano Profumo. Improved Cosmic-Ray Injection Models and the Galactic Center Gamma-Ray Excess. *Phys. Rev.*, D94(6):063504, 2016.

[150] Meng Su, Tracy R. Slatyer, and Douglas P. Finkbeiner. Giant Gamma-ray Bubbles from Fermi-LAT: AGN Activity or Bipolar Galactic Wind? *Astrophys. J.*, 724:1044–1082, 2010.

[151] M. Ackermann et al. The Spectrum and Morphology of the *Fermi* Bubbles. *Astrophys. J.*, 793(1):64, 2014.

[152] Jovana Petrovi, Pasquale Dario Serpico, and Gabrijela Zaharija. Galactic Center gamma-ray "excess" from an active past of the Galactic Centre? *JCAP*, 1410(10):052, 2014.

[153] Mariangela Lisanti, Siddharth Mishra-Sharma, Nicholas L. Rodd, and Benjamin R. Safdi. A Search for Dark Matter Annihilation in Galaxy Groups. 2017.

[154] Mariangela Lisanti, Siddharth Mishra-Sharma, Nicholas L. Rodd, Benjamin R. Safdi, and Risa H. Wechsler. Mapping Extragalactic Dark Matter Annihilation with Galaxy Surveys: A Systematic Study of Stacked Group Searches. 2017.

[155] A. Albert et al. Searching for Dark Matter Annihilation in Recently Discovered Milky Way Satellites with Fermi-LAT. *Astrophys. J.*, 834(2):110, 2017.

[156] Dan Hooper and Tim Linden. On The Gamma-Ray Emission From Reticulum II and Other Dwarf Galaxies. *JCAP*, 1509(09):016, 2015.

[157] A. Drlica-Wagner et al. Search for Gamma-Ray Emission from DES Dwarf Spheroidal Galaxy Candidates with Fermi-LAT Data. *Astrophys. J.*, 809(1):L4, 2015.

[158] Emma Storm, Christoph Weniger, and Francesca Calore. SkyFACT: High-dimensional modeling of gamma-ray emission with adaptive templates and penalized likelihoods. *JCAP*, 1708(08):022, 2017.

[159] Richard Bartels, Emma Storm, Christoph Weniger, and Francesca Calore. The Fermi-LAT GeV Excess Traces Stellar Mass in the Galactic Bulge. 2017.

[160] Oscar Macias, Chris Gordon, Roland M. Crocker, Brendan Coleman, Dylan Paterson, Shunsaku Horiuchi, and Martin Pohl. Discovery of Gamma-Ray Emission from the X-shaped Bulge of the Milky Way. 2016.

[161] Samuel K. Lee, Mariangela Lisanti, and Benjamin R. Safdi. Distinguishing Dark Matter from Unresolved Point Sources in the Inner Galaxy with Photon Statistics. *JCAP*, 1505(05):056, 2015.

[162] Tim Linden, Nicholas L. Rodd, Benjamin R. Safdi, and Tracy R. Slatyer. High-energy tail of the Galactic Center gamma-ray excess. *Phys. Rev.*, D94(10):103013, 2016.

[163] Siddharth Mishra-Sharma, Nicholas L. Rodd, and Benjamin R. Safdi. NPTFit: A code package for Non-Poissonian Template Fitting. *Astron. J.*, 153(6):253, 2017.

[164] Shunsaku Horiuchi, Manoj Kaplinghat, and Anna Kwa. Investigating the Uniformity of the Excess Gamma rays towards the Galactic Center Region. *JCAP*, 1611(11):053, 2016.

[165] F. Acero et al. Fermi Large Area Telescope Third Source Catalog. *Astrophys. J. Suppl.*, 218(2):23, 2015.

[166] K. M. Gorski, Eric Hivon, A. J. Banday, B. D. Wandelt, F. K. Hansen, M. Reinecke, and M. Bartelman. HEALPix - A Framework for high resolution discretization, and fast analysis of data distributed on the sphere. *Astrophys. J.*, 622:759–771, 2005.

[167] J. D. Simon et al. Stellar Kinematics and Metallicities in the Ultra-Faint Dwarf Galaxy Reticulum II. *Astrophys. J.*, 808(1):95, 2015.

[168] Alex Geringer-Sameth, Savvas M. Koushiappas, and Matthew Walker. Dwarf galaxy annihilation and decay emission profiles for dark matter experiments. *Astrophys. J.*, 801(2):74, 2015.

[169] Kevork N. Abazajian and Ryan E. Keeley. Bright gamma-ray Galactic Center excess and dark dwarfs: Strong tension for dark matter annihilation despite Milky Way halo profile and diffuse emission uncertainties. *Phys. Rev.*, D93(8):083514, 2016.

[170] F. Iocco and M. Benito. An estimate of the DM profile in the Galactic bulge region. *Physics of the Dark Universe*, 15:90–95, March 2017.

[171] Maria Benito, Nicolas Bernal, Nassim Bozorgnia, Francesca Calore, and Fabio Iocco. Particle Dark Matter Constraints: the Effect of Galactic Uncertainties. *JCAP*, 1702(02):007, 2017.

[172] Niki Klop, Fabio Zandanel, Kohei Hayashi, and Shin'ichiro Ando. Impact of axisymmetric mass models for dwarf spheroidal galaxies on indirect dark matter searches. *Phys. Rev.*, D95(12):123012, 2017.

[173] Kohei Hayashi, Koji Ichikawa, Shigeki Matsumoto, Masahiro Ibe, Miho N. Ishigaki, and Hajime Sugai. Dark matter annihilation and decay from non-spherical dark halos in galactic dwarf satellites. *Mon. Not. Roy. Astron. Soc.*, 461(3):2914–2928, 2016.

[174] V. Bonnivard, C. Combet, D. Maurin, and M. G. Walker. Spherical Jeans analysis for dark matter indirect detection in dwarf spheroidal galaxies - Impact of physical parameters and triaxiality. *Mon. Not. Roy. Astron. Soc.*, 446:3002–3021, 2015.

[175] Z. Ivezić, A. J. Connolly, J. T. VanderPlass, and A. Gray. *Statistics, Data Mining, and Machine Learning in Astronomy: A Practical Python Guide for the Analysis of Survey Data (Princeton Series in Modern Observational Astronomy)*. Princeton University Press, 2014.

[176] Miguel Pato, Fabio Iocco, and Gianfranco Bertone. Dynamical constraints on the dark matter distribution in the Milky Way. *JCAP*, 1512(12):001, 2015.

[177] Alan W. McConnachie. The observed properties of dwarf galaxies in and around the Local Group. *Astron. J.*, 144:4, 2012.

[178] Manoj Kaplinghat, Sean Tulin, and Hai-Bo Yu. Dark Matter Halos as Particle Colliders: Unified Solution to Small-Scale Structure Puzzles from Dwarfs to Clusters. *Phys. Rev. Lett.*, 116(4):041302, 2016.

[179] Joshua D. Simon, Alberto D. Bolatto, Adam Leroy, Leo Blitz, and Elinor L. Gates. High-resolution measurements of the halos of four dark matter-dominated galaxies: Deviations from a universal density profile. *Astrophys.J.*, 621:757–776, 2005.

[180] Rachel Kuzio de Naray, Stacy S. McGaugh, and W.J.G. de Blok. Mass Models for Low Surface Brightness Galaxies with High Resolution Optical Velocity Fields. *Astrophys.J.*, 676:920–943, 2008.

[181] Se-Heon Oh, W.J.G. de Blok, Elias Brinks, Fabian Walter, and Jr Kennicutt, Robert C. Dark and luminous matter in THINGS dwarf galaxies. 2010.

[182] Matthew G. Walker and Jorge Penarrubia. A Method for Measuring (Slopes of) the Mass Profiles of Dwarf Spheroidal Galaxies. *Astrophys.J.*, 742:20, 2011.

[183] Andrew B. Newman, Tommaso Treu, Richard S. Ellis, and David J. Sand. The Density Profiles of Massive, Relaxed Galaxy Clusters: II. Separating Luminous and Dark Matter in Cluster Cores. *Astrophys.J.*, 765(issue):25, 2013.

[184] F. Governato, A. Zolotov, A. Pontzen, C. Christensen, S.H. Oh, et al. Cuspy No More: How Outflows Affect the Central Dark Matter and Baryon Distribution in Lambda CDM Galaxies. *Mon.Not.Roy.Astron.Soc.*, 422:1231–1240, 2012.

[185] Alyson M. Brooks and Adi Zolotov. Why Baryons Matter: The Kinematics of Dwarf Spheroidal Satellites. 2012.

[186] Kenza S. Arraki, Anatoly Klypin, Surhud More, and Sebastian Trujillo-Gomez. Effects of baryon removal on the structure of dwarf spheroidal galaxies. 2012.

[187] Matthias Gritschneder and Douglas N.C. Lin. Explaining the observed velocity dispersion of dwarf galaxies by baryonic mass loss during the first collapse. *Astrophys.J.*, 765:38, 2013.

[188] Milos Milosavljevic and Volker Bromm. Dwarf Spheroidal Satellite Formation in a Reionized Local Group. 2013.

[189] Nicola Cristiano Amorisco, Jesus Zavala, and Thomas J. L. de Boer. Dark matter cores in the Fornax and Sculptor dwarf galaxies: joining halo assembly and detailed star formation histories. *Astrophys.J.*, 782:L39, 2014.

[190] David N. Spergel and Paul J. Steinhardt. Observational evidence for selfinteracting cold dark matter. *Phys.Rev.Lett.*, 84:3760–3763, 2000.

[191] Annika H.G. Peter, Miguel Rocha, James S. Bullock, and Manoj Kaplinghat. Cosmological Simulations with Self-Interacting Dark Matter II: Halo Shapes vs. Observations. 2012.

[192] Mark Vogelsberger, Jesus Zavala, and Abraham Loeb. Subhaloes in Self-Interacting Galactic Dark Matter Haloes. *Mon.Not.Roy.Astron.Soc.*, 423:3740, 2012.

[193] Jesus Zavala, Mark Vogelsberger, and Matthew G. Walker. Constraining Self-Interacting Dark Matter with the Milky Way's dwarf spheroidals. 2012.

[194] Sean Tulin, Hai-Bo Yu, and Kathryn M. Zurek. Beyond Collisionless Dark Matter: Particle Physics Dynamics for Dark Matter Halo Structure. 2013.

[195] Manoj Kaplinghat, Sean Tulin, and Hai-Bo Yu. Direct Detection Portals for Self-interacting Dark Matter. 2013.

[196] J. Binney and S. Tremaine. In *Galactic Dynamics.* Princeton University Press, Princeton, 1987.

[197] Paul J. McMillan. Mass models of the Milky Way. *Mon.Not.Roy.Astron.Soc.*, 414:2446–2457, 2011.

[198] Francisco Prada, Anatoly A. Klypin, Antonio J. Cuesta, Juan E. Betancort-Rijo, and Joel Primack. Halo concentrations in the standard LCDM cosmology. 2011.

[199] Oleg Y. Gnedin, Andrey V. Kravtsov, Anatoly A. Klypin, and Daisuke Nagai. Response of dark matter halos to condensation of baryons: Cosmological simulations and improved adiabatic contraction model. *Astrophys.J.*, 616:16–26, 2004.

[200] N. C. Amorisco and G. Bertin. Self-consistent nonspherical isothermal halos embedding zero-thickness disks. *Astronomy & Astrophysics*, 519:A47, September 2010.

[201] Scott W. Randall, Maxim Markevitch, Douglas Clowe, Anthony H. Gonzalez, and Marusa Bradac. Constraints on the Self-Interaction Cross-Section of Dark Matter from Numerical Simulations of the Merging Galaxy Cluster 1E 0657-56. *Astrophys.J.*, 679:1173–1180, 2008.

[202] P. Salucci, M. I. Wilkinson, M. G. Walker, G. F. Gilmore, E. K. Grebel, A. Koch, C. Frigerio Martins, and R. F. G. Wyse. Dwarf spheroidal galaxy kinematics and spiral galaxy scaling laws. *MNRAS*, 420:2034–2041, March 2012.